UNIVERSITAT POLITÈCNICA DE CATALUNYA BARCELONATECH

Partial oxidation of methane into syngas at low temperature

Shiva Fazlikeshteli

UNIVERSITAT POLITÈCNICA
DE CATALUNYA
BARCELONATECH

Partial oxidation of methane into syngas at low temperature

PhD thesis
Shiva Fazlikeshteli
2023

PhD program in Chemical Process Engineering

Partial oxidation of methane into syngas at low temperature

Doctoral thesis by:

Shiva Fazlikeshteli

Thesis advisors:

Prof. Jordi Llorca Piqué

Dr. Xavier Vendrell Villafruela

Department of Chemical Engineering

Universitat Politècnica de Catalunya (UPC)

Barcelona - May 2023

Acknowledgments

I would like to express my sincere gratitude to my thesis supervisor Prof. Jordi Llorca and my co-supervisor Dr. Xavier Vendrell for their invaluable guidance, support, and encouragement throughout this research project. Their expertise and insights have been instrumental in shaping my academic journey and achieving the goals of this thesis. I would also like to extend my heartfelt thanks to our research group (NEMEN) at Universitat Politècnica de Catalunya (UPC), for providing a stimulating research environment and valuable feedback during the course of this project.

I would like to express my sincere gratitude to Agència de Gestió d´Ajuts Universitaris i de Recerca (2019FI-B00908), and Universitat Politècnica de Catalunya (UPC), for their unwavering support and encouragement throughout my Ph.D. project. Their funding and resources have been instrumental in enabling me to conduct my research and pursue my academic goals.

Contents

List of Symbols

ATR	Autothermal reforming
BE	Binding energy
BM	Ball mill
BPR	Ball to powder ratio
DPO	Direct partial oxidation of methane to methanol
DPOM	Direct partial oxidation of methane
DRM	Dry reforming of methane
EDX	Energy dispersive X–ray spectroscopy
Eq	Equation
Fig	Figure
FTs	Fischer–Tropsch synthesis
GC	Gas chromatography
GHGs	Greenhouse gases
GHSV	Gas hourly space velocity
Hz	Hertz
HRTEM	High-resolution transmission electron microscopy
ICP	Intergovernmental Panel on Climate Change
IUPAC	International Union of Pure and Applied Chemistry
IWI	Incipient wetness impregnation
LNG	Liquefied natural gas

MC	Mechanochemistry
NG	Natural gas
nm	Nanometer
OCM	Oxidative coupling of methane
P	Pressure
PID	Proportional–integral–derivative
POM	Partial oxidation of methane
S/C	Steam/Carbon
SRM	Steam reforming of methane
Syngas	Synthesis gas
T	Temperature
TCD	Thermal Conductivity Detector
TPR	Temperature programmed reduction
WGS	Water gas shift
WHO	World Health Organization
XPS	X–ray Photoelectron Spectroscopy

Abstract

Syngas (a mixture of H_2 and CO) is a versatile feedstock that can be used to produce a wide range of chemicals and fuels. For that reason, there is a great interest to optimize and explore new routes for its production. The most common methods for syngas production are the steam reforming of methane (SRM), the partial oxidation of methane (POM), and the dry reforming of methane (DRM). In this thesis, a series of monometallic Pd, Ru, Ni, and bimetallic Pd–Ni, Ru–Ni, and Ru–Pd catalysts loaded on CeO_2 support have been prepared via dry ball milling (BM) and conventional incipient wetness impregnation (IWI) methods. The results showed that the dry ball mill technique can be used to prepare highly dispersed metal species strongly interacting with the ceria support. The use of this technique led to an improvement in the POM catalytic activity, particularly at low temperature, compared to the conventional IWI method. This project contributes to an increased knowledge concerning the influence of the order of addition of the metals, metal ratio, milling energy, and time for samples prepared by the mechanochemical method on

methane conversion and syngas yield. In order to determine the durability and performance of the catalysts, long-term stability tests were carried out for more than 100 h. Raman spectroscopy, temperature programmed reduction (H_2-TPR), X–ray photoelectron spectroscopy (XPS), X–ray diffraction (XRD), and high-resolution transmission electron microscopy (HRTEM) have been used to characterize the catalysts before and after reaction.

Resumen

El gas de síntesis (compuesto por H_2 y CO) es una materia prima versátil que se puede utilizar para producir una amplia gama de productos químicos y combustibles. Por esta razón, existe un gran interés en optimizar y explorar nuevas rutas para su producción. Los métodos más comunes para la producción de gas de síntesis son el reformado con vapor de metano (*SRM*, de sus siglas en inglés), la oxidación parcial de metano (*POM*) y el reformado seco de metano (*DRM*). En esta tesis se prepararon una serie de catalizadores monometálicos de Pd, Ru, Ni y bimetálicos de Pd–Ni, Ru–Ni y Ru–Pd sobre un soporte de CeO_2 utilizando métodos mecanoquímicos (*BM*) e impregnación a humedad incipiente (*IWI*). Los resultados mostraron que la técnica de molienda en seco puede utilizarse para preparar especies metálicas altamente dispersas que interactúan fuertemente con el soporte de ceria. El uso de esta técnica resultó en una mejora en la actividad catalítica de *POM*, especialmente a baja temperatura, en comparación con el método convencional *IWI*. Este proyecto contribuye a aumentar el conocimiento sobre la influencia del orden de adición de los

metales, la relación entre metales, la energía de molienda y el tiempo de molienda para las muestras preparadas por el método mecanoquímico en la conversión de metano y el rendimiento a gas de síntesis. Para determinar la durabilidad de los catalizadores, se llevaron a cabo pruebas de estabilidad a largo plazo durante más de 100 horas. Se utilizaron la espectroscopia Raman, reducción térmica programada (H_2-TPR), espectroscopia fotoelectrónica de rayos X (XPS), difracción de rayos X (XRD) y microscopía electrónica de transmisión de alta resolución (HRTEM) para caracterizar los catalizadores, antes y después de la reacción.

Resum

El gas de síntesi (una barreja d'H_2 i CO) és una matèria primera versàtil que es pot utilitzar per produir una àmplia gamma de productes químics i combustibles. Per aquesta raó, hi ha un gran interès per optimitzar i explorar noves vies per a la seva producció. Els mètodes més comuns per a la producció de gas de síntesi són la reformació amb vapor de metà (SRM), l'oxidació parcial del metà (POM) i la reformació seca del metà (DRM). En aquesta tesi, s'han preparat una sèrie de catalitzadors monometàl·lics de Pd, Ru i Ni i bimetàl·lics de Pd-Ni, Ru-Ni i Ru-Pd sobre un suport de CeO_2 mitjançant mètodes de mòlta en sec (BM) i impregnació a humitat incipient convencional (IWI). Els resultats van mostrar que la tècnica de mòlta en sec pot ser utilitzada per preparar espècies metàl·liques altament disperses que interactuen fortament amb el suport de cèria. L'ús d'aquesta tècnica va portar a una millora en l'activitat catalítica de POM, especialment a baixa temperatura, en comparació amb el mètode IWI convencional. Aquest projecte contribueix a del augmentar el coneixement sobre la influència de l'ordre d'addició dels metalls, la

relació metàl·lica, l'energia de mòlta i el temps de molta per a mostres preparades pel mètode mecanoquímic en la conversió de metà i el rendiment a gas de síntesi. Per determinar la durabilitat dels catalitzadors, es van dur a terme proves de resistència durant més de 100 hores. S'ha utilitzat l'espectroscòpia Raman, la reducció tèrmica programada (H_2-TPR), l'espectroscòpia fotoelectrònica de raigs X (XPS), la difracció de raigs X (XRD) i la microscòpia electrònica de transmissió d'alta resolució (HRTEM) per caracteritzar els catalitzadors abans i després de la reacció.

1. Introduction

1.1 Setting the scene

Since the 1960s, many different human activities have required the extensive use of energy, which it is fulfilled mainly by the burning of fossil fuels to produce electricity, power factories, heat houses, power automobiles, etc. As it is well known, burning fossil fuels causes the emission of a massive amount of greenhouse gases (GHGs) [2, 3]. Fig–1.1 shows the composition of GHGs produced by consumers worldwide since 1978.

All of these gases such as carbon dioxide (CO_2), methane (CH_4), nitrous oxide (N_2O), and chlorofluorocarbons (CFCs) represent GHGs emissions and can remain in the atmosphere for different amounts of time, ranging from a few years to thousands of years [4]. From Fig–1.2, it can be found that CO_2 and CH_4 are the main components of GHGs emission, accounting for 76.0 and 16 %, respectively.

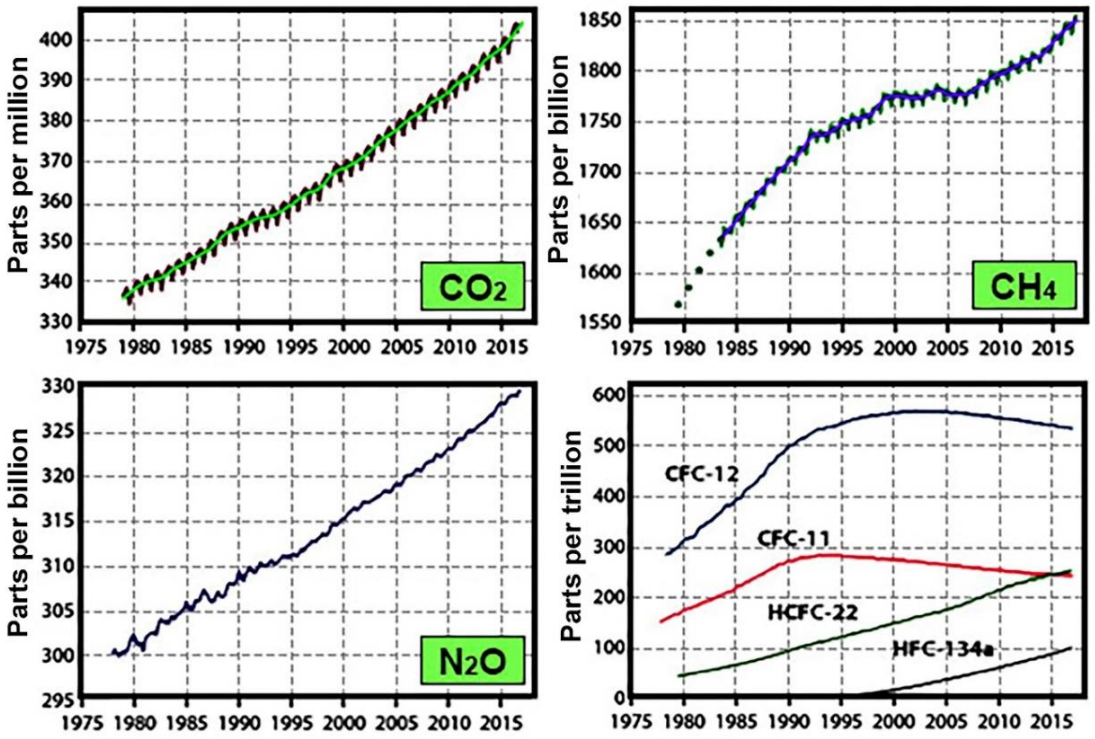

Fig-1. 1: Global averages of the concentrations of the greenhouse gases carbon dioxide, methane, nitrous oxide, CFCs-12, CFCs-11, HCFCs-22, HFCs-134a. Adapted from [5].

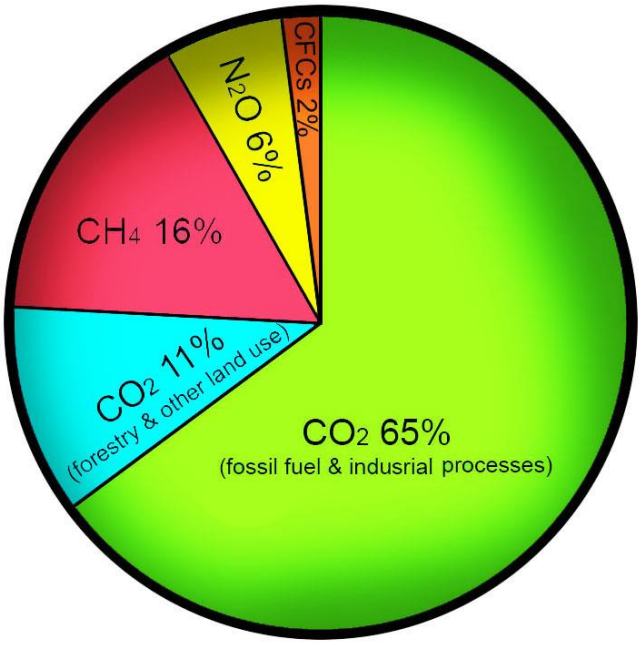

Fig-1. 2: Global GHGs emissions. Redrawn from [6].

GHGs have resulted in additional heat being trapped in the lower atmosphere, ozone depletion, and potentially contributing to the rise in temperature and global warming bringing a lot of negative impacts on the environment and, most importantly, the activity and survival of human life [7, 8]. According to a World Health Organization (WHO) report, the Earth's temperature has risen approximately 1.1 °C in the last one hundred years, which means every quarter century is experiencing an increase in temperature of about 0.27 °C, and this high rate of global warming is affecting the world's ecosystems [9, 10]. Additionally, according to the Fifth Assessment Report (AR5) of the Intergovernmental Panel on Climate Change (IPC) in 2014, the average temperature in 2100 will become 4.8 °C higher than now in the worst-case scenario [10].

From another angle, the human population in 1750 was approximately 800 million, in 1900, it increased to 1.6 billion, and in 2022, and the global population has achieved more than 7.9 billion. The increase of worldwide population is obviously accompanied by an increase of the worldwide energy demand [9, 11, 12]. As an example, a survey from the US Department of Energy in 2009 revealed that the consumption of electricity increases significantly every year and is projected to increase by 44% from 2006 to 2030 [8].

Thus, an increasingly concern about the growing of GHGs emissions has pushed the society to lean more onto a sustainable development technology of more efficient and less polluting energy sources [13]. There is large consensus among researchers that renewable energy sources are the only way forward to guarantee the consistent welfare of human society [14]. Reducing GHGs emissions is an urgent challenge for all countries to solve environmental problems, and collecting or converting the existing GHGs has also been an effective approach to settle these issues.

1.2 Natural gas

Natural gas (NG) is a hydrocarbon mixture of light gases of natural origin and is typically used as fuel for power generation, transportation, and domestic heating. Methane (CH_4) is a colorless, odorless gas and the simplest hydrocarbon molecule, and it is the main component of natural gas (>90%), landfill gas, and a by-product from oil refining and chemical processing which is forecast to outlast oil by a significant margin (around 60 years) [15, 16].

CH_4's lifetime in the atmosphere is much shorter than CO_2, but on a 20-year timescale, a CH_4 molecule is roughly 90 times more effective at trapping heat in the atmosphere than a molecule of CO_2, the GHGs that wields the most control over Earth's future warming in the long-term [17].

Moreover, CH_4's atmospheric concentrations have increased by at least 150 percent since the Industrial Revolution [18]. Globally, CH_4 is emitted from energy, industry, agriculture, land use, and waste management activities (50–65% of total CH_4 emissions come from human activities) [19]. In general, CH_4 emission sources can be classified into two categories: natural sources of methane and anthropogenic sources of methane [18, 20]. Fig–1.3 presents the anthropogenic CH_4 emissions from all different source sectors while Fig–1.4 shows the contribution of individual sources to total natural CH_4 emissions [21].

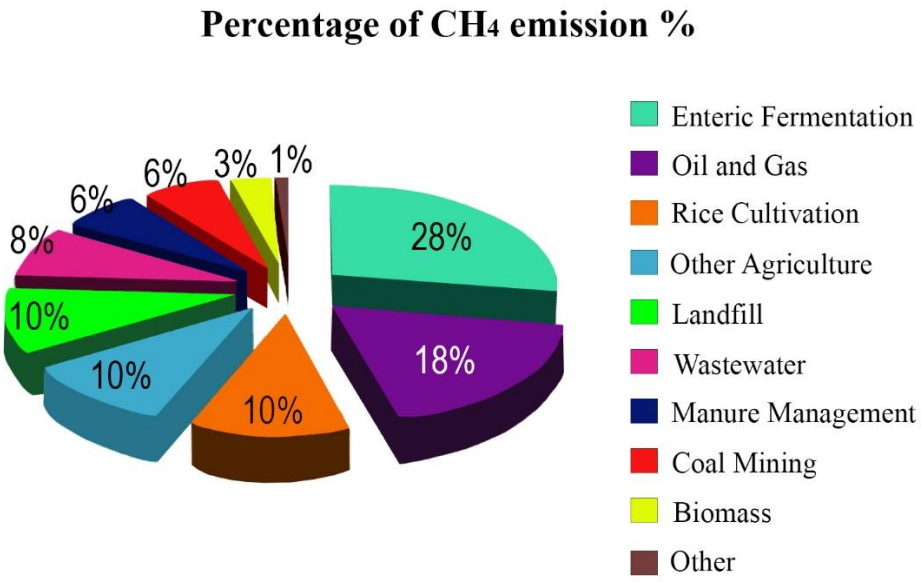

Fig-1. 3: Anthropogenic methane emissions from all different source sectors. Redrawn from [21].

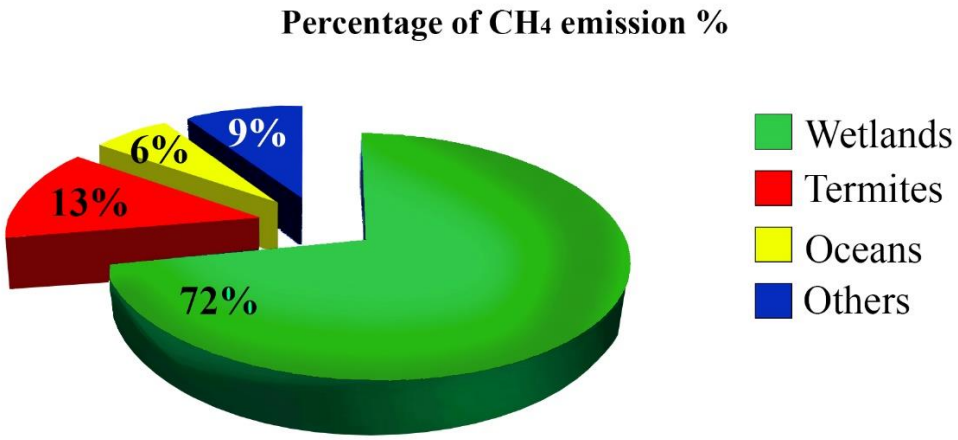

Fig-1. 4: Contribution of individual sources to total natural methane emissions. Redrawn from [21].

The Paris Agreement's goal of limiting global warming to well below two degrees above pre-industrial levels will necessitate a concerted effort to reduce CH_4 emissions in addition to the essential decarbonization and improvement of the energy systems' efficiency [22]. Although CH_4 combustion is more efficient and leaves a smaller

carbon footprint than other carbon-containing fuels, methane can be used for producing synthesis gas (syngas, a mixture of hydrogen and carbon monoxide), long-chain hydrocarbons or hydrogen, which can be used in the chemical industry as well as for fueling fuel cells. In addition to boost the added value of natural gas, the development of new processes for converting CH_4 to valuable chemicals would and enable the efficient use of medium-sized and smaller gas resources at a reduced cost [23, 24] because neither pipelines nor liquefied natural gas (LNG) transports are economically viable in the case of medium or small gas fields far from the areas where the gas will be used.

1.3 Possible pathways for methane conversion

Fig–1.5 gives a summary of the two main routes of CH_4 conversion to useful products. They can be classified into: [25].

1. Direct conversion of methane,
2. Indirect conversion of methane.

Direct conversion includes oxidative coupling of methane to ethylene (C_2H_4) [26], and oxidation of methane to methanol (CH_3OH) or formaldehyde (CH_2O), etc. [27]. On the other side, indirect conversion means firstly converting CH_4 to syngas, and then converting syngas to methanol or to liquid hydrocarbons by the Fischer–Tropsch process, which could be used to replace petroleum products (such as gasoline) [28]. In addition, syngas could be used to synthesize fine chemicals or ammonia [29].

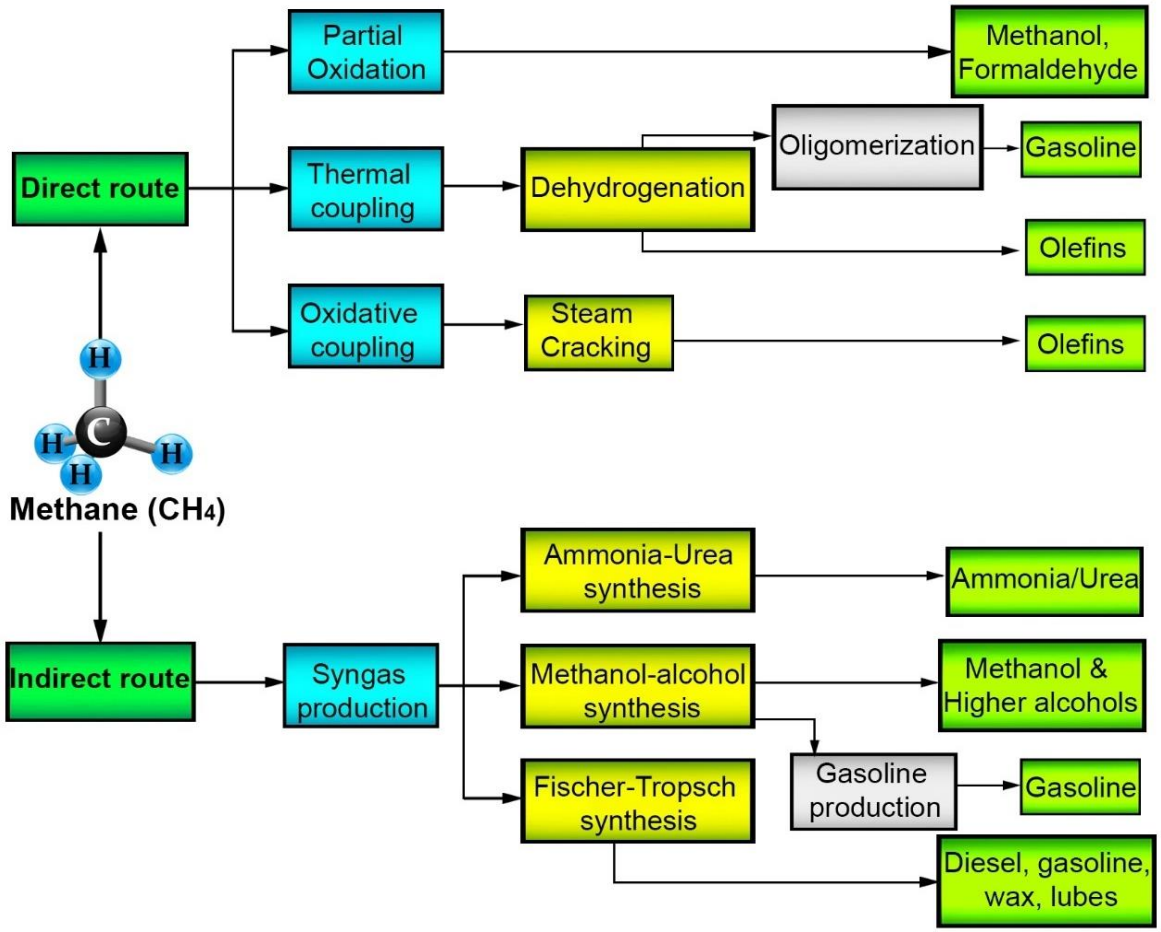

Fig-1. 5: Conceptual routes for chemical conversion of methane. Redrawn from [30].

1.3.1 Direct conversion of methane

Direct conversion of methane is a one-step process where methane is directly converted to desired products without passing through intermediates [31]. Compared with the indirect methods, direct methods are potentially simpler in technology and more economical [32]. Two major direct conversion routes are [33, 34]: Oxidative coupling of methane (OCM) to C_2 hydrocarbons and the other one is direct partial oxidation of methane to formaldehyde or methanol (DPO). Conceptually, direct methods should have a distinct economic advantage over indirect methods, but apart from complete combustion for heating purposes which results in the production of CO_2, and water, all other direct conversion routes have not yet been realized on an

industrial scale [35]. This is mostly because generally desired product yields when operating in a single-pass mode are not sufficiently high (less than 5%) to be of interest for commercial application [36].

1.3.1.1 Oxidative coupling of methane to C_2 hydrocarbons (OCM)

In 1982, the investigation of Keller and Bhasin [37] demonstrated that two molecules of CH_4 could be coupled oxidatively over a PbO/Al_2O_3 (Fig–1.6) catalyst at high temperatures to form ethane (C_2H_6) as a primary product and ethylene (C_2H_4) as a secondary product by the following equations:

$$2CH_4 + \frac{1}{2}O_2 \longrightarrow C_2H_6 + H_2O \qquad \Delta H°_{298K} = -88.38 \text{ kJ mol}^{-1} \qquad \text{(Eq–1.1)}$$

$$2CH_4 + O_2 \longrightarrow C_2H_4 + 2H_2O \qquad \Delta H°_{298K} = -140.72 \text{ kJ mol}^{-1} \qquad \text{(Eq–1.2)}$$

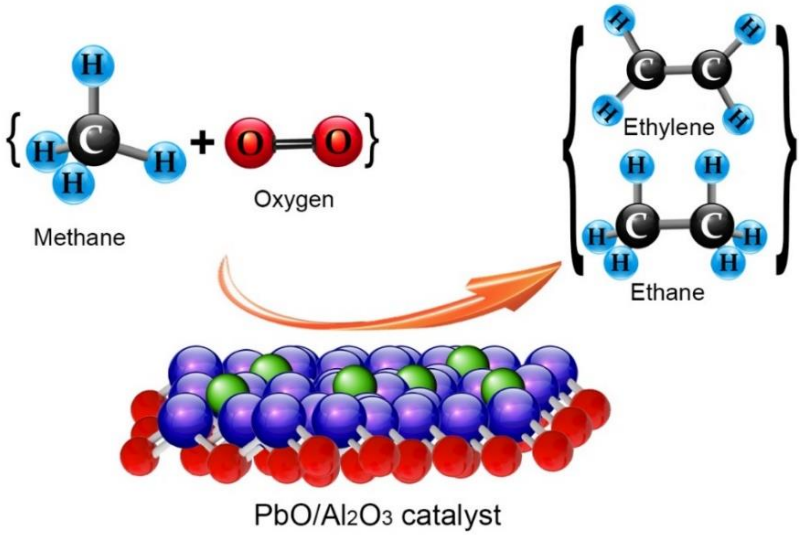

Fig-1. 6: Typical Oxidative coupling of methane to C_2 hydrocarbons production. Redrawn from [37].

Fang et al. [38] proposed a heterogeneous-homogeneous mechanism, after investigating the pyrolysis of methane over OCM catalysts including the heterogeneous formation of methyl radicals with their recombination to ethane in the

gas phase. Heterogeneous generation of methyl radicals is postulated in all the models:

$$O_{ads\cdot} + 2CH_4 \rightarrow OH_{ads} + CH_{3\cdot} \qquad \text{(Eq–1.3)}$$

In the gas phase the methyl radicals recombine with the formation of ethane, a primary C_2 hydrocarbon, and by via dehydrogenation of C_2H_6 can be further converted to ethylene (C_2H_4) and ethyne (C_2H_2):

$$2CH_{3\cdot} \rightarrow C_2H_6 \xrightarrow{-H_2} C_2H_4 \xrightarrow{-H_2} C_2H_2 \qquad \text{(Eq–1.4)}$$

However, the yield of the C_2 product obtained in a packed-bed catalytic reactor is only about 25% due to an intrinsic constraint. This is due to complete oxidation processes that partially occur on the catalyst surface and completely occur in the gas phase, which Only a selectivity significantly reduces the C_2 selectivity, especially at high temperatures and pressures. of up to 70% has thus far been attained with a CH_4 conversion rate of greater than 30%. Additionally, the cost of its separation is significant [23, 37, 39] due to the low concentration of C_2H_4 in the exit stream. OCM has not yet been commercialized, despite the amount of research that has been done on this technology [40].

1.3.1.2 Direct partial oxidation of methane to methanol (DPO)

Direct partial oxidation of methane to methanol (DPO) is another method that converts methane directly into methanol in a single step. In DPO process, in the presence of a catalyst, methane is reacted with oxygen which results in the formation of formaldehyde (CH_2O) and water [41]. The formaldehyde is then oxidized further to produce methanol and additional water. The overall methanol synthesis process is represented by the following reaction [42]:

$$CH_4 + \frac{1}{2}O_2 + H_2O \longrightarrow CH_3OH + H_2O \qquad \Delta H°_{298K} = -164.2 \text{ kJ mol}^{-1} \qquad \text{(Eq–1.5)}$$

Even though the DPO process has a high selectivity (about 80%) under ideal circumstances, the yield of methanol per pass is still less than 7% because of the extremely poor methane conversion for a single pass [31]. Because of this, a very high recycle ratio is needed, which makes it difficult to separate the final product due to the low partial pressure of CH_3OH.

1.3.2 Indirect conversion of methane

The indirect route is a two-step process in which methane is first transformed into an intermediate, most frequently syngas, and then in the following stage, syngas is transformed into the desired product(s) by a downstream catalytic conversion [43].

1.3.2.1 Industrial methanol (CH_3OH) synthesis

Syngas is generally utilized to produce methanol, which serves as the precursor to the manufacturing of many other chemical industrial products. CH_3OH is produced via a two-step process where syngas is produced first, followed by the synthesis of CH_3OH from the syngas:

$$CH_4 + H_2O \longrightarrow CO + 3H_2 \qquad \Delta H°_{298K} = 206 \text{ kJ mol}^{-1} \qquad \text{(Eq–1.6)}$$

$$CH_4 + CO_2 \longrightarrow 2CO + 2H_2 \qquad \Delta H°_{298K} = 247 \text{ kJ mol}^{-1} \qquad \text{(Eq–1.7)}$$

$$CH_4 + \frac{1}{2}O_2 \longrightarrow CO + 2H_2 \qquad \Delta H°_{298K} = -127 \text{ kJ mol}^{-1} \qquad \text{(Eq–1.8)}$$

$$CO + 3H_2 \longrightarrow CH_3OH + H_2O \qquad \Delta H°_{298K} = -49.5 \text{ kJ mol}^{-1} \qquad \text{(Eq–1.9)}$$

$$CO + 2H_2 \longrightarrow CH_3OH \qquad \Delta H°_{298K} = -90.6 \text{ kJ mol}^{-1} \qquad \text{(Eq–1.10)}$$

The water gas shift equilibrium (WGS) in present as well:

$CO + H_2O \rightleftarrows CO_2 + H_2$ $\Delta H°_{298K}$= -41.2 kJ mol^{-1} (Eq–1.11)

Equations–1.6-8 represent different routes to produce of syngas from methane, namely methane steam reforming (Eq–1.6), methane dry reforming (Eq–1.7) and methane partial oxidation (Eq–1.8).

1.3.2.2 Fischer–Tropsch synthesis (FTs)

The Fischer–Tropsch synthesis (FTS) is another important development for the conversion of syngas into a wide range of hydrocarbon products [44]:

$nCO + 2nH_2 \longrightarrow (-CH_2-)_n + nH_2O$ $\Delta H°_{298K}$= -165 kJ mol^{-1} (Eq. 1.12)

FTs process was established in 1923 by Franz Fischer and Hans Tropsch, and has since been used for the production of synthetic fuels and chemicals [44]. They discovered that syngas over a metal catalyst such as Ru, Co, Fe or similar metals, could be converted to paraffinic liquid, olefins, and oxygenates, at elevated temperatures and pressures (the operating temperature and pressure of the FTs processes are in the range of 150–350 °C, and of 18–45 bar, respectively). This product mixture is often called synthetic crude oil or "syncrude" which can be used for the production of high quality diesel fuel, gasoline and linear chemicals such as alkanes, and alkenes [45].

1.3.3 Syngas production

According to estimates, the generation of syngas accounts for more than 60% of the cost of the whole process in the majority of natural gas applications, including those for methanol, FTs synthesis, and ammonia [46]. On the other hand, syngas reaction produces more than 75% of the methanol [2]. The entire economics of these downstream operations would be significantly and directly impacted by a reduction

in syngas production costs. Therefore, both industry and academia have given a lot of attention to syngas production research.

Nowadays, the most common industrial technologies to produce syngas from methane are: the steam reforming of methane (SRM) [47], dry reforming of methane (DRM) with CO_2 [48, 49], partial oxidation of methane (POM) with O_2 [50, 51], and autothermal reforming (ATR). Fig–1.7 illustrates the main types of reactors currently used. In order to obtain a sufficiently high per pass conversion of methane, the temperature at the exit of the reactor(s) should be high (around 1000 °C), at these conditions exit compositions are very close to the equilibrium value [52].

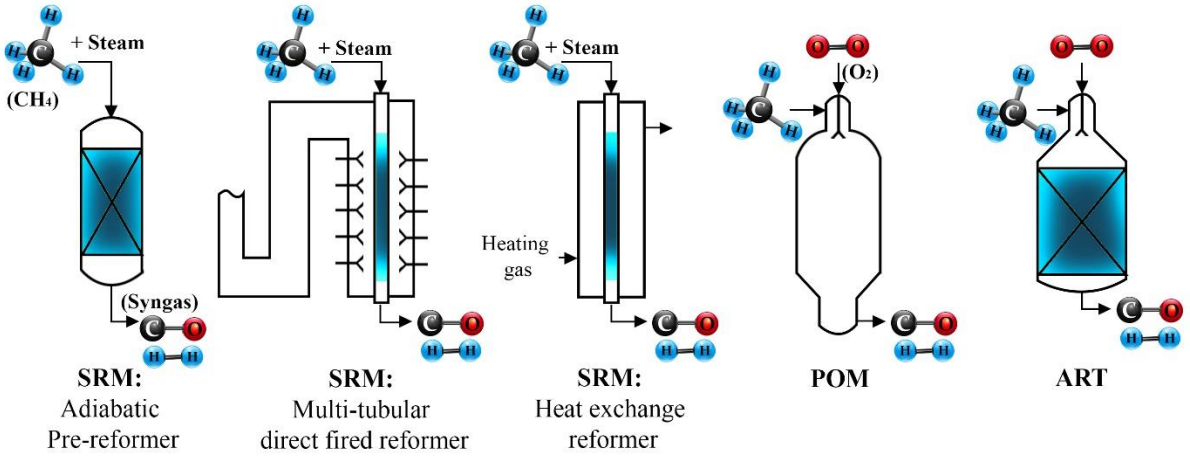

Fig-1. 7: Different types of reactors for syngas production. Redrawn from [53, 54].

1.3.3.1 Steam reforming of methane (SRM)

Steam reforming of methane (SRM), which was initially developed in 1926, is currently the most commonly used method for producing syngas from NG [55]. Fig–1.8 shows the typical SRM process. The process to produce synthesis gas from steam and methane is reached by the following reactions:

$$CH_4 + H_2O \longrightarrow CO + 3H_2 \qquad \Delta H°_{298K} = 206 \text{ kJ mol}^{-1} \qquad \text{(Eq–1.6)}$$

WGS:

$CO + H_2O \rightleftarrows CO_2 + H_2$ $\Delta H°_{298K}$= -41.2 kJ mol^{-1} (Eq–1.11)

And methane cracking/decomposition as well:

$CH_4 \longrightarrow C + 2H_2$ $\Delta H°_{298K}$= 76 kJ mol^{-1} (Eq–1.13)

In general, the three parameters temperature, pressure, and steam/carbon (S/C) ratio must be chosen in a way that maximizes syngas production while avoiding coke formation in an acceptable temperature field [56]. Overall, SRM process has a strong endothermic response, large capital expenditure requirements, and a catalyst-coking tendency (often, nickel supported on alumina catalysts are utilized). Large volumes of fibrous carbon can accumulate at high reaction temperatures, which can affect the catalyst's activity and stability and potentially cause reactor damage [56]. To prevent carbon deposition, a high H_2O:CH_4 ratio is required (from 2 to 6). Moreover, excess of water accelerates WGS reaction (Eq–1.11), resulting in a high H_2:CO ratio (≥3), compared to that required for downstream processes, e.g. FTs or methanol synthesis H_2:CO (≥ 2) [57, 58].

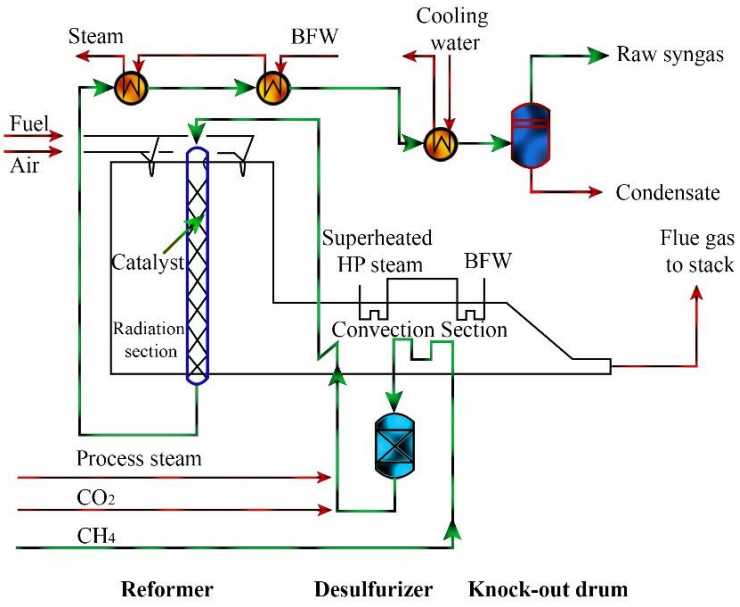

Fig-1. 8: Typical steam reforming process for syngas production [55]

Joensen and Rostrup-Nielsen [59] published a typical equilibrium conversion graph of SRM against T, P, and S/C ratio (Fig–1.9), and they suggested that because the reaction progresses with an increase in the total number of molecules, it is necessary to operate the system at high temperatures, low pressures, and relatively high S/C ratios in order to achieve higher methane conversion and syngas yields. The hydrocarbons may experience thermal cracking at temperatures as high as 650 °C, which results in the creation of coke. As in the earlier description, such excess of superheated steam at high temperature is expensive and it requires an "extra fuel", in addition to the SRM reactions stoichiometric requirements to be fired outside of the reformer tubes to supply the necessary heat to sustain the endothermic reforming reactions [60]. Industrially, the SRM process is usually conducted at high temperature and pressure (typically 800–1000 °C and 30–40 bar), followed by an additional two-step shift section at lower temperature (typically 200–400 °C), in order to maximize the CO conversion [61]. The reaction heat is provided by a furnace system including tubular reactors filled with Ni based catalysts.

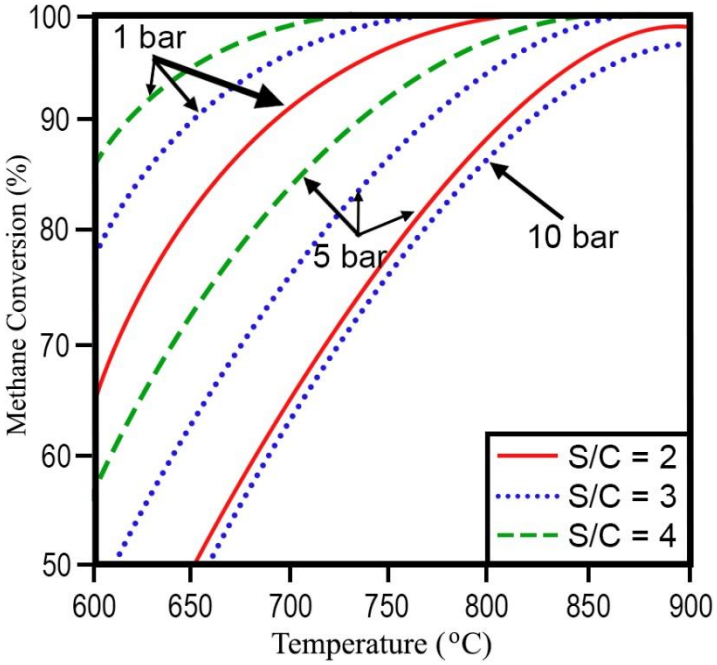

Fig-1. 9: Equilibrium conversion of SRM against T,P, and S/C ratio. Adapted from [59].

1.3.3.2 Dry reforming of methane (DRM)

Dry reforming of methane (DRM) with carbon dioxide has been identified as a process which has the potentials to mitigate the environmental challenges associated with GHGs emissions and to convert biogas directly to syngas (with a H_2/CO molar ratio of 1) according the following reaction [60, 62]:

$$CH_4 + CO_2 \longrightarrow 2CO + 2H_2 \qquad \Delta H°_{298K} = 247 \text{ kJ mol}^{-1} \qquad \text{(Eq–1.7)}$$

Side reactions include CO disproportionation or Boudouard reaction (Eq–1.14) and methane decomposition (Eq–1.15):

$$2CO \longrightarrow C + CO_2 \qquad \Delta H°_{298K} = -172 \text{ kJ mol}^{-1} \qquad \text{(Eq–1.14)}$$

$$CH_4 \longrightarrow C + 2H_2 \qquad \Delta H°_{298K} = 76 \text{ kJ mol}^{-1} \qquad \text{(Eq–1.15)}$$

Despite its considerable environmental potentials, DRM is not considered an industrially mature process. The thermodynamic studies on DRM reaction reveals, as an extremely high endothermic reaction, this process requires large heat input, and spontaneous reaction cannot be achieved below 640 °C [63]. A specific problem which has to be resolved with this process is its greater potential for carbon formation, which rapidly deactivates the catalysts [64]. Additionally, the issue of some impurities in the carbon dioxide feed, which is often overlooked, could cause serious catalyst poisoning [65]. Fig–1.10 displays the typical scheme for the SRM process.

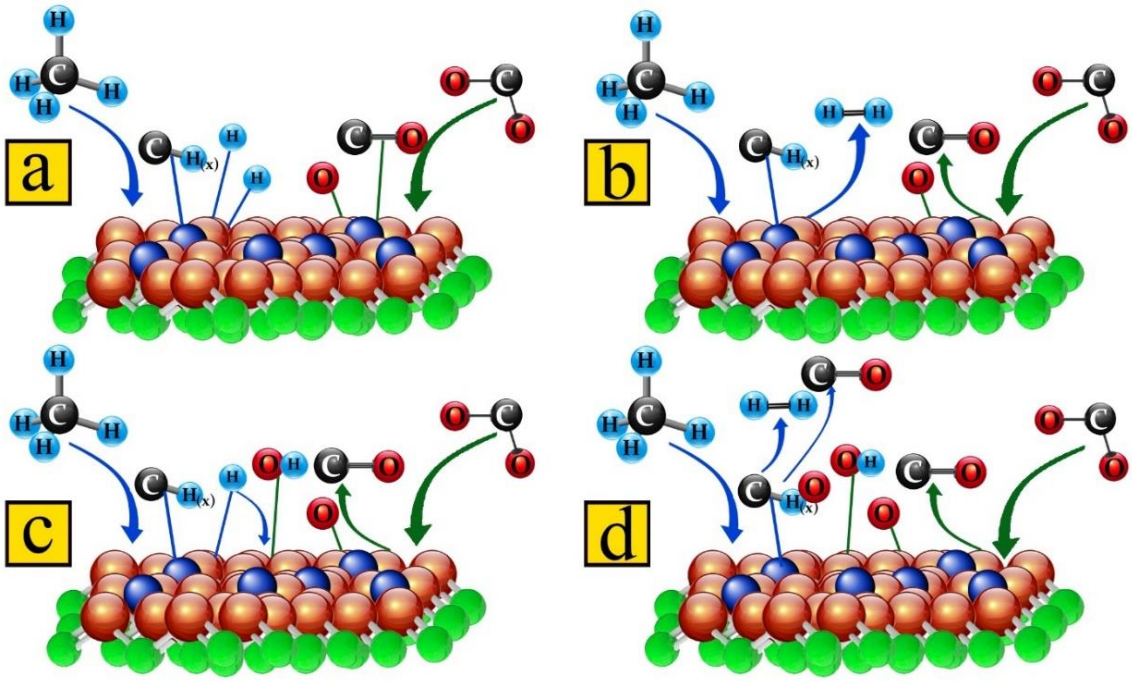

Fig-1. 10: Reaction steps for the DRM: (a) Dissociative adsorption of CO_2 on the metal and metal-support interface respectively. (b) Fast desorption of CO and hydrogen. (c) Formation of surface hydroxyls and oxygen spill-over (d) Surface hydroxyls and oxygen species oxidize hydrogen depleted S–CH_x species and formation of CO and H_2. Adapted from [65].

1.3.3.3 Partial oxidation of methane (POM)

The catalytic partial oxidation of methane (POM) to syngas began as early as 1946 [66]. In the presence of oxygen, methane partial oxidation (Eq–1.8) and methane total oxidation (Eq–1.16) take place by the following reactions:

$$CH_4 + \frac{1}{2}O_2 \longrightarrow CO + 2H_2 \qquad \Delta H°_{298K} = -36 \text{ kJ mol}^{-1} \qquad \text{(Eq–1.8)}$$

$$CH_4 + 2O_2 \longrightarrow CO_2 + 2H_2O \qquad \Delta H°_{298K} = -803 \text{ kJ mol}^{-1} \qquad \text{(Eq–1.16)}$$

Compared with SRM, the DRM and POM processes have distinct advantages, including:

- It is a mildly exothermic reaction and no external heat source is necessary to sustain the process, while the SRM and DRM processes are highly endothermic reactions [67, 68]. An estimated 10–15% reduction in the energy requirement is expected for POM compared to the typical SRM processes [46].
- The capability to produce syngas with a H_2/CO molar ratio of ~2, which is suitable for downstream processes such as methanol synthesis, FTs, etc. In contrast, the syngas produced via either SRM and/or DRM needs to be adjusted to a suitable H_2/CO ratio before used in the downstream processes [69, 70].
- It can be carried out under high gas hourly space velocity (GHSV), which means less investment and less production scale to achieve the same capacity [70]. An estimated 25–30% lower capital investment is expected for POM compared to the typical SRM processes [46]. In fact, while in the SRM the contact time is of the order of seconds, in the POM the contact time is of the order of milliseconds [30].
- High conversion and selectivity at lower process temperature [71].
- It is considerably faster [72].

Because of the characteristics outlined above, POM has attracted special attention and represents the most compelling technology for syngas production [73-75].

1.3.3.4 Autothermal reforming of methane (ATR)

The process known as autothermal reforming (ATR) combines POM and SRM processes. Actually, the feed is made up of methane, oxygen, and water in a proportion that can cause the process to become autothermal and stop coke formation [76]. The balanced equation can be represented by the following equation [77]:

$$CH_4 + 2O_2 + H_2O \longrightarrow CO + 4H_2 + H_2O \qquad \Delta H°_{298K} = -36 \text{ kJ mol}^{-1} \qquad \text{(Eq–1.17)}$$

The typical ATR mechanism is illustrated in Fig–1.11. Moreover, ATR process includes a heating phase within the reactor, where the exothermic oxidation events take place in the first section of the catalytic bed and produce heat for endothermic activities in the remaining area [78]. Adding steam allows for lower temperatures and higher syngas selectivity than what is available with POM [30]. A steam addition also limits the growth of carbon coke and the presence of hot patches in the catalytic bed because the reforming reactions enhance the overlapping of the oxidation events. It is obvious that the contact times in the catalytic bed are lengthened by the presence of water (about one tenth of second) [79]. As a result, the employment of compact reactors, as in the oxidation process, is not an option. However, compared to the reactors used in reforming reactions, the ones used in ATR are rather small [80].

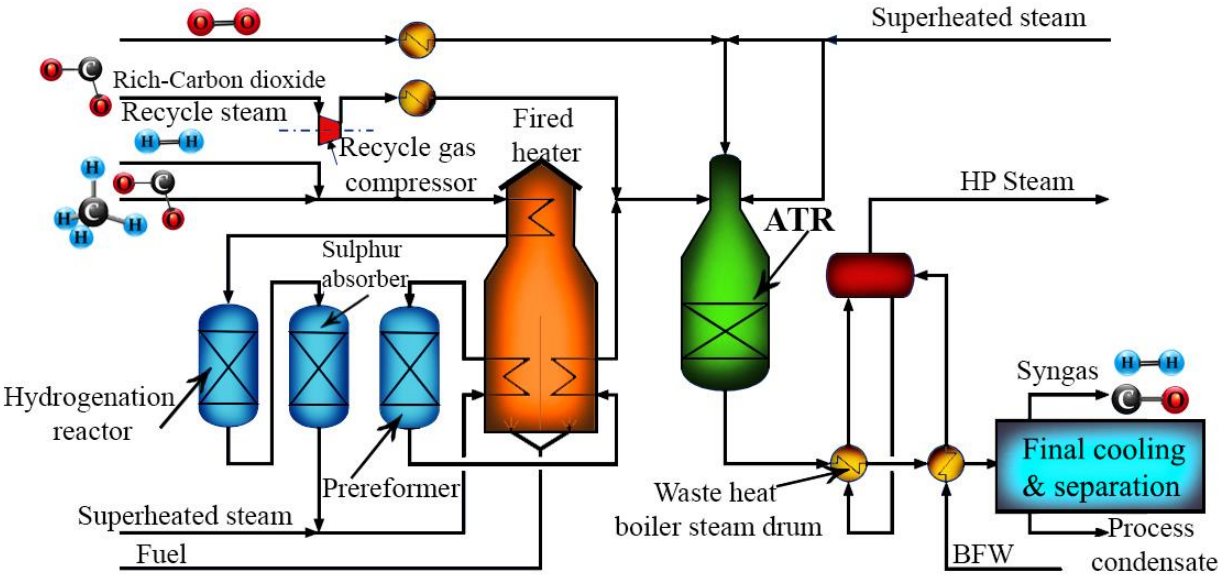

Fig-1. 11: Typical ATR process for syngas production. Redrawn from [81].

1.4 Mechanism of the catalytic partial oxidation of methane

Two different reaction mechanisms have been proposed to explain the POM process:

1. Direct partial oxidation of methane (DPOM),
2. Two-steps catalytic partial oxidation of methane mechanism (CPOM).

1.4.1 Direct partial oxidation of methane (DPOM)

Hickman et al. [79] demonstrated that both H_2 and CO are primary products of the direct partial oxidation of methane (DPOM) at high temperatures and an extremely short contact time, in contrast to previous proposals that the generation of syngas would occur via a sequence of total oxidation followed by reforming (in the order of milliseconds). The mechanism, according to one theory, entailed direct synthesis of H_2 caused by CH_4 on catalyst surfaces, producing surface C and H species. While the surface C atoms react with adsorbed O atoms and desorb as CO, the H atoms dimerize and desorb as H_2.

1.4.2 Two-steps catalytic partial oxidation of methane (CPOM) mechanism

Ashcroft et al. [82-86] reported that the POM process into syngas occurs in two steps. In the first step, CH_4 is combusted by O_2 to produce CO_2 and H_2O and then the remaining unreacted CH_4 is reformed with water and CO_2 to produce CO and H_2. Therefore, they suggested that the reaction pathway may involve initial total oxidation of some CH_4 to CO_2 and H_2O, followed by a sequence of SRM and DRM reactions

of unconverted CH_4 to syngas and reverse WGS reactions to give equilibrium product yields:

$CH_4 + 2O_2 \rightarrow CO_2 + 2H_2O$ $\Delta H°_{298K}$=–803 kJ mol^{-1} (Eq–1.16)

$CH_4 + H_2O \rightarrow CO + 3H_2$ $\Delta H°_{298K}$=206 kJ mol^{-1} (Eq–1.6)

$CH_4 + CO_2 \rightarrow 2H_2 + 2CO$ $\Delta H°_{298K}$=247 kJ mol^{-1} (Eq–1.7)

$CO + H_2O \rightleftarrows CO_2 + H_2$ $\Delta H°_{298K}$=-41.2 kJ mol^{-1} (Eq–1.11)

In practice, the syngas production via POM process will typically be at or very close to the equilibrium of the reforming and WGS reactions [54]. This is commonly called the "indirect or two-steps partial oxidation mechanism", also known as the combustion-reforming mechanism, and, as a result, a temperature profile along the reactor, with a peak temperature close to the entrance, is usually observed [52, 87]. Fig–1.12 indicates the typical scheme of CPOM process.

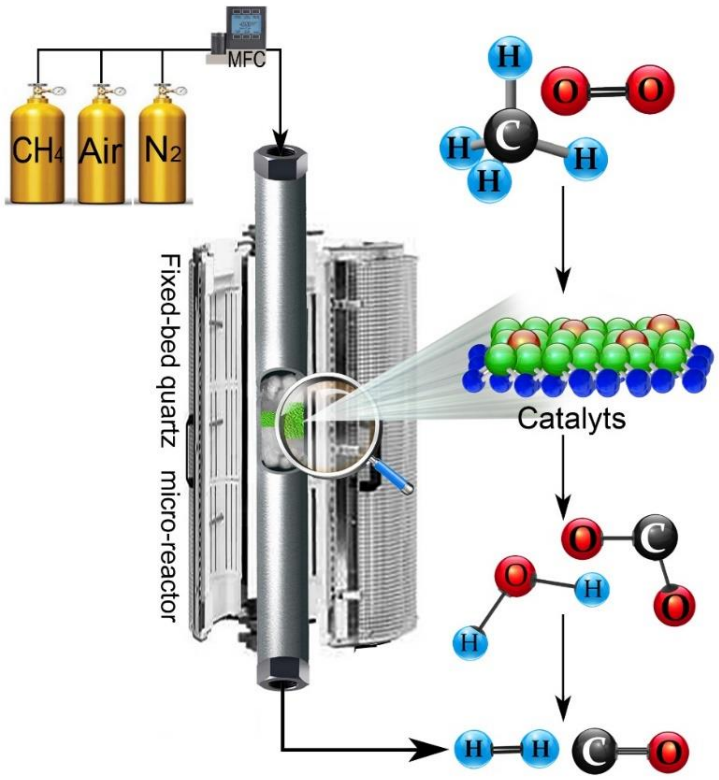

Fig-1. 12: Schematic of catalytic partial oxidation of methane (CPOM) to syngas.

1.4.2.1 Catalysts for the catalytic partial oxidation of methane (CPOM)

Most early studies in the CPOM (before the middle of the 1980s) focused on Ni catalysts, which are frequently employed for SRM process. Ashcroft and colleagues made a substantial contribution to CPOM in the 1990s [82, 83, 85, 88] and tested a variety of catalyst compositions for syngas production in a series of four articles. In addition, the CPOM over metallic catalysts had been briefly reviewed by Green et al. [89], therefore, the catalysts used for POM process can be divided basically into three main types [90-92]:

1. Base metal nickel (Ni), cobalt (Co) and iron (Fe) catalysts,
2. Noble metal catalysts (Ru, Rh, Pd, etc.),
3. Transition metal carbide catalysts.

Currently, the industrial catalysts used for POM are primarily nickel and noble metal supported catalysts [93].

1.4.2.1.1 Nickel–based catalysts

Nickel, cobalt and iron catalysts were widely studied because of considerable activity, good stability, and low cost [90]. Co and Fe catalysts have a much lower performance with respect to Ni for the CPOM process. Moreover, Ni has been extensively employed as an active metal in catalytic processes, and is currently the preferred choice for the commercial SRM [52, 54]. Ni–based catalysts in the CPOM exhibit good syngas production activity that is comparable to Pt behavior [94]; however, under certain operating conditions, the disadvantages of Ni-based catalysts is deactivation, which may occur due to sintering and causes metal loss and carbon deposition at temperatures higher than 700 °C [89, 95].

Surface oxidation of Ni to NiO may occur due to the presence of oxygen in the feed stream. The NiO formation during reaction may not only enhance combustion reactions but also interact with the catalyst support to form, for example, nickel aluminates when alumina is used as support or NiO–MgO solid solutions with MgO as support [92, 94, 96]. It was reported that formation of a solid solution in the Ni–MgO system and the weak basicity of MgO decreases carbon deposition [55, 97].

Choudhary et al. [98, 99] studied NiO catalysts supported on MgO, CaO, Al_2O_3, SiO_2 and rare earth oxides. The results indicated that when supported on CaO, the catalyst could maintain a high efficiency for long times with no apparent carbon deposition. Dissanayake and co-workers [100] studied POM reaction over 25 wt.% of Ni/Al_2O_3 in the temperature range 450~900ºC. They found that CH_4 was almost completely converted with about 95% of syngas selectivity when temperature was over 700°C, with a CO selectivity beyond 95%. They also found that three regions exist in the catalyst bed with different states of the catalyst: $NiAl_2O_4$, NiO/Al_2O_3 and supported nickel metal particles [100]. High syngas selectivity over this catalyst bed suggests that CPOM over supported Ni catalysts proceeds via combustion followed by SRM and DRM. However, to solve the major technical problem of the nickel-based catalysts which is carbon deposition on the catalyst, several strategies have been utilized to improve thermal stability, activity and decrease carbon deposition. Some of these strategies include preparing catalysts with different methods [94], selecting appropriate different oxide supports (e.g. CaO, TiO_2, Y_2O_3, ZrO_2, ThO_2 and UO_2 [98, 101, 102], promoting the catalysts with noble metals and non–noble metals [103, 104], addition of promoters with basic properties [105, 106], utilization of supports with high thermal conductivities [107, 108], and improving the oxygen-storage properties of the catalysts by promotion with rare earth metal oxides [109,

110]. Rare earth metal oxides or alkaline metal oxides as supports can restrict carbon formation of the supported Ni catalysts [111, 112]. This promotion is attributed to the capability for O_2 storage of these rare earth metal and alkaline metal oxides, which help to oxidize the surface carbon deposited [111]. Despite large efforts towards modification of the Ni catalysts, carbon deposition still cannot be completely avoided. To suppress carbon formation is still a subject of many studies today.

1.4.2.1.2 Noble metal catalysts

Noble metals such as Rh, Ru, Pd, Pt, Ir, etc. have been widely studied in the last three decades, and they are primarily employed for CPOM process to syngas production, because they can be directly used as catalyst [113]. They have many advantages with respect to Ni–based catalysts, such as more active, less sensitive to coke formation, and higher capacity to oxidize hydrocarbons, and strong resistant to catalyst deactivation and metal evaporation [94, 114], but they are much more expensive.

Green and co–workers [63, 86] showed that for stoichiometric partial oxidation with air, high methane conversion (~ 94%) and high syngas yield (H_2~ 99%, CO~ 97%) can be obtained at ~ 775 °C and 1 atm over nearly all the noble metal catalysts, as well as over rare earth ruthenium pyrochlores. Hickman et al. [79, 115, 116] and Poirier et al. [117] studied the CPOM over Rh catalysts and Pt–Pd catalysts, respectively, at extremely high flow rates. They reported that these noble metal catalysts, even with very low metal loadings, were much more active than Ni catalysts. It was also shown by Horn et al. [118] that CH_4 could be converted into syngas with very high syngas selectivity on Rh and Pt foam catalysts. Kunimori et al. [119, 120] found that $RhVO_4$–SiO_2 and Rh–SiO_2 are all excellent catalysts for POM,

with 90% of CH_4 conversion at 700°C. Schimidt et al. [121] compared activities of monolith-supported Rh, Pt, Ir, Pd, Ni, Fe, Co, and Re catalysts. The best CH_4 conversion was achieved (~ 89 %) on Ru at 1000 °C. In addition, these catalysts did not exhibit carbon deposition [71]. Among the noble metals, ruthenium and palladium are the most effective noble metals used for methane conversion processes [74, 122].

In general, low metal loadings have been used with noble metals because of their high cost, and usually they have been used as promoters [114]. Therefore, bimetallic catalysts with Ni and noble metals have been proposed to promote methane conversion [91, 95].

Bimetallic catalysts are attractive because the addition of the second metal modifies the structure and electronic properties of the monometallic catalyst [123, 124], which may increase the catalytic activity, improve the selectivity and suppress catalytic deactivation [125]. The bimetallic catalysts might consist of two noble metals [126], non–noble and noble [127, 128], as well as two non–noble metals [129]. Moreover, It has been reported that the activity and stability of nickel catalysts can be increased with the addition of low amounts of noble metals [90]. These promoting effects have been attributed to several factors: formation of an alloy, causing electronic changes in nickel; exposure of the noble metal by migration to the nickel surface; multi-functionality of the catalyst (the noble metal catalyzing partial oxidation and nickel catalyzing steam reforming); and a higher amount of metallic nickel exposed to the reaction, resulting from the promotion of nickel reduction by spillover [103, 104]. Only a few studies have been focused on the deactivation phenomena of nickel–based catalysts under realistic operating conditions and during extended periods of time (e.g. > 1000 h) [92].

Additionally, the choice of a proper support has been found crucial in addressing the catalytic performance, selectivity, and thermal stability of catalysts for the POM process [130, 131].The support plays also an important role in the POM process [130, 131]. Most catalysts show high activity when metals are dispersed on a reducible oxide support [89]. Typical supports are Al_2O_3 [70, 132] and CeO_2 [133]. Alumina is commonly adopted as a support material to maintain a good dispersion of the active metals. However, palladium catalysts supported on alumina are not stable at the high temperatures associated with CH_4 oxidation reactions. Rare earth and alkaline earth oxides are frequently added to enhance the thermal stability of both the support and the active metal. Cerium oxide (CeO_2) is one of the most significant reducible oxide supports used in industrial catalysis in order to low affinity towards carbon deposition due to its high oxygen storage within its crystal lattice, which can help to minimize coke formation on the catalyst surface [134]. Moreover, it is very effective as structural support and shows unique electronic properties, which can enhance the catalytic activity of metal species [135, 136]. The peculiar redox properties of CeO_2 involving the facile exchange between Ce^{3+} and Ce^{4+} states and the high mobility of O^{2-} ions in the lattice are the key factors to suppress carbon deposition [122, 135].

1.5 Catalysts preparation method

In recent years there has been a growing awareness of the importance of the environmentally friendly design of chemical products and processes. The concept of sustainability is strongly impacting the chemical community, which is more and more focusing on minimizing the use of hazardous substances and adopting green synthetic strategies from renewable, sustainable resources as starting materials [137]. Additionally, preparation of catalysts from several routes may have different internal structures that would affect the properties of materials consolidated from them [138]. Generally, the liquid route involves sol–gel and wet chemical methods, and the solid–state route preparation takes place via mechanical milling, also called mechanochemical synthesis.

However, each method has its own advantages and shortcomings, but among all the methods that can be employed for the preparation of catalysts, ball milling is an emerging technique, which allows avoiding organic solvents, being easy to use, fast, economical and environmentally friendly. This technique has recently acquired growing interest in heterogeneous catalysis [137, 139].

In this project, two different methods were used to prepare the catalysts, mechanochemical (dry ball mill, BM) and conventional incipient wetness impregnation (IWI). We especially focused on the applicability of ball milling for the preparation of the catalysts.

1.5.1 Dry ball milling (BM) technology

Around 150 years ago, Ostwald introduced mechanochemistry (MC) as part of physical chemistry, at the same level as thermochemistry, electrochemistry or photochemistry [140]. The International Union of Pure and Applied Chemistry (IUPAC) compendium of chemical terminology defines MC process as a ‘‘chemical reaction that is induced by mechanical energy’’ [141]. Nowadays, the MC technique is an important technological process which is widely used to grind powders into fine particles, and for mixing, blending, and dispersing. It is also used to induce structural disorder, amorphization and increased chemical reactivity in the material treated by intensive grinding [1, 142]. Besides, MC is a green technology with enormous potential for the preparation of catalysts. The entire process is characterized by small energy requirements and it is cost-effective, reproducible, and environmentally friendly [143]. The potential for contamination is a potential drawback of this technology [143]. Depending on the application, several types of milling equipment are available in the market, including ball mill, planetary ball mills or ring mills. They all operate on the same fundamental principles (Fig–1.13) [144].

According to the mode of activity, Gorrasi and Sorrentino [145] classify the milling processes into two groups: direct milling and indirect milling. In the direct milling technique, mechanical shafts or rollers directly transfer kinetic energy to the particles. In the indirect milling technique, the kinetic energy is firstly passed to the mill body and then to the grinding medium. Planetary and vibration milling are categorized in the indirect milling group, and ball mill and attritor (stirring ball mill) are direct BM techniques.

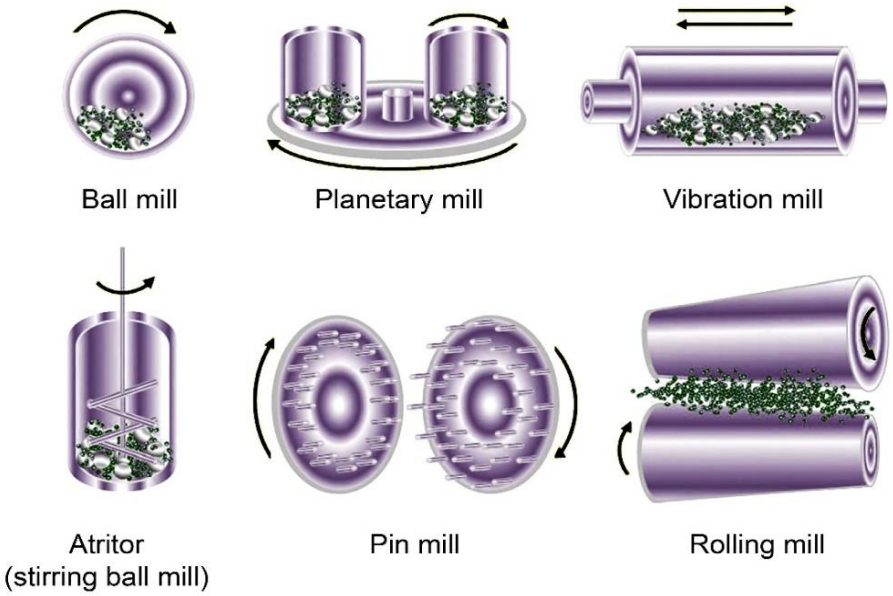

Fig-1. 13: Types of ball mills for high-energy milling. Modified from [1].

A number of factors can affect the milling process, including the type of milling material, ball to powder ratio (BPR), amount of material in the milling chamber, milling atmosphere, speed (energy), and time [137]. Currently, a variety of materials, including silicon nitride, zirconia (tetragonal ZrO_2 stabilized with Y_2O_3), agate (SiO_2), corundum, Cr–Ni steel, polyamide, and tungsten carbide, have been used to manufacture milling reactors and balls [1].

The most widely studied use of mechanochemistry prepared catalysts has been in the area of environmental catalysis and, in particular, for exhaust gas after treatment. As an example, Danielis et al. [146] successfully prepared Pd–CeO_2 catalysts using dry mechanochemical synthesis directly from metallic Pd and CeO_2.The resulting catalysts showed an outstanding activity in the oxidation of methane compared to their counterparts prepared by traditional incipient wetness impregnation. The milled samples also exhibited higher stability. They reported a particular architecture of the catalyst prepared by ball milling, which consisted of an amorphous Pd–Ce layer covering the ceria crystallites. Tao Gan et al. [147] reported a eco-friendly and

scalable ball milling method for the synthesis of Co alloyed Pt single-atom alloy catalysts at kilogram levels. The catalysts exhibit superior catalytic performance for the hydrodeoxygenation of hydroxymethylfurfural (HMF) to dimethylfuran (DMF), obtaining 100% HMF conversion and 92.9% selectivity to DMF under 1.0 MPa H_2 at 180 °C for 2 h. Moreover, Colussi et al. [148] studied Pd catalysts supported on CeO_2 prepared by dry ball mill, and their investigation proved that the catalysts could operate at high space velocity (480,000 h^{-1} GHSV) under a gas mixture containing CO, CO_2, and H_2O, which is known to inhibit methane oxidation and are always present in large quantities in natural gas fuel vehicles exhausts. Additionally, Li Yang et al. [149] prepared by dry ball milling a series of Pd catalysts with different Pd precursors (palladium chloride, nitrate, acetate and acetylacetonate) supported on SiO_2. Their investigation results indicate that the Pd dispersion and catalytic performance of the Pd–SiO_2 catalysts prepared by the dry ball-milling method are remarkably dependent on the Pd precursor, being the catalyst prepared from acetylacetonate the one with high dispersion of Pd species, superior resistance against sintering and superior catalytic performance in the lean methane oxidation. It can be concluded that dry ball milling is a simple but rather effective method to prepare catalysts with improved properties. This work describes for the first time the preparation, characterization, and testing of a series of monometallic and bimetallic catalysts prepared by dry ball milling for the partial oxidation of methane at low temperature.

1.6 Objectives

- The primary objective of this thesis is to develop an efficient and sustainable method for converting methane into syngas using the partial oxidation of methane (POM) process with suitable catalysts that can facilitate the conversion of methane into syngas with high selectivity and activity.
- To evaluate the catalytic activity and stability of monometallic Ni, Pd, and Ru and bimetallic Pd–Ni, Ru–Ni, and Ru–Pd catalysts supported on CeO_2 for the POM process to obtain syngas at low temperatures. The study aims to examine the performance of these catalysts under various conditions, and to investigate their potential for improving the efficiency of the conversion of methane. The study will also focus on the characterization and analysis of the catalysts to understand their physicochemical properties and their impact on the catalytic activity.
- Another important goal of this project is to compare the effectiveness of two different methods for preparing catalysts for the POM reaction, namely conventional incipient wetness impregnation (IWI) and dry ball milling (BM). The aim is to identify the most effective method for producing catalysts with optimal properties for the intended application.
- To investigate the impact of different metal types and metal loading ratios on the development of an active and selective catalyst system for the sustainable production of syngas via the POM process. The proposed catalyst system is expected to demonstrate economic feasibility and have potential for industrial applications.

1.7 References

1. Shamsul, N., et al., An overview on the production of bio-methanol as potential renewable energy. Renewable and Sustainable Energy Reviews, 2014. **33**: p. 578-588.
2. Jeffry, L., et al., Greenhouse gases utilization: A review. Fuel, 2021. **301**: p. 121017.
3. Zakaria, Z. and S.K. Kamarudin, Direct conversion technologies of methane to methanol: An overview. Renewable and Sustainable Energy Reviews, 2016. **65**: p. 250-261.
4. Agency, E.U.S.E.P. Climate Change Indicators: Atmospheric Concentrations of Greenhouse Gases 2022, July; Available from: https://www.epa.gov/climate-indicators/climate-change-indicators-atmospheric-concentrations-greenhouse-gases.
5. Agency, E.U.S.E.P. Global Greenhouse Gas Emissions Data 2022, February; Available from: https://www.epa.gov/ghgemissions/global-greenhouse-gas-emissions-data.
6. Mokhta, Z.M., et al., Simulation studies on microwave-assisted pyrolysis of biomass for bioenergy production with special attention on waveguide number and location. Energy, 2020. **190**: p. 116474.
7. Ma, Z., et al., Temperature effects on redox potentials and implications to semiconductor photocatalysis. Fuel, 2021. **286**: p. 119490.
8. Dębek, R.. Novel catalysts for chemical CO_2 utilization. A thesis. Mechanical Science, l'AGH University of Science and Technology (Cracovie, Pologne). (2016). Paris 6.

9. (IPCC), T.I.P.o.C.C. Framing and Context. 2022, June; Available from: https://www.ipcc.ch/sr15/chapter/chapter-1/.
10. Worldometer. Current World Population. 2022, August; Available from: https://www.worldometers.info/world-population/.
11. Dębek, R., et al., Promotion effect of zirconia on Mg (Ni, Al) O mixed oxides derived from hydrotalcites in CO_2 methane reforming. Applied Catalysis B: Environmental, 2018. **223**: p. 36-46.
12. Ong, M.Y., et al., Optimization and kinetic study of non-catalytic transesterification of palm oil under subcritical condition using microwave technology. Energy Conversion and Management, 2019. **196**: p. 1126-1137.
13. Nations, D.o.E.a.S.A.U. Energy Transition. 2021; Available from: https://webcache.googleusercontent.com/search?q=cache:7XohPRYZn0wJ:https://www.un.org/sites/un2.un.org/files/2021-twg_2-062321.pdf&cd=1&hl=ca&ct=clnk&gl=es.
14. Zavala-Araiza, D., et al., Reconciling divergent estimates of oil and gas methane emissions. Proceedings of the National Academy of Sciences, 2015. **112**(51): p. 15597-15602.
15. Ying, G., et al., Quantitative analysis of main components of natural gas based on Raman spectroscopy. Chinese Journal of Analytical Chemistry, 2019. **47**(1): p. 67-76.
16. Yin, J., et al., Thermodynamic characteristics of a low concentration methane catalytic combustion gas turbine. Applied Energy, 2010. **87**(6): p. 2102-2108.
17. Wuebbles, D.J. and K. Hayhoe, Atmospheric methane and global change. Earth-Science Reviews, 2002. **57**(3-4): p. 177-210.

18. European Commission, E. (2022). "EU economy greenhouse gas emissions." from https://ec.europa.eu/eurostat/web/products-eurostat-news/w/DDN-20230515-2.
19. Ueno, Y. and Kitajima, Y. (2014) Suppression of Methane Gas Emissions and Analysis of the Electrode Microbial Community in a Sediment-Based Bio-Electrochemical System. Advances in Microbiology, **4**: p. 252-266.
20. Reddy, P.V.L., K.-H. Kim, and H. Song, Emerging green chemical technologies for the conversion of CH_4 to value added products. Renewable and Sustainable Energy Reviews, 2013. **24**: p. 578-585.
21. Change, U.N.C. The Paris Agreement. 2022, December; Available from: https://unfccc.int/process-and-meetings/the-paris-agreement/the-paris-agreement.
22. Lunsford, J.H., Catalytic conversion of methane to more useful chemicals and fuels: a challenge for the 21st century. Catalysis today, 2000. **63**(2-4): p. 165-174.
23. Loktev, A., et al., Novel High-Performance Catalysts for Partial Oxidation and Dry Reforming of Methane to Synthesis Gas. Petroleum Chemistry, 2022. **62**(5): p. 526-543.
24. Zhu, Z., et al., Research progress on methane conversion coupling photocatalysis and thermocatalysis. Carbon Energy, 2021. **3**(4): p. 519-540.
25. Liu, S., et al., “Soft” oxidative coupling of methane to ethylene: Mechanistic insights from combined experiment and theory. Proceedings of the National Academy of Sciences, 2021. **118**(23): p. e2012666118.
26. Ravi, M., M. Ranocchiari, and J.A. van Bokhoven, The direct catalytic oxidation of methane to methanol—A critical assessment. Angewandte Chemie International Edition, 2017. **56**(52): p. 16464-16483.

27. Wang, K., et al., Summary of research progress on separation and extraction of valuable metals from Bayer red mud. Environmental Science and Pollution Research, 2022: p. 1-19.

28. Deka, T.J., et al., Methanol fuel production, utilization, and techno-economy: a review. Environmental Chemistry Letters, 2022: p. 1-30.
29. Specchia, S., et al., Syngas production by short contact time catalytic partial oxidation of methane. Nova Science: New York, 2011.
30. Lustemberg, P.G., et al., Tuning Selectivity in the Direct Conversion of Methane to Methanol: Bimetallic Synergistic Effects on the Cleavage of C–H and O–H Bonds over NiCu/CeO_2 Catalysts. TheJournal of Physical Chemistry Letters, 2022. **13**(24): p. 5589-5596.
31. Lustemberg, P.G., et al., Direct conversion of methane to methanol on Ni-Ceria surfaces: metal–support interactions and water-enabled catalytic conversion by site blocking. Journal of the American Chemical Society, 2018. **140**(24): p. 7681-7687.
32. Farrell, B.L., V.O. Igenegbai, and S. Linic, A viewpoint on direct methane conversion to ethane and ethylene using oxidative coupling on solid catalysts. 2016, ACS Publications. p. 4340-4346.
33. Schwach, P., X. Pan, and X. Bao, Direct conversion of methane to value-added chemicals over heterogeneous catalysts: challenges and prospects. Chemical reviews, 2017. **117**(13): p. 8497-8520.
34. Jašo, S., H. Arellano-Garcia, and G. Wozny, Oxidative coupling of methane in a fluidized bed reactor: Influence of feeding policy, hydrodynamics, and reactor geometry. Chemical Engineering Journal, 2011. **171**(1): p. 255-271.

35. Li, Q., et al., Experimental study and kinetics modeling of partial oxidation reactions in heavily sooting laminar premixed methane flames. Chemical Engineering Journal, 2012. **207**: p. 235-244.
36. Keller, G. and M. Bhasin, Synthesis of ethylene via oxidative coupling of methane: I. Determination of active catalysts. Journal of Catalysis, 1982. **73**(1): p. 9-19.
37. Fang, T. and C.-t. Yeh, Interactions of methane with ThO_2SiO_2 surface at 1073 K. Journal of Catalysis, 1981. **69**(1): p. 227-229.
38. Pyatnitskii, Y.I., Contemporary methods for the direct catalytic conversion of methane. Theoretical and Experimental Chemistry, 2003. **39**(4): p. 201-218.
39. Baerns, M., K. van der Wiele, and J.R. Ross, Methane activation-a bibliography. Catalysis today, 1989. **4**(3-4): p. 471-494.
40. Park, M.B., E.D. Park, and W.-S. Ahn, Recent progress in direct conversion of methane to methanol over copper-exchanged zeolites. Frontiers in Chemistry, 2019. **7**: p. 514.
41. Brown, M. and N. Parkyns, Progress in the partial oxidation of methane to methanol and formaldehyde. Catalysis Today, 1991. **8**(3): p. 305-335.
42. Alvarez-Galvan, M., et al., Direct methane conversion routes to chemicals and fuels. Catalysis Today, 2011. **171**(1): p. 15-23.
43. Fischer, F. and H. Tropsch, Über die Synthese höherer Glieder der aliphatischen Reihe aus Kohlenoxyd. Berichte der deutschen chemischen Gesellschaft (A and B Series), 1923. **56**(11): p. 2428-2443.
44. Dry, M.E., The Fischer–Tropsch (FT) Synthesis Processes. Handbook of Heterogeneous Catalysis: Online, 2008.

45. Bharadwaj, S. and L.D. Schmidt, Catalytic partial oxidation of natural gas to syngas. Fuel Processing Technology, 1995. **42**(2-3): p. 109-127.
46. Freni, S., G. Calogero, and S. Cavallaro, Hydrogen production from methane through catalytic partial oxidation reactions. Journal of Power Sources, 2000. **87**(1-2): p. 28-38.
47. Fakeeha, A.H., A.S. Al-Fatesh, and A.E. Abasaeed, Modification of alumina support with TiO_2-P_{25} in CO_2 reforming of CH_4. Journal of Industrial and Engineering Chemistry, 2012. **18**(1): p. 212-217.
48. Cheng, Z., et al., Role of support in CO_2 reforming of CH_4 over a Ni/γ-Al_2O_3 catalyst. Applied Catalysis A: General, 2001. **205**(1-2): p. 31-36.
49. Moral, A., et al., Partial oxidation of methane to syngas using Co/Mg and Co/Mg-Al oxide supported catalysts. Catalysis Today, 2019. **333**: p. 259-267.
50. Krisnandi, Y.K., et al., Partial oxidation of methane to methanol over heterogeneous catalyst Co/ZSM-5. Procedia Chemistry, 2015. **14**: p. 508-515.
51. Christiansen, L.J. and J. Rostrup-Nielsen, Concepts in Syngas Manufacture (Catalytic Science Series). 2011: World Scientific.
52. de Klerk, A., Oryx and Escravos Gas-to-Liquids Facilities. Fischer–Tropsch Refining Wiley-VCH Verlag GmbH & Co. KGaA, 2011: p. 241-248.
53. Aasberg-Petersen, K., et al., Natural gas to synthesis gas–catalysts and catalytic processes. Journal of Natural Gas Science and Engineering, 2011. **3**(2): p. 423-459.
54. Zhu, J., Catalytic partial oxidation of methane to synthesis gas over ZrO_2-based defective oxides. Enschede: Printpartners Ipskamp BV, 2005.

55. Usman, M., W.W. Daud, and H.F. Abbas, Dry reforming of methane: Influence of process parameters—A review. Renewable and Sustainable Energy Reviews, 2015. **45**: p. 710-744.
56. Oyama, S.T., et al., Dry reforming of methane has no future for hydrogen production: Comparison with steam reforming at high pressure in standard and membrane reactors. International Journal of Hydrogen Energy, 2012. **37**(13): p. 10444-10450.
57. Olah, G.A., et al., Bi-reforming of methane from any source with steam and carbon dioxide exclusively to metgas ($CO–2H_2$) for methanol and hydrocarbon synthesis. Journal of the American Chemical Society, 2013. **135**(2): p. 648-650.
58. Joensen, F. and J.R. Rostrup-Nielsen, Conversion of hydrocarbons and alcohols for fuel cells. Journal of Power Sources, 2002. **105**(2): p. 195-201.
59. Rostrup-Nielsen, J.R., Catalytic steam reforming, in Catalysis. 1984, Springer. p. 1-117.
60. Minh, D.P., et al., Review on the catalytic tri-reforming of methane-Part I: Impact of operating conditions, catalyst deactivation and regeneration. Applied Catalysis A: General, 2021. **621**: p. 118202.
61. Lercher, J., et al., Methane utilisation via synthesis gas generation-catalytic chemistry and technology, in Environmental Catalysis. 1999, World Scientific. p. 103-126.
62. Tsang, S., J. Claridge, and M. Green, Recent advances in the conversion of methane to synthesis gas. Catalysis Today, 1995. **23**(1): p. 3-15.
63. Xu, G., et al., Studies of reforming natural gas with carbon dioxide to produce synthesis gas: X. The role of CeO_2 and MgO promoters. Journal of Molecular Catalysis A: Chemical, 1999. **147**(1-2): p. 47-54.

64. Aramouni, N.A.K., et al., Catalyst design for dry reforming of methane: Analysis review. Renewable and Sustainable Energy Reviews, 2018. **82**: p. 2570-2585.
65. Prettre, M., C. Eichner, and M. Perrin, The catalytic oxidation of methane to carbon monoxide and hydrogen. Transactions of the Faraday Society, 1946. **42**: p. 335b-339.
66. Tang, S., J. Lin, and K. Tan, Partial oxidation of methane to synthesis gas over α-Al_2O_3-supported bimetallic Pt–Co catalysts. Catalysis Letters, 1999. **59**(2): p. 129-135.
67. Xie, J., et al., Autothermal reforming and partial oxidation of n-hexadecane via Pt/Ni bimetallic catalysts on ceria-based supports. International Journal of Hydrogen Energy, 2015. **40**(27): p. 8510-8521.
68. Drago, R.S., et al., Partial oxidation of methane to syngas using NiO-supported catalysts. Catalysis letters, 1998. **51**(3): p. 177-181.
69. Maniecki, T.P., et al., Effect of the chemical composition of (MgO) x (Al_2O_3) y support on the catalytic performance of Ni and Ni–Au catalysts for the partial oxidation of methane. Chemical Engineering Journal, 2009. **154**(1-3): p. 142-148.
70. Khajenoori, M., M. Rezaei, and B. Nematollahi, Preparation of noble metal nanocatalysts and their applications in catalytic partial oxidation of methane. Journal of Industrial and Engineering Chemistry, 2013. **19**(3): p. 981-986.
71. Korup, O., et al., Catalytic partial oxidation of methane on platinum investigated by spatial reactor profiles, spatially resolved spectroscopy, and microkinetic modeling. Journal of Catalysis, 2013. **297**: p. 1-16.
72. Bruno, T., et al., A study of methane partial oxidation in annular reactor: activity of Rh/α-Al_2O_3 and Rh/ZrO_2 catalysts. Catalysis today, 2005. **99**(1-2): p. 89-98.

73. Colussi, S., et al., Nanofaceted Pd–O Sites in Pd–Ce Surface Superstructures: Enhanced Activity in Catalytic Combustion of Methane. Angewandte Chemie International Edition, 2009. **48**(45): p. 8481-8484.
74. Navarro, R.M., M. Pena, and J. Fierro, Hydrogen production reactions from carbon feedstocks: fossil fuels and biomass. Chemical reviews, 2007. **107**(10): p. 3952-3991.
75. Williams, J., et al., Heterogeneous numerical modelling for the auto thermal reforming of crude glycerol in a fixed bed reactor. Chinese Journal of Chemical Engineering, 2022. **42**: p. 261-268.
76. Dybkjær, I., Tubular reforming and autothermal reforming of natural gas—an overview of available processes. Fuel Processing Technology, 1995. **42**(2-3): p. 85-107.
77. Madsen, S.W. SYNCOR™ - AUTOTHERMAL REFORMER (ATR). 2022; Available from: https://www.topsoe.com/our-resources/knowledge/our-products/process-licensing/syncortm-autothermal-reformer-atr.
78. Semelsberger, T.A., et al., Equilibrium products from autothermal processes for generating hydrogen-rich fuel-cell feeds. International Journal of Hydrogen Energy, 2004. **29**(10): p. 1047-1064.
79. Hickman, D. and L. Schmidt, Production of syngas by direct catalytic oxidation of methane. Science, 1993. **259**(5093): p. 343-346.
80. Hagh, B.F., Optimization of autothermal reactor for maximum hydrogen production. International Journal of Hydrogen Energy, 2003. **28**(12): p. 1369-1377.

81. Jones, R.H., et al., Catalytic conversion of methane to synthesis gas over europium iridate, $Eu_2Ir_2O_7$: An in situ study by X–ray diffraction and mass spectrometry. Catalysis letters, 1991. **8**(2): p. 169-174.
82. Claridge, J.B., et al., A study of carbon deposition on catalysts during the partial oxidation of methane to synthesis gas. Catalysis Letters, 1993. **22**(4): p. 299-305.
83. Vernon, P.D., et al., Partial oxidation of methane to synthesis gas. Catalysis Letters, 1990. **6**(2): p. 181-186.
84. Ashcroft, A., A.K. Cheetham, and M. Green, Partial oxidation of methane to synthesis gas using carbon dioxide. Nature, 1991. **352**(6332): p. 225-226.
85. Ashcroft, A., et al., Selective oxidation of methane to synthesis gas using transition metal catalysts. Nature, 1990. **344**(6264): p. 319-321.
86. De Groote, A.M. and G.F. Froment, Simulation of the catalytic partial oxidation of methane to synthesis gas. Applied Catalysis A: General, 1996. **138**(2): p. 245-264.
87. Ashcroft, A., et al., Selective oxidation of methane to synthesis gas using transition metal catalysts. Nature, 1990. **344**(6264): p. 319-321.
88. York, A.P., T. Xiao, and M.L. Green, Brief overview of the partial oxidation of methane to synthesis gas. Topics in Catalysis, 2003. **22**(3): p. 345-358.
89. Fazlikeshteli, S., X. Vendrell, and J. Llorca, Low-Temperature Methane Partial Oxidation over Pd Supported on CeO_2: Effect of the Preparation Method and Precursors. Reactions, 2021. **2**(1): p. 30-42.
90. Koh, A.C., et al., Hydrogen or synthesis gas production via the partial oxidation of methane over supported nickel–cobalt catalysts. International Journal of Hydrogen Energy, 2007. **32**(6): p. 725-730.

91. Enger, B.C., R. Lødeng, and A. Holmen, A review of catalytic partial oxidation of methane to synthesis gas with emphasis on reaction mechanisms over transition metal catalysts. Applied Catalysis A: General, 2008. **346**(1-2): p. 1-27.
92. Li, B., et al., Synthesis gas production from partial oxidation of methane over highly dispersed Pd/SiO_2 catalyst. Fuel, 2013. **103**: p. 1032-1038.
93. Lanza, R., J.A. Velasco, and S.G. Järås, Recent developments and achievements in partial oxidation of methane with and without addition of steam. Vol. 23. 2011: The Royal Society of Chemistry: Cambridge, UK.
94. Rostrup-Nielsen, J.R., Fuels and energy for the future: the role of catalysis. Catalysis reviews, 2004. **46**(3-4): p. 247-270.
95. ROSTRUP, J., Catalyst deactivation in synthesis gas production, and important syntheses. Deactivation and Poisoning of Catalysts, 1985. **20**: p. 259.
96. Tang, S., J. Lin, and K. Tan, Partial oxidation of methane to syngas over Ni/MgO, Ni/CaO and Ni/CeO_2. Catalysis Letters, 1998. **51**(3): p. 169-175.
97. Choudhary, V., V. Rane, and A. Rajput, Beneficial effects of cobalt addition to Ni-catalysts for oxidative conversion of methane to syngas. Applied Catalysis A: General, 1997. **162**(1-2): p. 235-238.
98. Choudhary, V., B. Uphade, and A. Mamman, Oxidative conversion of methane to syngas over nickel supported on commercial low surface area porous catalyst carriers precoated with alkaline and rare earth oxides. Journal of Catalysis, 1997. **172**(2): p. 281-293.
99. Dissanayake, D., et al., Partial oxidation of methane to carbon monoxide and hydrogen over a Ni/Al_2O_3 catalyst. Journal of Catalysis, 1991. **132**(1): p. 117-127.

100. Choudhary, V., A. Rajput, and B. Prabhakar, Low temperature oxidative conversion of methane to syngas over NiO-CaO catalyst. Catalysis Letters, 1992. **15**(4): p. 363-370.

101. Choudhary, V.R., A.M. Rajput, and V.H. Rane, Low-temperature catalytic selective partial oxidation of methane to carbon monoxide and hydrogen over nickel/ytterbium sesquioxide. The Journal of Physical Chemistry, 1992. **96**(22): p. 8686-8688.

102. Dias, J.A. and J.M. Assaf, Autothermal reforming of methane over Ni/γ-Al_2O_3 catalysts: the enhancement effect of small quantities of noble metals. Journal of Power Sources, 2004. **130**(1-2): p. 106-110.

103. Mukainakano, Y., et al., Catalytic performance and QXAFS analysis of Ni catalysts modified with Pd for oxidative steam reforming of methane. Catalysis Today, 2008. **132**(1-4): p. 101-108.

104. Takehira, K., "Intelligent" reforming catalysts: Trace noble metal-doped Ni/Mg (Al) O derived from hydrotalcites. Journal of Natural Gas Chemistry, 2009. **18**(3): p. 237-259.

105. Souza, M.M., et al., Autothermal reforming of methane over nickel catalysts prepared from hydrotalcite-like compounds, in Studies in Surface Science and Catalysis. 2007, Elsevier. p. 451-456.

106. Santos, D.C., L. Madeira, and F.B. Passos, The effect of the addition of Y_2O_3 to Ni/α-Al_2O_3 catalysts on the autothermal reforming of methane. Catalysis Today, 2010. **149**(3-4): p. 401-406.

107. Liu, H. and D. He, Properties of Ni/Y_2O_3 and its catalytic performance in methane conversion to syngas. International Journal of Hydrogen Energy, 2011. **36**(22): p. 14447-14454.

108. Cai, X., X. Dong, and W. Lin, Effect of CeO_2 on the catalytic performance of Ni/Al_2O_3 for autothermal reforming of methane. Journal of Natural Gas Chemistry, 2008. **17**(1): p. 98-102.

109. Pompeo, F., D. Gazzoli, and N.N. Nichio, Stability improvements of Ni/α-Al_2O_3 catalysts to obtain hydrogen from methane reforming. International Journal of Hydrogen Energy, 2009. **34**(5): p. 2260-2268.

110. Liu, S., et al., Sustainable Ni catalyst for partial oxidation of CH_4 to syngas at high temperature, in Studies in Surface Science and Catalysis. 2000, Elsevier. p. 3567-3572.

111. Slagtern, Å. and U. Olsbye, Partial oxidation of methane to synthesis gas using La-MO catalysts. Applied Catalysis A: General, 1994. **110**(1): p. 99-108.

112. Tan, L., et al., Liquid-phase hydrogenation of N-nitrosodimethylamine over Pd-Ni supported on CeO_2-TiO_2: The role of oxygen vacancies. Colloids and Surfaces A: Physicochemical and Engineering Aspects, 2018. **558**: p. 211-218.

113. Burch, R. and F. Urbano, Investigation of the active state of supported palladium catalysts in the combustion of methane. Applied Catalysis A: General, 1995. **124**(1): p. 121-138.

114. Hickman, D., E. Haupfear, and L. Schmidt, Synthesis gas formation by direct oxidation of methane over Rh monoliths. Catalysis Letters, 1993. **17**(3): p. 223-237.

115. Hickman, D. and L.D. Schmidt, Steps in CH4 oxidation on Pt and Rh surfaces: High-temperature reactor simulations. AIChE Journal, 1993. **39**(7): p. 1164-1177.

116. Poirier, M.G., J. Trudel, and D. Guay, Partial oxidation of methane over ruthenium catalysts. Catalysis Letters, 1993. **21**(1): p. 99-111.

117. Horn, R., et al., Methane catalytic partial oxidation on autothermal Rh and Pt foam catalysts: Oxidation and reforming zones, transport effects, and approach to thermodynamic equilibrium. Journal of Catalysis, 2007. **249**(2): p. 380-393.

118. Yamagishi, T., et al., Catalytic performance and characterization of $RhVO_4/SiO_2$ for hydroformylation and CO hydrogenation. Journal of Molecular Catalysis A: Chemical, 2006. **244**(1-2): p. 201-212.

119. Tomishige, K., M. Asadullah, and K. Kunimori, Syngas production by biomass gasification using $Rh/CeO_2/SiO_2$ catalysts and fluidized bed reactor. Catalysis Today, 2004. **89**(4): p. 389-403.

120. Torniainen, P., X. Chu, and L. Schmidt, Comparison of monolith-supported metals for the direct oxidation of methane to syngas. Journal of Catalysis, 1994. **146**(1): p. 1-10.

121. Fouladvand, S., et al., Methane oxidation over Pd supported on ceria–alumina under rich/lean cycling conditions. Topics in Catalysis, 2013. **56**(1-8): p. 410-415.

122. Chen, W., et al., Titanium-promoted $Rh-Mn-Li/SiO_2$ for C_2-oxygenates synthesis from syngas: effect of low titanium loading. Journal of Natural Gas Chemistry, 2005. **14**(4): p. 199-206.

123. Choudhary, V.R., K.C. Mondal, and S.A. Mulla, Simultaneous conversion of methane and methanol into gasoline over bifunctional Ga-, Zn-, In-, and/or Mo-modified ZSM-5 zeolites. Angewandte Chemie, 2005. **117**(28): p. 4455-4459.

124. Kriz, D.A., et al., Partial Oxidation of Methane to Synthesis Gas Using Supported Ga-Containing Bimetallic Catalysts and a Ti-Promoter. ChemCatChem, 2018. **10**(19): p. 4300-4308.

125. Kaila, R.K., et al., Zirconia-supported bimetallic RhPt catalysts: Characterization and testing in autothermal reforming of simulated gasoline. Applied Catalysis B: Environmental, 2008. **84**(1-2): p. 223-232.

126. Dias, J.A.C. and J.M. Assaf, Autoreduction of promoted Ni/γ-Al_2O_3 during autothermal reforming of methane. Journal of Power Sources, 2005. **139**(1-2): p. 176-181.

127. Nikolla, E., J. Schwank, and S. Linic, Promotion of the long-term stability of reforming Ni catalysts by surface alloying. Journal of Catalysis, 2007. **250**(1): p. 85-93.

128. Zhang, J., H. Wang, and A.K. Dalai, Development of stable bimetallic catalysts for carbon dioxide reforming of methane. Journal of Catalysis, 2007. **249**(2): p. 300-310.

129. Mattos, L.V., et al., Partial oxidation of methane on Pt/Ce–ZrO_2 catalysts. Catalysis Today, 2002. **77**(3): p. 245-256.

130. Luo, Z., et al., TiO_2 Supported gold–palladium catalyst for effective syngas production from methane partial oxidation. Applied Catalysis A: General, 2018. **554**: p. 54-63.

131. Zhu, J., D. Zhang, and K. King, Reforming of CH_4 by partial oxidation: thermodynamic and kinetic analyses. Fuel, 2001. **80**(7): p. 899-905.

132. Cifuentes, B., et al., Monoliths washcoated with AuCu catalysts for CO removal in an ethanol fuel processor: Effect of CeO_2–SiO_2 dual support on the catalytic performance and reactor cost. International Journal of Hydrogen Energy, 2021. **46**(2): p. 2166-2181.

133. Singha, R.K., et al., Effect of metal-support interaction on activity and stability of Ni-CeO_2 catalyst for partial oxidation of methane. Applied Catalysis B: Environmental, 2017. **202**: p. 473-488.

134. Ramírez-López, R., I. Elizalde-Martinez, and L. Balderas-Tapia, Complete catalytic oxidation of methane over Pd/CeO_2–Al_2O_3: The influence of different ceria loading. Catalysis Today, 2010. **150**(3-4): p. 358-362.

135. Wang, Y. and J. Zhang, Hydrogen production on Ni–Pd–Ce/γ-Al_2O_3 catalyst by partial oxidation and steam reforming of hydrocarbons for potential application in fuel cells. Fuel, 2005. **84**(14-15): p. 1926-1932.

136. Piras, C.C., S. Fernández-Prieto, and W.M. De Borggraeve, Ball milling: a green technology for the preparation and functionalisation of nanocellulose derivatives. Nanoscale Advances, 2019. **1**(3): p. 937-947.

137. Singh, K.K. and S. Bhattacharjee, Study on the effect of high energy ball milling (a nano material process) on the microstructure and mechanical properties of a (Al-Si-Fe-Cu) alloy. 2007.

138. Jiang, Y., et al., Photocatalytic methane conversion: insight into the mechanism of C (sp^3)-H bonds activation. CCS Chemistry, 2022: p. 1-55.

139. Ostwald, W., Lehrbuch der Allgemeinen Chemie, 1 Auflage, 2 Band. 1887, Leipzig.

140. McNaught, A.D. and A. Wilkinson, Compendium of chemical terminology. IUPAC recommendations. 1997.

141. McNaught, A.D. and A. Wilkinson, Compendium of chemical terminology. Vol. 1669. 1997: Blackwell Science Oxford.

142. Baláž, P., et al., Hallmarks of mechanochemistry: from nanoparticles to technology. Chemical Society Reviews, 2013. **42**(18): p. 7571-7637.

143. Baláž, P., Mechanochemistry in minerals engineering, in Mechanochemistry in nanoscience and minerals engineering. 2008, Springer. p. 257-296.

144. Dhiman, S., et al., A framework for effective and clean conversion of machining waste into metal powder feedstock for additive manufacturing. Cleaner Engineering and Technology, 2021. **4**: p. 100151.

145. Gorrasi, G. and A. Sorrentino, Mechanical milling as a technology to produce structural and functional bio-nanocomposites. Green Chemistry, 2015. **17**(5): p. 2610-2625.

146. Danielis, M., et al., Methane oxidation activity and nanoscale characterization of Pd/CeO_2 catalysts prepared by dry milling Pd acetate and ceria. Applied Catalysis B: Environmental, 2021. **282**: p. 119567.

147. Gan, T., et al., Facile synthesis of kilogram-scale Co-alloyed Pt single-atom catalysts via ball milling for hydrodeoxygenation of 5-hydroxymethylfurfural. ACS Sustainable Chemistry & Engineering, 2020. **8**(23): p. 8692-8699.

148. Danielis, M., et al., Pd/CeO_2 catalysts prepared by solvent-free mechanochemical route for methane abatement in natural gas fueled vehicles. Industrial & Engineering Chemistry Research, 2021. **60**(18): p. 6435-6445.

149. Yang, L., et al., Preparation of Pd/SiO_2 Catalysts by a Simple Dry Ball-Milling Method for Lean Methane Oxidation and Probe of the State of Active Pd Species. Catalysts, 2021. **11**(6): p. 725.

2. Materials and methods

2.1 Preparation of support and catalysts

2.1.1 CeO_2 support

Cerium nitrate hexahydrate ($Ce(NO_3)_3 \cdot 6H_2O$, 99.5%), and ammonia solution (NH_3, 28%) were purchased from Alfa Aesar, and Scharlab, respectively. All reagents were used without further purification. Cerium dioxide (CeO_2) was prepared by adding dropwise the ammonia solution to an aqueous solution of $Ce(NO_3)_3 \cdot 6H_2O$ until the pH reached a value between 9–10 and a yellowish precipitate was obtained. After that, the resulting product was filtered and washed thoroughly with deionized water. Finally, the precipitate was dried overnight at 90 °C and calcined at 650 °C for 4 hours (5 °C min^{-1}).

2.1.2 Monometallic Pd/CeO_2, $Pd(AC)/CeO_2$, Ni/CeO_2, and Ru/CeO_2 catalysts by mechanochemistry

Palladium (II) nitrate ($Pd(NO_3)_2$, 93%), and Nickel (II) nitrate hexahydrate ($Ni(NO_3)_2 \cdot 6H_2O$, 98%), were purchased from Alfa Aesar and Fisher chemical, respectively. Palladium (II) acetate ($Pd(CH_3COO)_2$, 47.5% Pd), and ruthenium (III) chloride ($RuCl_3$, 99.9%), were obtained from Acros Organics. All these metal precursors were used without further purification.

Monometallic xPd/CeO_2/BM, $xPd(AC)/CeO_2$/BM (using $Pd(NO_3)_2$ and $Pd(CH_3COO)_2$, respectively; x = 0.5 to 2 wt.%), xNi/CeO_2/BM (x = 0.5, 1 and 1.5 wt.%), and xRu/CeO_2/BM (x = 0.25, 0.5 and 1 wt.%) catalysts were prepared via dry ball mill (labeled as BM). The desired amounts of the metal precursors were mixed directly with 1 g of the CeO_2 support in a zirconium oxide vessel using a Fritsch Pulverisette 23 mini-mill apparatus and one zirconium oxide ball of 15 mm diameter (ball to powder ratio, BPR = 10.2). The effect of ball mill energy was explored in the range of 15–50 Hz, and the effect of milling time was studied in the range of 5-40 min.

2.1.3 Bimetallic Pd–Ni, Ru–Ni, and Ru–Pd catalysts supported on CeO_2 by mechanochemistry

Two different routes were used to prepare the bimetallic xPd–yNi (x = 0.06–1 wt.%, y = 0.5–1.44 wt.%, x + y = 1.5 wt.%), xRu–yNi (x = 0.06–1 wt.%, y = 0.5–1.44 wt.%, x + y = 1.5 wt.%), and xRu–yPd (x = 0.06–1 wt.%, y = 0.5–1.44 wt.%, x + y = 1.5 wt.%) catalysts by the BM method: (i) one step BM and (ii) sequential–BM. In the one step route, the bimetallic xPd–yNi, xRu–yNi, and xRu–yPd catalysts were

prepared in one step by milling together the two metal precursors with CeO_2. These catalysts are labeled as Pd–Ni/CeO_2/BM, Ru–Ni/CeO_2/BM, and Ru–Pd/CeO_2/BM.

In the sequential–BM method, firstly, one of the metal precursors was milled with CeO_2, and in a second step, the resulting material was milled with the other metal precursor. As an example, the bimetallic Pd–Ni catalysts were labeled as Pd–CeO_2/BM/Ni/BM or Ni–CeO_2/BM/Pd/BM if ceria was first milled with the Pd precursor or with the Ni precursor, respectively. Similarly, the Ru–Ni samples were labeled as Ru–CeO_2/BM/Ni/BM or Ni–CeO_2/BM/Ru/BM if CeO_2 was first milled with the Ru precursor or with the Ni precursor, respectively. Finally, the bimetallic Ru-Pd samples were labeled Ru–CeO_2/BM/Pd/BM or Pd–CeO_2/BM/Ru/BM if CeO_2 was first milled with the Ru precursor or with the Pd precursor, respectively. The effect of ball mill frequency (15, 30 and 50 Hz) and milling time (5 to 40 min) for the bimetallic Pd–Ni, and Ru–Ni catalysts were investigated. Also, for the Ru–Pd catalysts, the effect of ball mill energy (15, 30 and 50 Hz) and milling time (5, 10 and 20 min) was investigated. All fresh catalysts were tested for the POM reaction without any further treatment.

2.1.4 Monometallic Pd/CeO_2, Pd(AC)/CeO_2, Ni/CeO_2, and Ru/CeO_2 catalysts by incipient wetness impregnation

Monometallic xPd/CeO_2/IWI, xPd(AC)/CeO_2/IWI (x = 0.5 to 2 wt.%), xNi/CeO_2/IWI (x = 0.5, 1 and 1.5 wt.%), and xRu/CeO_2/IWI (x = 0.25, 0.5 and 1 wt.%) catalysts were also prepared by conventional incipient wetness impregnation for comparison (labeled as IWI). For preparation of these monometallic samples, aqueous solutions of $Pd(NO_3)_2$, $Pd(CH_3COO)_2$, $RuCl_3$, and $Ni(NO_3)_2{\cdot}6H_2O$ were used as precursors, and were added dropwise to the CeO_2 support. Samples were dried

at 90 °C and calcined at 650 °C for 4 h (5 °C min^{-1}). No further treatments were performed on the calcined samples prior to the catalytic tests.

2.1.5 Bimetallic Pd–Ni, Ru–Ni, and Pd–Ru catalysts supported on CeO_2 by incipient wetness impregnation

Bimetallic Pd–Ni, Ru–Ni, and Ru–Pd catalysts supported on CeO_2 were also prepared by conventional incipient wetness impregnation (labeled as IWI) for comparison with their analogues prepared by ball milling. Similarly to the BM method, two different routes were used to prepare the bimetallic xPd–yNi/CeO_2/IWI (x = 0.06–1 wt.%, y = 0.5–1.44 wt.%, x + y = 1.5 wt.%), xRu–yNi/CeO_2/IWI (x = 0.06–1 wt.%, y = 0.5–1.44 wt.%, x + y = 1.5 wt.%), xRu–yPd/CeO_2/IWI (x= 0.06–1 wt.%, y= 0.5–1.44 wt.%, x + y = 1.5 wt.%) catalysts by the IWI method: (i) co–IWI and (ii) sequential–IWI. In the co–IWI method, the bimetallic catalysts were prepared in one-step by impregnating an ethanol solution containing both precursors (xPd + yNi, or xRu + yNi, or xRu + yPd). Samples were dried at 90 °C and calcined at 650 °C for 4 h (5 °C min^{-1}). These samples were labeled as Pd–Ni/CeO_2/IWI, Ru–Ni/CeO_2/IWI, and Ru–Pd/CeO_2/IWI.

In the sequential–IWI method, two consecutive incipient wetness impregnations were carried out, with a calcination step at 650 °C for 2 h after each impregnation. As an example, these samples were labeled as Pd–CeO_2/IWI/Ni/IWI or Ni–CeO_2/IWI/Pd/IWI if the first impregnation was carried out with the Pd or the Ni precursor, respectively. For the other catalysts, similar labeling was used: Ru–CeO_2/IWI/Ni/IWI or Ni–CeO_2/IWI/Ru/IWI, if the first impregnation was carried out with the Ru or the Ni precursor, respectively, and Pd–CeO_2/IWI/Ru/IWI or Ru–CeO_2/IWI/Pd/IWI if the first impregnation was carried out with the Pd or the Ru

precursor, respectively. No further treatments were performed on the calcined samples before the catalytic test.

2.2 Catalytic tests

To study the catalytic performance for the POM process to syngas, a continuous–flow fixed–bed quartz reactor was used. Reactions were carried out at atmospheric pressure between 300 and 600 °C at steps of 50 °C using a CH_4: air: N_2 mixture of 4:11:85 (CH_4/O_2=1.73) and F/W=60 L h^{-1} g^{-1} (gas hourly space velocity of GHSV = 12×10^3 h^{-1}). Typically, 0.1 g of the catalyst was mixed with SiC to obtain a fixed bed volume of 0.5 cm^3, and placed in the center of the heated zone of the furnace controlled with a proportional–integral–derivative (PID) temperature controller. The reaction products were analyzed online every 4 minutes with a Varian CP–4900 gas chromatograph (GC) equipped with a Molecular Sieve of 5 Å, Plot U, and Stabilwax columns. The methane conversion (X_{CH_4}) (Eq–2.1), selectivity of hydrogen (S_{H_2}) (Eq–2.2), selectivity of carbon monoxide (S_{CO}) (Eq–2.3), selectivity of carbon dioxide (S_{CO_2}) (Eq–2.4), and yield of syngas (Y_{sg}) (Eq–2.5) were calculated according to the following equations:

$$x_{CH_4}(\%) = \frac{F_{inCH_4} - F_{outCH_4}}{F_{inCH_4}} \times 100 \qquad \text{(Eq–2.1)}$$

Where F_{inCH_4} and F_{outCH_4} are the inlet and outlet molar flow of methane, respectively.

$$S_{H_2}(\%) = \frac{\dot{m}\ of\ H_2\ produced}{\dot{m}\ of\ (H_2+CO+CO_2) produced} \times 100 \qquad \text{(Eq–2.2)}$$

$$S_{CO}(\%) = \frac{\dot{m}\ of\ CO\ produced}{\dot{m}\ of\ (H_2+CO+CO_2) produced} \times 100 \qquad \text{(Eq–2.3)}$$

$$S_{CO_2}(\%) = \frac{\dot{m}\ of\ CO_2\ produced}{\dot{m}\ of\ (H_2+CO+CO_2) produced} \times 100 \qquad \text{(Eq–2.4)}$$

$$Y_{sg}(\%) = \frac{x_{CH_4} \times (S_{H_2} + S_{CO})}{100} \quad \text{(Eq–2.5)}$$

Thermodynamic equilibrium compositions were calculated using the Bioanalytical Microfluidics Program [150].

2.3 Catalysts characterization

X–ray diffraction (XRD) was performed using a Siemens D5000 diffractometer equipped with a Cu Kα radiation source (45 kV, 35 mA) in Bragg-Brentano geometry using steps of 0.02 ° at 1 s per step. The crystallite size was calculated with the Debye-Scherrer formula. Raman spectroscopy was performed using a Renishaw inViaQontor confocal Raman microscope equipped with a 532.1 ± 0.3 nm laser with a nominal 100 mW output power directed through a specially adapted Leica DM2700 M microscope (x50 magnification). Spectra were acquired in two ranges, 50–1200 cm^{-1} and 1200–2000 cm^{-1}, with an exposure time of 0.5 s, 1% of maximum laser power, and 18 repetitions. H_2–temperature programmed reduction (H_2-TPR) was carried out with a Chemstar apparatus equipped with a TCD detector. About 50 mg of sample was exposed to 50 mL min^{-1} of H_2 diluted in Ar (5 % H_2) from room temperature up to 850 °C (10 °C min^{-1}). The surface of the catalysts was analyzed by X–ray Photoelectron Spectroscopy (XPS) using a SPECS system equipped with an XR50 source operating at 250 W and a Phoibos 150 MCD–9 detector. The pass energy of the high–resolution spectra was set at 0.1 eV. Binding energy (BE) values were referred to the Ce^{4+} $3d_{5/2}$ peak at 916.9 eV. CasaXPS program (Casa Software Ltd., UK [151]) was used to evaluate the XPS data (Shirley type background). The microstructure of the catalysts was investigated by high–resolution transmission

electron microscopy (HRTEM) using a FEI TECNAI F20 instrument equipped with a field–emission electron source operated at 200 kV.

2.4 References

1. Engineering, D.o.C.a.B. Bioanalytical Microfluidics Program. 2019; Available from: http://cbe.colostate.edu/.
2. Casa Software Ltd. 2022; Available from: http://www.casaxps.com/.

CHAPTER 3

3. Low-temperature methane partial oxidation over Pd supported on CeO_2: Effect of the preparation method and precursors

This chapter has been partially published in:

I. S. Fazlikeshteli, J. Llorca, X. Vendrell. Reactions **2**(1): 30-42.

https://doi.org/10.3390/reactions2010004

Abstract

In this chapter, the partial oxidation of methane (POM) into syngas at low temperatures (200–550 °C) over Pd (0.5–2 Pd wt.%) supported on cerium dioxide was investigated. Palladium was chosen as it is one of the most effective noble metal catalysts for methane activation, particularly when supported on materials with redox properties. The metal-support interaction between Pd and CeO_2 has demonstrated excellent properties for activating C–H bonds in the methane molecule due to the oxygen storage-release capabilities of ceria and the stabilization of oxidized Pd species [152]. In recent years, different architectures of the Pd/CeO_2 interface have been achieved using conventional impregnation, solution combustion synthesis, or mechanochemical methods, which strongly determine the performance of the resulting Pd/CeO_2 catalysts in the total oxidation of methane [74, 153-155]. The preparation of the Pd/CeO_2 catalysts is described in Chapter 2, starting with the characterization of the samples using high–resolution transmission electron microscopy (HRTEM), Raman spectroscopy, X–ray diffraction (XRD), and X–ray photoelectron spectroscopy (XPS). In the next section, the influence of the preparation method, milling energy and time for the samples made by the mechanochemical method, and metal ratio are assessed. Finally, the results of a long stability test conducted on the best monometallic Pd/CeO_2 catalysts are presented.

3.1 Characterization of fresh catalysts

3.1.1 High–resolution transmission electron microscopy (HRTEM)

The microstructure of the catalysts was investigated by high–resolution transmission electron microscopy (HRTEM) and energy-dispersive X–ray analysis (EDX). Fig–3.1a illustrates a representative image of the xPd(AC)/CeO_2 sample prepared by BM (50 Hz, 10 min, x = 1 wt.% Pd(AC)). As reported by Danielis et al. [156], the mechanochemical synthesis of 1Pd(AC)/CeO_2/BM creates an amorphous layer on the CeO_2 crystallites. This amorphous layer exhibits an average thickness of about 2–3 nm. The EDX analysis of the amorphous layer (inset in Fig–3.1a) indicates the simultaneous occurrence of Ce, Pd and O (the Cu signal originates from the TEM grid), which shows these layers are constituted by a Pd–O–Ce phase. Fig–3.1b corresponds to the xPd/CeO_2/BM sample (also 50 Hz, 10 min, x = 1 wt.% Pd). On the other side, the substitution of Pd acetate by Pd nitrate in the mechanochemical preparation method originates a very different microstructure. The 1Pd/CeO_2/BM sample contains subnanometric Pd entities instead of an amorphous Pd–O–Ce shell, which are well dispersed on the ceria support. Some of these subnanometric Pd entities are shown in a green circle in Fig–3.1b.

The microstructure of the 1Pd(AC)/CeO_2/IWI sample is shown in Fig–3.1c. In contrast with the catalysts prepared by BM, the sample prepared by IWI using Pd acetate shows the occurrence of well-defined Pd nanoparticles, which measure about 3–4 nm. Finally, Fig–3.1d corresponds to the 1Pd/CeO_2/IWI sample. Individual Pd

nanoparticles are also encountered, but the use of $Pd(NO_3)_2$ as precursor results in smaller Pd nanoparticles, which measure about 1–2 nm.

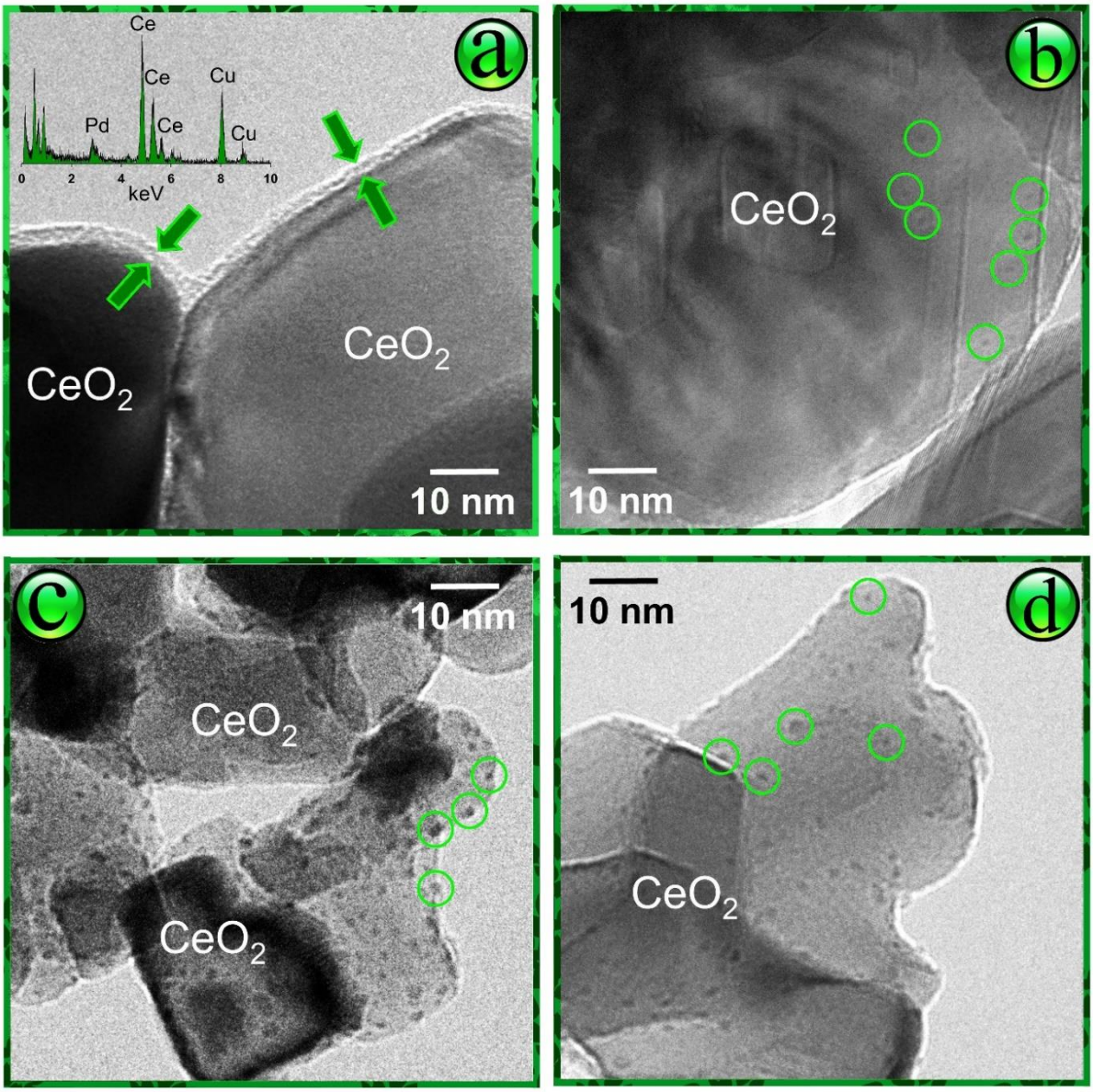

Fig-3. 1: HRTEM images of the catalysts: $Pd(AC)/CeO_2/BM$ (a), $Pd/CeO_2/BM$ (b), $Pd(AC)/CeO_2/IWI$ (c), and $Pd/CeO_2/IWI$ (d). All catalysts contain a nominal Pd loading of 1 wt.%. Ball mill conditions: 50 Hz for 10 min.

3.1.2 X–ray diffraction (XRD) patterns and Raman spectroscopy

The X–ray diffraction (XRD) patterns and Raman spectra recorded for the samples investigated by TEM are shown in Fig–3. 2a and 2b, respectively. For all catalysts, the only peaks detected by XRD were those corresponding to the CeO_2 support. Due to the low Pd loading (1 wt.%), no peaks associated with Pd phases and no variation of the lattice parameter of CeO_2 were detected, excluding the possibility of Pd incorporation in the ceria structure. As a result, for samples prepared by BM, the size of the ceria crystallites decreased from about 35 nm down to 31.6 nm after milling for 5 min at 50 Hz and 26.7 nm after ball milling for 10 min at 50 Hz.

For all samples, the Raman spectra (Fig–3.2b) were dominated by the characteristic F_{2g} band of the ceria lattice structure at ~ 463 cm^{-1} [157]. The defect-induced vibrational mode at ~ 595 cm^{-1} (D band) was nearly absent in all samples, which means the incorporation of Pd did not result in the formation of lattice defects in the CeO_2 structure, such as oxygen vacancies [158]. It is worth noting that the main F_{2g} peak of ceria for the samples prepared by BM method shifted slightly to lower wavelengths (~ 460 cm^{-1}), caused by an enhanced Pd–support interaction in the samples prepared by BM [159], whereas it appeared at the same wavelength for the samples prepared by IWI method. Moreover, the Raman spectrum of the $Pd(AC)/CeO_2/BM$ sample showed a weak band at 945 cm^{-1}, which is ascribed to the ($C–CH_3$) mode of the acetate group. For the $Pd/CeO_2/BM$ sample, the Raman spectrum showed a weak band at 1046 cm^{-1}, which is ascribed to the symmetric ν_1 stretching mode of the nitrate anion [160]. These bands were absent in the catalysts prepared by IWI method, because the acetate and nitrate residues disappeared following the calcination treatment performed at 650 °C. Finally, the Raman spectrum

of the $Pd/CeO_2/IWI$ catalyst exhibited a band at 650 cm^{-1}, which is attributed to the B_{1g} mode of PdO and suggests that this sample contains well-defined PdO nanoparticles [161].

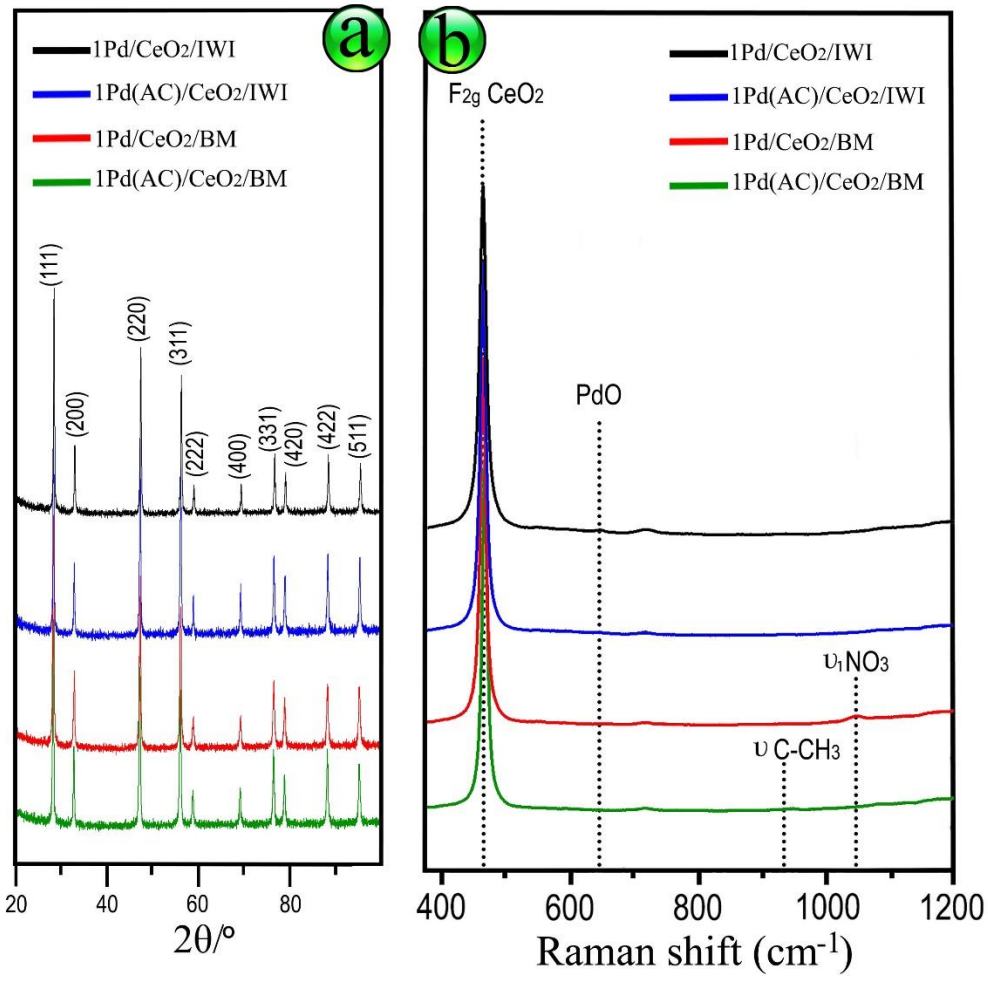

Fig-3. 2: XRD (a) profiles and Raman spectra (b) of the catalysts: $Pd/CeO_2/IWI$, $Pd(AC)/CeO_2/IWI$, $Pd/CeO_2/BM$, and $Pd(AC)/CeO_2/BM$. All catalysts contain a nominal Pd loading of 1 wt. %. Ball mill conditions: 50 Hz for 10 min.

3.1.3 X–ray Photoelectron Spectroscopy (XPS)

The surface composition of the catalysts was analyzed by X–ray photoelectron spectroscopy (XPS). Fig–3.3 shows the Pd 3d XP spectra of the catalysts investigated

by HRTEM, XRD and Raman spectroscopy discussed above. There are important differences among the XP spectra between the samples prepared by the BM method and those prepared by the IWI method. The Pd 3d spectra of the samples prepared by IWI showed the same pattern, independently of the Pd precursor used (Fig–3. 3a and 3b). The Pd $3d_{5/2}$ spectra contain two bands at about 336.4 and 338.0 eV, which can be ascribed well to Pd^{2+} and Pd^{4+} species, respectively [153, 156]. Moreover, the surface atomic ratio ($\frac{Pd^{4+}}{Pd^{4+}+Pd^{2+}}$) for the samples prepared by IWI method is about 0.2. In contrast, the spectra of the samples prepared by BM are quite different. The Pd/CeO_2/BM sample (Fig–3.3c) exhibited a unique band at 337.7 eV, whereas the spectrum of the Pd(AC)/CeO_2/BM sample (Fig–3.3d) indicated two bands at 336.0 and 337.6 eV, which represent a shift of 0.4 eV to lower energy values with respect to the catalysts prepared by IWI method.

These results demonstrate that the electronic state of Pd at the surface of the catalysts strongly depends on the preparation method. Additionally, for samples prepared by BM, the shift to lower binding energy values is indicative of surface oxidized Pd strongly interacting with CeO_2 [162-164], which is in agreement with HRTEM and Raman spectroscopy data. In addition, the surface atomic ratio ($\frac{Pd^{4+}}{Pd^{4+}+Pd^{2+}}$) of the samples prepared by BM are much higher and the values depend on the Pd precursor used; for the Pd(AC)/CeO_2/BM sample this value is 0.6, which is much higher than the value recorded in the catalyst prepared by IWI with Pd acetate (= 0.2). It is concluded that Pd^{4+} species strongly interacting with CeO_2 are easily accommodated on the surface of catalysts prepared by BM method.

In addition, XPS yields valuable information about the dispersion of Pd. The surface atomic ratio ($\frac{Pd}{Pd+Ce}$) is higher in the Pd(AC)/CeO_2/BM sample (= 0.29) with respect to the Pd/CeO_2/BM sample (= 0.14) and also for the samples prepared by IWI (= 0.2). The high Pd dispersion measured by XPS for the Pd(AC)/CeO_2/BM sample is in accordance with the existence of the amorphous shell identified by HRTEM (Fig–3.1d).

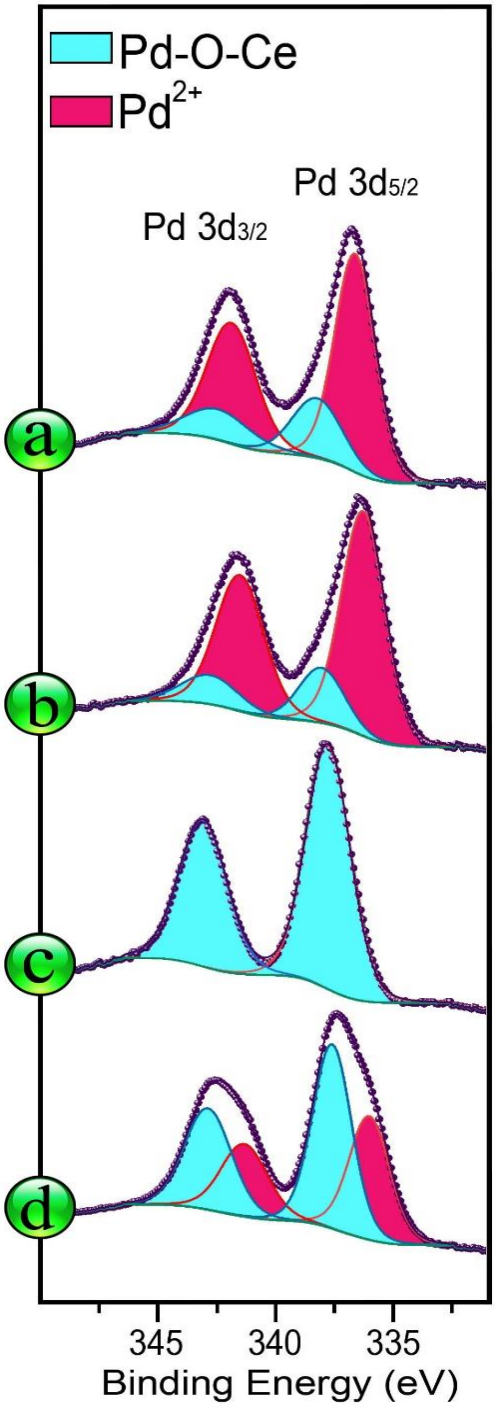

Fig-3. 3: Pd 3d X–ray photoelectron spectra of the catalysts: Pd/CeO_2/IWI (a), Pd(AC)/CeO_2/IWI (b), Pd/CeO_2/BM (c) and Pd(AC)/CeO_2/BM (d). All catalysts contain a nominal Pd loading of 1 wt.%. Ball mill conditions: 50 Hz for 10 min.

3.2 Catalytic tests

The temperature-dependent catalytic performance of the different catalysts prepared followed similar patterns. As a representative example, Fig–3.4a shows these profiles recorded over the 0.5Pd(AC)/CeO_2 sample prepared by BM method at

50 Hz for 5 min. As expected, the conversion of methane progressively increased with temperature, whereas oxygen was rapidly consumed at low temperatures (≤ 350 °C). The oxygen consumption was accompanied by the simultaneous appearance of water and carbon dioxide in a H_2O:CO_2 ratio of about 2:1 (molar basis). Moreover, in the range 300–350 °C, the consumption of O_2 is double than that of CH_4, and the amount of CO_2 formed equaled the amount of CH_4 consumed. Overall, this distribution of species clearly shows that the direct combustion of methane takes place in this temperature range (300–350 °C), $CH_4 + 2O_2 \rightarrow CO_2 + 2H_2O$. When all the oxygen was consumed, at 400 °C, the consumption of CH_4 was accompanied by the simultaneous consumption of H_2O, being the amount of water consumed double than that of methane, and at the same time, CO_2 and H_2 were produced. The amount of CO_2 produced equaled the amount of CH_4 consumed, and the amount of H_2 produced was about four times that of CH_4 consumed. This distribution of species corresponds well to the methane steam reforming (SRM, Eq–1.6: $CH_4 + H_2O \rightleftarrows CO + 3H_2$) reaction. At temperatures higher than 450 °C, the transformation of methane was accompanied by the progressive consumption of not only H_2O, but also CO_2. At the same time, the production of syngas (H_2 and CO) increased, which was produced by the simultaneous occurrence of the SRM and dry reforming of methane (DRM, Eq–1.7: $CH_4 + CO_2 \rightleftarrows 2CO + 2H_2$) reactions, respectively. These reaction mechanism corresponds well with the so-called “combustion and reforming reaction (CRR)” mechanism for POM process [92, 165].

For comparison, Fig–3.4b indicates the distribution of products obtained at different temperatures with the 0.5Pd(AC)/CeO_2 catalyst prepared by IWI method. Similar trends were observed in the disappearance of reactants and the appearance of products, which shows that the reaction mechanism is the same as that discussed above, but the temperatures for the catalyst prepared by IWI method shifted to higher values, about 100 °C, indicating lower catalytic activity.

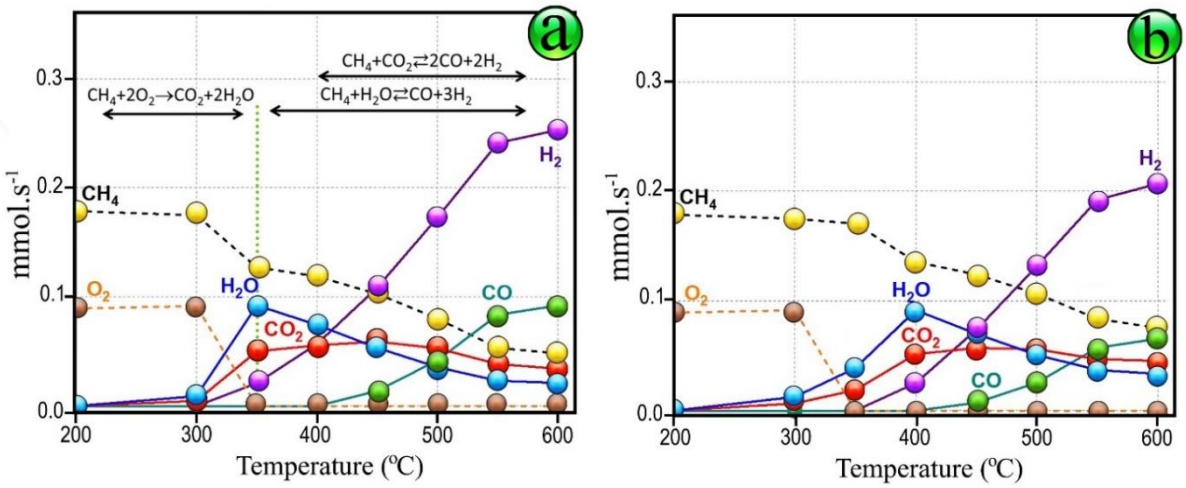

Fig-3. 4: Molar flows of the different species present during the partial oxidation of methane on 0.5Pd(AC)/CeO_2 prepared by dry BM at 50 Hz for 5 min (a) and 0.5Pd(AC)/CeO_2 prepared by IWI (b). GHSV=12 × 10^3 h^{-1}, F/W=60 L h^{-1} g^{-1}.

Considering the two consecutive steps involved in the POM mechanism on Pd/CeO_2 and Pd(AC)/CeO_2 catalysts, since at temperature lower than 450 °C the production of syngas is not significant, from now on, only the results obtained at temperatures above 450 °C will be considered. Table–3.1, and Table–3.2 are include the results obtained for all catalysts tested in terms of methane conversion and hydrogen selectivity at 450 and 550 °C, and selectivity of CO at 550 °C for the sample prepared by IWI and BM methods, respectively. The results obtained on bare CeO_2 as prepared and after milling at 50 Hz for 10 min are also included as blank runs

(Table–3.1). The CeO_2 support is totally inactive for POM process under the reaction conditions tested, and also CeO_2/BM did not result in any reactivity in the absence of Pd.

Table–3.1. Methane conversion and selectivity of hydrogen and carbon monoxide obtained at 450 and 550 °C on Pd/CeO_2 catalysts prepared by IWI method using different synthesis parameters and metal loading values.

Catalyst	Hz	min	wt.% Pd	$X_{CH_4}^{450\,°C}$	$X_{CH_4}^{550\,°C}$	$S_{H_2}^{450\,°C}$	$S_{H_2}^{550\,°C}$	$S_{CO}^{550\,°C}$
Equilibrium	–	–	–	51.3	77.9	60.4	64.6	26.3
CeO_2	–	–	–	0	0	0	0	0
CeO_2/BM	50	10	–	0	0	0	0	0
Pd(AC)/CeO_2/IWI	–	–	0.5	32.8	50.7	46	62.4	16.6
Pd(AC)/CeO_2/IWI	–	–	1	35.9	59.2	51.5	64.5	19.8
Pd(AC)/CeO_2/IWI	–	–	2	37.0	62.3	54.1	65.2	20.6
Pd(AC)/CeO_2/IWI	50	5[a]	1	34.2	57.0	52.4	64.5	19.6
Pd/CeO_2/IWI	–	–	0.5	39.7	67.7	59	66.2	23
Pd/CeO_2/IWI	–	–	1	34.5	57.4	52.4	64.5	19.4
Pd/CeO_2/IWI	–	–	2	32.8	56.0	53.1	65	20.3
Pd/CeO_2/IWI	50	10[b]	1	34.8	59.2	54.3	65	20.4

[a]impregnation on previously ball milled CeO_2

Table–3.2. Methane conversion and selectivity of hydrogen and carbon monoxide obtained at 450 and 550 °C on bare ceria, ceria after ball milling, and Pd/CeO_2 catalysts prepared by BM using different synthesis parameters and metal loading values.

Catalyst	Hz	min	wt.% Pd	$X_{CH_4}^{450\,°C}$	$X_{CH_4}^{550\,°C}$	$S_{H_2}^{450\,°C}$	$S_{H_2}^{550\,°C}$	$S_{CO}^{550\,°C}$
Pd(AC)/CeO_2/BM	15	10	1	34.9	47.0	52.1	63.1	16.7
Pd(AC)/CeO_2/BM	30	10	1	35.5	55.9	52	64	18.8
Pd(AC)/CeO_2/BM	50	5	1	42.5	70.2	59.8	66.4	23
Pd(AC)/CeO_2/BM	50	10	1	38.9	64.1	56.8	65.3	21
Pd(AC)/CeO_2/BM	50	10	1[b]	33.5	55.8	51.7	64.3	19.4
Pd(AC)/CeO_2/BM	50	20	1	36.8	58.5	53.9	64.6	19.4
Pd(AC)/CeO_2/BM	50	5	0.5	48.1	73.1	63.3	66.7	24.9
Pd(AC)/CeO_2/BM	50	5	2	39.7	67.5	59	66.2	22.9
Pd/CeO_2/BM	15	10	1	35.2	54.9	49.7	63.5	18
Pd/CeO_2/BM	30	10	1	31.5	51.0	52.2	64	18.2
Pd/CeO_2/BM	50	5	1	30.7	47.0	50.8	63.1	16.7
Pd/CeO_2/BM	50	10	1	30.5	53.2	53.4	64.9	19.3
Pd/CeO_2/BM	50	10	1[a]	45.4	70.2	62.6	66.5	24.4
Pd/CeO_2/BM	50	20	1	32.7	55.7	54.9	65.2	20.2
Pd/CeO_2/BM	50	10	0.5	32.6	52.7	48.4	63.3	17.4
Pd/CeO_2/BM	50	10	2	39.9	66.8	56.9	64.9	22

[b]calcined at 300 °C for 1 h.

The catalytic performances for the catalysts prepared by BM demonstrate that the Pd salt used as precursor has a strong effect on catalytic activity. Fig–3.5 displays the data selected from Table–3.1 & Table–3.2 to perform accurate comparisons between different catalysts. In Fig–3.5a, the influence of ball milling time for the catalysts

containing 1 wt.% Pd and prepared at 50 Hz with Pd nitrate or Pd acetate precursors is shown. Clearly, at short milling times (5 and 10 min) the activity of 1Pd(Ac)/CeO_2/BM (50 Hz) catalysts outperforms those of samples prepared with Pd nitrate, whereas after long milling time (20 min) the methane conversion on both samples became similar. Interestingly, the longer the milling time, the higher the activity for the 1Pd/CeO_2/BM(50 Hz) catalysts. This suggests that a particular and delicate Pd–CeO_2 architecture is formed at a short milling time using Pd acetate, which is highly active for POM process. Contrarily, the resulting metal–support interaction is independent of the Pd salt used as a precursor if a long milling time is used. This could be attributed to the peculiar decomposition of Pd acetate, which first decomposes to metallic Pd and then gradually oxidizes to PdO in contrast to Pd nitrate, which decomposes directly to PdO [166].

Recently, it has been claimed that for Pd/CeO_2 systems, a metal-core-oxide-shell structure is responsible for a high activity for the combustion of methane [167]. The different decomposition pathways of Pd acetate and Pd nitrate would likely result in different Pd–ceria interactions developed during the POM reaction.

These results are also supported by Fig–3.5b, where the effect of the frequency of ball milling (energy) is shown for the samples containing 1 wt.% Pd after 10 min. It is deduced high milling energy has a beneficial effect on catalytic activity of the 1Pd(AC)/CeO_2/BM (10 min) samples, which suggests that a strong Pd–CeO_2 interaction favors the activation of the methane molecule, whereas an opposite trend is observed in the 1Pd/CeO_2/BM (10 min) samples. On the other hand, two ball-milled samples (50 Hz and 10 min) prepared with Pd acetate and Pd nitrate and calcined at 300 °C to remove the acetate and nitrate groups, respectively, showed different results

(Table–**3**.2). Whereas the catalytic activity of the sample prepared by BM using Pd acetate decreased slightly after calcination, the sample prepared by BM using Pd nitrate showed a clear improvement after the calcination treatment, which suggests that the presence of nitrate residues on the catalyst surface is detrimental for the reaction.

Recent density functional theory (DFT) calculations have shown that $Pd_xCe_{1-x}O_\delta$ surfaces are particularly effective in the activation of the C-H bonds in the methane molecule [166, 168], and that substitution of Ce by Pd ions originates highly active and stable systems [169, 170]. The mechanochemical forces that operate in the ball milling preparation method would enhance the formation of such active surfaces and substituted structures, as demonstrated recently in the total oxidation of methane [153]. In fact, the amorphous shell observed in the HRTEM images of the 1Pd(AC)/CeO_2/BM catalyst (Fig-3.2) is expected to be particularly active due to under-coordinated sites, as claimed recently by DFT calculations for the activation of methane [171].

Important information is obtained from Fig-3.5c, where the methane conversion is plotted against the Pd loading for samples prepared by BM at 50 Hz for 5 min. For the catalysts using the Pd nitrate, with increasing the Pd content the methane conversion increased. In contrast, the opposite trend was observed for the catalysts using Pd acetate, which is in accordance with the assumption that low Pd contents are required to build up active $Pd_xCe_{1-x}O_\delta$ surfaces, whereas high Pd loadings result in the accumulation of other less active Pd species on the surface.

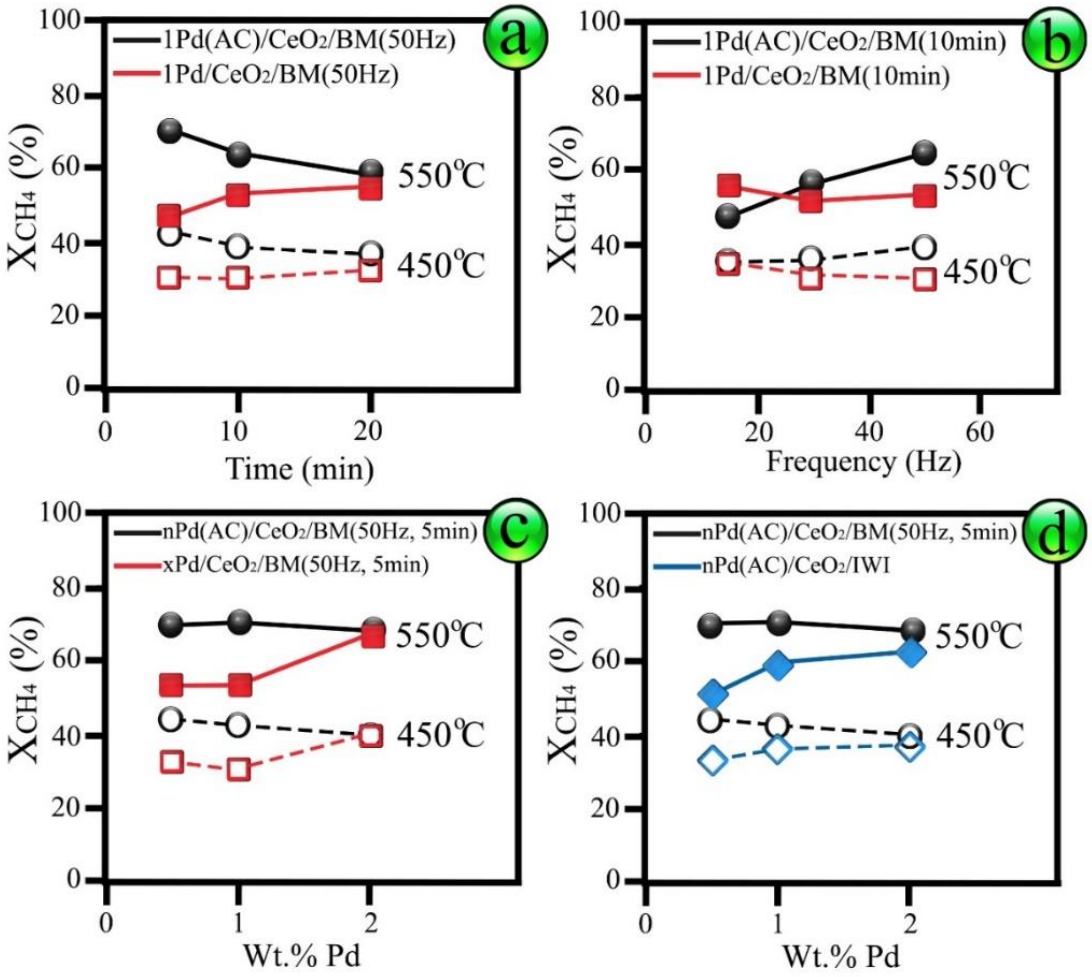

Fig-3. 5: Conversion of methane at 450 and 550°C on Pd catalysts prepared by milling CeO_2 and palladium acetate (black) or palladium nitrate (red) at different milling time (a), frequency (b) and Pd loading (c). Conversion of methane on Pd(AC)/CeO_2 prepared by BM (black) and IWI (blue) (d). GHSV=12 × 10^3 h^{-1}, F/W=60 L h^{-1} g^{-1}.

Fig–3.5d clearly illustrates that the catalytic performances of the Pd(AC)/CeO_2 catalysts prepared by the IWI method are less active than the Pd(AC)/CeO_2 catalysts prepared by BM for any Pd loading. Indeed, the performances of the Pd/CeO_2 catalysts prepared by ball milling using Pd nitrate are similar to those prepared by IWI method, again pointing out to an extraordinary catalytic behavior induced by the amorphous $Pd_xCe_{1-x}O_\delta$ surface in the catalysts prepared by BM using Pd acetate.

Finally, to investigate if the better catalytic performance of the samples prepared by BM are due to defects and/or structural changes of the CeO_2 support induced by the BM method. We also tested the catalysts prepared by the IWI method using milled CeO_2 with the exact same conditions. The catalytic performance of the IWI samples using fresh CeO_2 and CeO_2/BM are virtually identical (Table–3.1), which means that the catalytic behavior of the Pd/CeO_2 samples prepared by BM is not related to the CeO_2 support, but to a specific interaction between CeO_2 and Pd induced by the mechanochemical method.

3.3 Stability tests

In order to investigate the catalysts stability, the 0.5Pd(AC)/CeO_2/BM catalyst, which exhibited good methane conversion and selectivity to syngas (see Table–3.2), was tested at 550 °C for more than 100 h on POM process (Fi–3.6a). For comparative purpose, the 0.5Pd(AC)/CeO_2/IWI sample was also examined. During the first 50 h of stream, a slight deactivation of the sample prepared by BM method was observed, where the CH_4 conversion rate decreased by approximately 0.15 % h^{-1}.

After 50 h, the deactivation decreased by only 0.04 % h^{-1}, the CH_4 conversion stabilized at about 63 % and the selectivity to H_2 and CO were ~ 64.9 and 17.9 %, respectively. In contrast, for the sample prepared by IWI deactivated more severely; during the first 50 h of operation the methane conversion rate decreased significantly by 0.48 % h^{-1} and in the second 50 h the methane conversion rate still decreased by 0.23 % h^{-1} and did not stabilize.

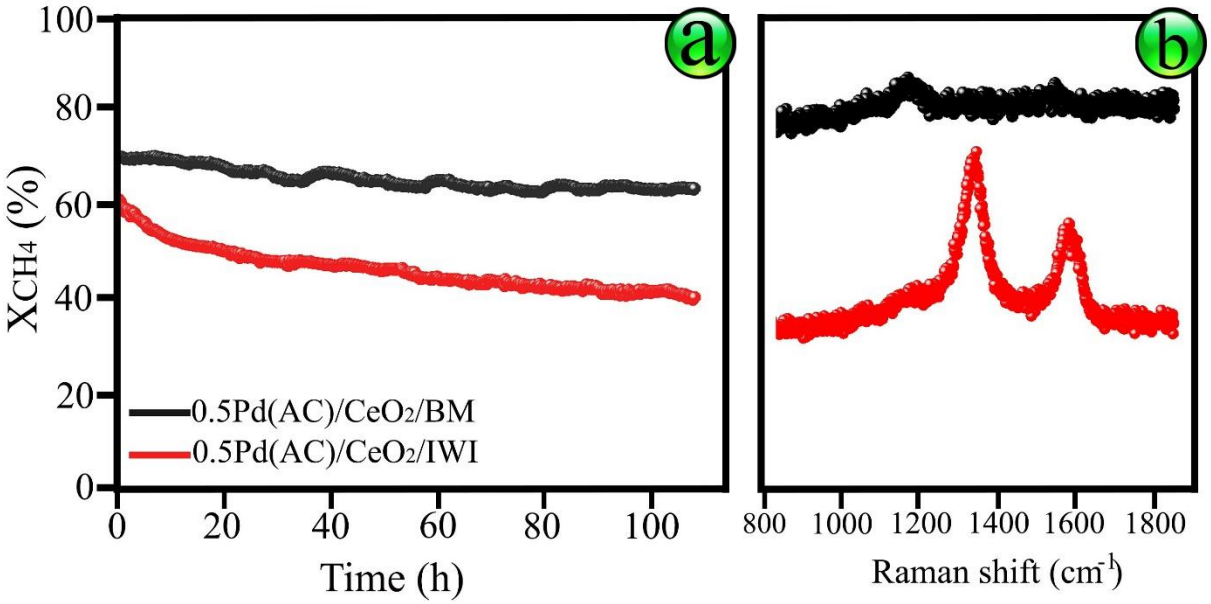

Fig-3. 6: Methane conversion in a long-term stability at 550 °C on 0.5Pd(AC)/CeO_2 prepared by BM(50Hz, 5min) and by IWI methods. GHSV=12 × 10^3 h^{-1}, F/W=60 L h^{-1} g^{-1}. (b) Raman spectra recorded on the samples after reaction.

We recorded the Raman spectra in the carbon region for the two samples after reaction (Fig–3.6b), since the DRM is involved in the reaction mechanism and generally causes carbon deposition on the catalyst. The Raman spectrum for the 0.5Pd(AC)/CeO_2/BM sample after reaction showed a broad signal at approximately 1180 cm^{-1}, which corresponds to the second-order longitudinal optical mode (2LO) of CeO_2 [39]. In contrast, the Raman spectrum of the 0.5Pd(AC)/CeO_2/IWI sample after the reaction showed, in addition to the signal at ca. 1180 cm^{-1} due to CeO_2, the characteristic D and G bands of carbon at approximately 1340 and 1580 cm^{-1}, respectively. Even if the intensity of the carbon bands is certainly low, the occurrence of carbon deposition may explain the deactivation observed for this sample. Therefore, the catalyst prepared my BM is not only more active, but remarkably more stable under reaction conditions. This result makes this catalyst a good candidate for practical application. In addition, it contains a low metal loading.

3.4 Conclusion

A series of Pd/CeO_2 and $Pd(AC)/CeO_2$ catalysts have been prepared, characterized with HRTEM, XRD, Raman spectroscopy and XPS, and tested for the partial oxidation of methane at low temperature to obtain syngas. Two different preparation methods have been used to synthesize the catalysts, conventional incipient wetness impregnation and dry ball mill. Two metal precursors have been used, palladium nitrate and palladium acetate, and the metal loading has been varied from 0.5 to 2 wt.% Pd. For the ball-milled samples, the influence of milling energy (15–50 Hz) and milling time (5–20 min) on the catalytic performance has been evaluated. Catalysts prepared by mechanochemistry using Pd acetate have shown better catalytic performance than catalysts prepared by mechanochemistry using Pd nitrate and catalysts prepared by incipient wetness impregnation, either with Pd acetate or with Pd nitrate. The best catalytic performance has been obtained with a catalyst prepared by milling ceria and Pd acetate for 5 min at 50 Hz with a metal loading of 0.5 % by weight of palladium, which has also shown good catalytic stability in a 100 h experiment duration. Catalysts prepared by incipient wetness impregnation contain well-defined PdO nanoparticles. In contrast, catalysts prepared by milling ceria and Pd acetate contain a unique Pd/CeO_2 architecture characterized by a 2–3 nm thick amorphous layer with highly oxidized Pd (Pd^{4+}–like) on the surface that strongly interacts with ceria, which is very active for methane partial oxidation.

3.5 References

1. Toso, A., et al., The dynamics of PdO-Pd phase transformation in the presence of water over Si-doped Pd/CeO_2 methane oxidation catalysts. Applied Catalysis A: General, 2019. **574**: p. 79-86.
2. Colussi, S., et al., Nanofaceted Pd–O Sites in Pd–Ce Surface Superstructures: Enhanced Activity in Catalytic Combustion of Methane. Angewandte Chemie International Edition, 2009. **48**(45): p. 8481-8484.
3. Danielis, M., et al., Outstanding Methane Oxidation Performance of Palladium-Embedded Ceria Catalysts Prepared by a One-Step Dry Ball-Milling Method. Angewandte Chemie, 2018. **130**(32): p. 10369-10373.
4. Danielis, M., et al., The effect of milling parameters on the mechanochemical synthesis of Pd–CeO_2 methane oxidation catalysts. Catalysis Science & Technology, 2019. **9**(16): p. 4232-4238.
5. Adijanto, L., et al., Exceptional thermal stability of Pd@ CeO_2 core–shell catalyst nanostructures grafted onto an oxide surface. Nano letters, 2013. **13**(5): p. 2252-2257.
6. Danielis, M., et al., Methane oxidation activity and nanoscale characterization of Pd/CeO_2 catalysts prepared by dry milling Pd acetate and ceria. Applied Catalysis B: Environmental, 2022. **282**: p. 119567.
7. Wu, Z., et al., Probing defect sites on CeO_2 nanocrystals with well-defined surface planes by Raman spectroscopy and O_2 adsorption. Langmuir, 2010. **26**(21): p. 16595-16606.

8. Weber, W., K. Hass, and J. McBride, Raman study of CeO_2: second-order scattering, lattice dynamics, and particle-size effects. Physical Review B, 1993. **48**(1): p. 178.
9. Kosacki, I., et al., Raman scattering and lattice defects in nanocrystalline CeO_2 thin films. Solid State Ionics, 2002. **149**(1-2): p. 99-105.
10. Waterland, M.R., D. Stockwell, and A.M. Kelley, Symmetry breaking effects in NO_3^-: Raman spectra of nitrate salts and ab initio resonance Raman spectra of nitrate–water complexes. The Journal of Chemical Physics, 2001. **114**(14): p. 6249-6258.
11. Ma, J., et al., The relationship between the chemical state of Pd species and the catalytic activity for methane combustion on Pd/CeO_2. Catalysis Science & Technology, 2018. **8**(10): p. 2567-2577.
12. Slavinskaya, E., et al., Metal–support interaction in Pd/CeO_2 model catalysts for CO oxidation: from pulsed laser-ablated nanoparticles to highly active state of the catalyst. Catalysis Science & Technology, 2016. **6**(17): p. 6650-6666.
13. Divins, N.J., et al., Influence of the support on surface rearrangements of bimetallic nanoparticles in real catalysts. Science, 2014. **346**(6209): p. 620-623.
14. Garcia, X., et al., Ceria-Based Catalysts Studied by Near Ambient Pressure X–ray Photoelectron Spectroscopy: A Review. Catalysts, 2020. **10**(3): p. 286.
15. Enger, B.C., R. Lødeng, and A. Holmen, A review of catalytic partial oxidation of methane to synthesis gas with emphasis on reaction mechanisms over transition metal catalysts. Applied Catalysis A: General, 2008. **346**(1-2): p. 1-27.
16. York, A.P., T. Xiao, and M.L. Green, Brief overview of the partial oxidation of methane to synthesis gas. Topics in Catalysis, 2003. **22**(3-4): p. 345-358.

17. Senftle, T.P., A.C. Van Duin, and M.J. Janik, Methane activation at the Pd/CeO_2 interface. ACS Catalysis, 2017. **7**(1): p. 327-332.
18. Murata, K., et al., Exploiting Metal–Support Interactions to Tune the Redox Properties of Supported Pd Catalysts for Methane Combustion. ACS Catalysis, 2019. **10**(2): p. 1381-1387.
19. Senftle, T.P., A.C. Van Duin, and M.J. Janik, Role of Site Stability in Methane Activation on Pd x Ce1–x Oδ Surfaces. ACS Catalysis, 2015. **5**(10): p. 6187-6199.
20. Su, Y.-Q., et al., Stable Pd-doped ceria structures for CH_4 activation and CO oxidation. ACS catalysis, 2018. **8**(1): p. 75-80.
21. Su, Y.-Q., et al., Highly active and stable CH_4 oxidation by substitution of Ce^{4+} by two Pd^{2+} ions in CeO_2 (111). ACS catalysis, 2018. **8**(7): p. 6552-6559.
22. Bunting, R.J., et al., Amorphous Surface PdO X and Its Activity toward Methane Combustion. ACS Catalysis, 2019. **9**(11): p. 10317-10323.

CHAPTER 4

4. Low-temperature partial oxidation of methane over Pd–Ni bimetallic catalysts supported on CeO_2

The data used in this chapter has been partially published in:

I. S. Fazlikeshteli, J. Llorca, X. Vendrell. International Journal of Hydrogen Energy 48(32): 12024-12035.

https://doi.org/10.1016/j.ijhydene.2022.07.020

Abstract

Nickel-based catalysts have been widely investigated due to their low cost; nevertheless, at temperatures higher than 700 ˚C, they are easily deactivated owing to carbon deposition and metal loss [89, 95, 172]. To improve thermal stability and activity and decrease carbon deposition, other components like noble metals (Pd, Pt, Rh, Ru, etc.) are added to Ni catalysts. Therefore, in the present chapter the bimetallic xPd–yNi/CeO_2 catalysts, have been investigated to promote methane conversion for partial oxidation of methane (POM) process into syngas at low temperatures (300–550 °C). For comparative purposes, monometallic xPd/CeO_2 and yNi/CeO_2 catalyst were also prepared and tested. The preparation of the monometallic xPd/CeO_2, yNi/CeO_2 and bimetallic xPd–yNi/CeO_2 catalysts have been described in Chapter 2. At first, the characterization such as Raman spectroscopy, High–resolution transmission electron microscopy (HRTEM), Temperature programmed reduction (H_2–TPR), and X–ray photoelectron spectroscopy (XPS) for the fresh samples have been evaluated. After that, the influence of the preparation method, the sequence in which the metals are added, the milling energy and time for samples prepared by the mechanochemical method, and the Pd:Ni metal ratio, have been explained in the catalytic test section. At the end, we discussed about the characterization of the catalysts after reaction and the long stability test result that obtained by the best bimetallic Pd–Ni/CeO_2 catalysts.

4.1 Characterization of fresh catalysts

4.1.1 Raman spectroscopy

The Raman spectra recorded for the fresh bimetallic Pd–Ni catalysts supported on CeO_2 prepared by BM and IWI methods are shown in Fig–4.1. For each sample, various spectra were recorded at several places and no differences were noted, indicating homogeneity of the samples. In all cases, the Raman spectra was dominated by the characteristic F_{2g} mode of the ceria lattice structure at about at ~ 464 cm^{-1} [157]. Moreover, Raman spectra for the bimetallic Pd–Ni/CeO_2 catalyst prepared by BM method showed a weak band at ~1050 cm^{-1}, which corresponds to the symmetric ν_1 stretching mode of the nitrate anion [173, 174]. It should be noted that, the NO_3^- band was absent in the bimetallic Pd–Ni/CeO_2 catalysts prepared by IWI because nitrate residues disappeared following the calcination treatment performed at 650 °C. Also, for the bimetallic Pd–Ni/CeO_2/IWI catalyst, a broad band from ~530 to 620 cm^{-1} corresponds to NiO species [174], although a defect-induced vibrational mode of ceria, such as oxygen vacancies, cannot be discarded (~595 cm^{-1}, D band) [158].

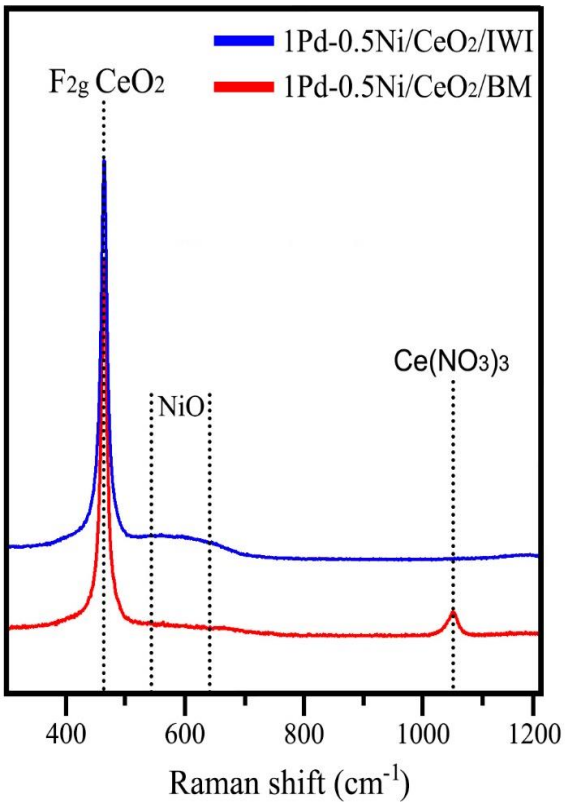

Fig-4. 1: Raman spectra of bimetallic xPd–yNi/CeO_2 catalysts (x = 1 wt.% and y = 0.5 wt.%) prepared by IWI (blue) and BM (red) at 50 Hz for 20 min (black).

4.1.2 High–resolution transmission electron microscopy (HRTEM)

High–resolution transmission electron microscopy (HRTEM) and energy-dispersive X–ray analysis (EDX) were applied to study the microstructure of the catalysts, the metal dispersion, and potential interactions between metal and support, as shown in Fig–4.2. A representative image of the monometallic 1Pd/CeO_2 catalyst prepared by BM is show in Fig–4.2a. This sample is very homogeneous and contains subnanometric Pd entities, which are well dispersed over the CeO_2 support (some of them signed with arrows in the image). A larger Pd particle is highlighted with a dashed square. Moreover, the Fourier Transform (FT) image of this area is shown in the inset and shows spots at 1.9 Å from CeO_2 (220) planes and at 2.2 Å from Pd (111) planes. The EDX spectrum recorded in the same area confirms the nature of the particle and illustrates the simultaneous occurrence of Ce, Pd and O (the Cu signal originates from the TEM grid).

Fig–4.2b corresponds to the bimetallic 1Pd–0.5Ni/CeO_2 catalysts prepared by IWI method. It is hard to distinguish any Pd, Ni or Pd–Ni particle by the TEM analysis, which means an excellent dispersion of Pd and Ni on the CeO_2 support. Additionally, the EDX spectrum recorded from the area enclosed by the square indicates only weak Pd signals; no signals of Ni are observed, probably due to the low loading of Ni (0.5 wt.%).

Finally, Fig–4.2c shows the microstructure of the bimetallic Pd–Ni/CeO_2 catalysts prepared by the BM method. The ceria crystallites are surrounded by an amorphous layer as a result of the mechanochemical preparation of Pd–Ni/CeO_2 (marked between arrows). This shell exhibits an average thickness of about 2–4 nm. The EDX spectrum recorded from the area enclosed by the square conclusively identified both

Pd and Ni in this amorphous shell. The amorphous shell is similar to that recently reported in Pd/CeO_2 catalysts prepared by BM method [153] and corresponds to an unprecedented architecture.

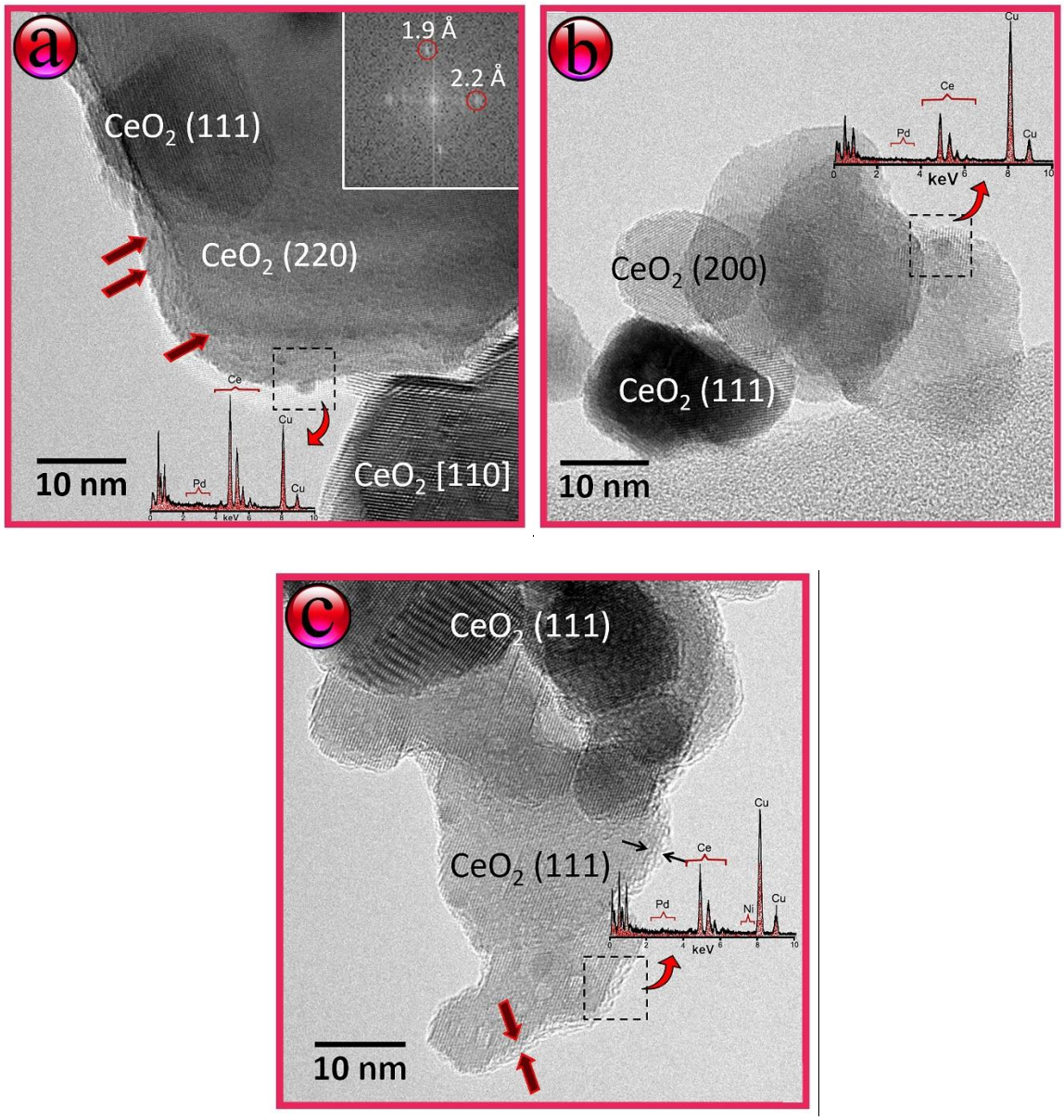

Fig-4. 2: HRTEM images of (a) monometallic 1Pd/CeO_2 catalyst prepared by BM at 50 Hz for 20 min; (b) bimetallic 1Pd–0.5Ni/CeO_2 catalyst prepared by IWI; (c) bimetallic 1Pd–0.5Ni/CeO_2 catalyst prepared by BM at 50 Hz for 20 min.

4.1.3 Temperature programmed reduction (H_2–TPR)

Fig–4.3 displays the H_2–TPR profiles obtained for the investigated samples. In all samples, a high-temperature reduction peak at 700 °C, according to previous chapter, is ascribed to the bulk reduction of CeO_2 [175]. However, it is important to note that, this high-temperature peak is shifted to lower temperatures when samples are prepared by the BM method with respect to analogous samples prepared by IWI. According to an improved metal-support interaction after calcination [176, 177], the Ni/CeO_2/IWI catalyst appears a broad H_2 consumption at about 450 °C, which can be assigned to the reduction of NiO strongly interacting with the CeO_2 support [178, 179]. In contrast, the H_2 consumption of the Ni/CeO_2/BM catalyst occurs at much lower temperature (~185 °C) and with higher intensity, which can be attributed to the reduction of well-dispersed NiO species [180]. It's noteworthy to observe that the metal's reducibility at lower temperatures is much improved by the ball mill process. The monometallic Pd/CeO_2/BM catalyst shows a broad reduction peak centered at ~285 °C, which can be assigned to the reduction of PdO species anchored on CeO_2 [181, 182].

Additionally, the bimetallic Pd–Ni/CeO_2 catalysts prepared by both IWI and BM methods shows similar H_2–TPR profiles with a broad H_2 consumption at about ~250 °C, due to PdO–NiO reduction. The bimetallic Pd–Ni/CeO_2 catalysts exhibit the reduction at a lower temperature than monometallic Pd/CeO_2 catalyst, showing that the presence of Ni improves the reduction of PdO. In other words, there is a strong synergy between both metals, which is consistent with the results of the HRTEM (Fig–4.2c).

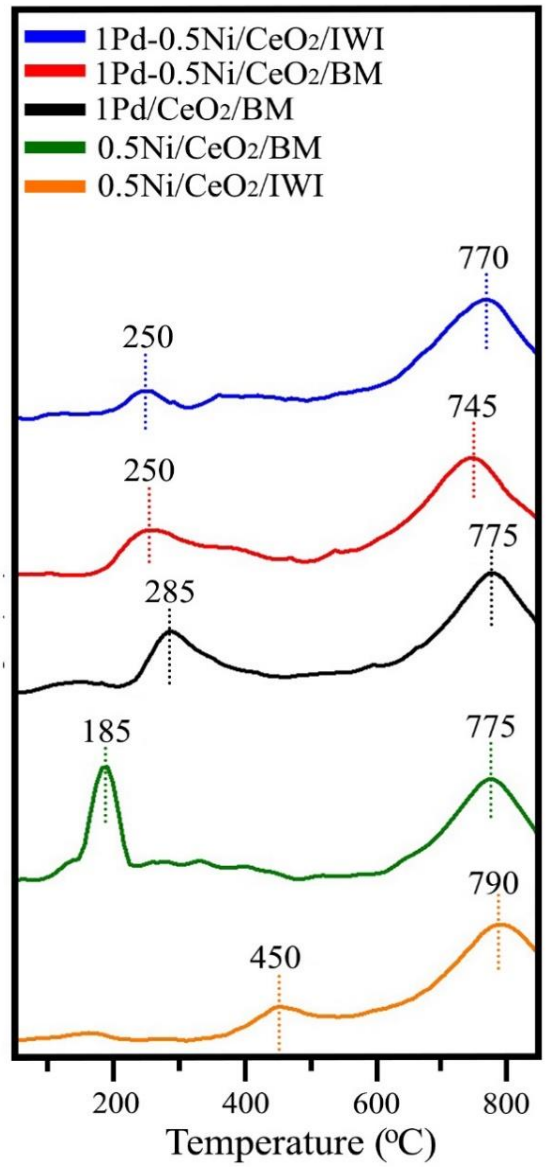

Fig-4. 3: H_2–TPR profiles corresponding to1Pd/CeO_2/BM (black), 0.5Ni/CeO_2/BM (green), 0.5Ni/CeO_2/IWI (orange), 1Pd–0.5Ni/CeO_2/IWI (blue) and 1Pd–0.5Ni/CeO_2/BM (red). Ball mill conditions: 50 Hz for 20 min.

4.1.4 X–ray Photoelectron Spectroscopy (XPS)

The surface atomic composition of the bimetallic Pd–Ni/CeO_2 catalysts prepared by the ball milling method were analyzed by X–ray photoelectron spectroscopy (XPS) as shown in Fig–4.4. Fig–4.4a illustrates the Ce 3d spectrum, where the peaks marked as v (882.7 eV), v_2 (889 eV), v_3 (899.8 eV), u (901.1 eV), u_2 (907.1 eV) and u_3 (916.9 eV) are attributed to the presence of Ce^{4+} species, and those labeled as v_0 (881.6 eV), v_1 (885 eV), u_0 (898.4 eV), and u_1 (903 eV) correspond to Ce^{3+} species

[183, 184]. It is quite clear that about 40% of cerium at the surface appears as Ce^{3+} species. On the other side, Fig-4.4b shows the Pd 3d spectrum. A single doublet corresponding to the $3d_{5/2}$ and $3d_{3/2}$ splitting is present, with a binding energy for $3d_{5/2}$ at 335.3 eV, which can be assigned well to reduce Pd. According to the surface Pd/Ce and Ni/Ce atomic ratios of 0.09 and 0.04, respectively, the two metals have an excellent dispersion over the ceria support.

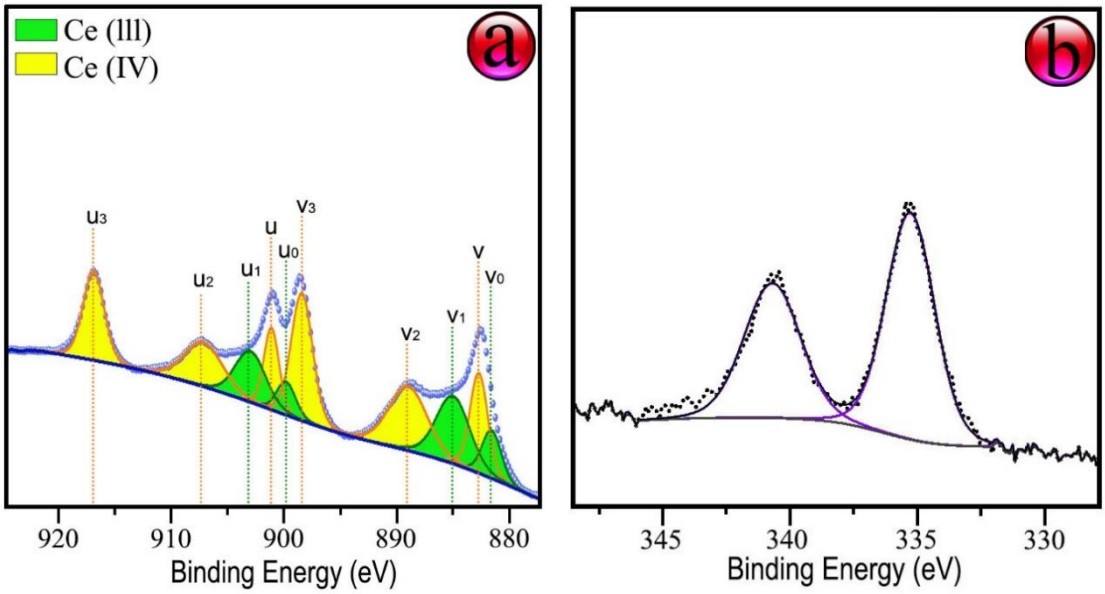

Fig-4. 4: Ce 3d (a) and Pd 3d (b) X–ray photoelectron spectra of the bimetallic 1Pd–0.5Ni/CeO_2 catalyst prepared by BM at 50 Hz for 20 min.

4.2 Catalytic tests

Similar patterns occurred in the temperature-dependent catalytic activity of the various produced catalysts. As a representative example, Fig–4.5 depicts the molar flow rates of the reactants (methane and oxygen) and the products (syngas, water, and carbon dioxide) from 300 to 550 °C of bimetallic Pd–Ni/CeO_2 catalysts made by the

BM (Fig–4.5a) and IWI (Fig–4.5b). The conversion of methane increases progressively with temperature, according with thermodynamics.

However, there are noticeable differences between catalysts prepared by BM and IWI methods. At 450 °C all the oxygen is consumed for the bimetallic 1Pd–0.5Ni/CeO_2 catalyst prepared by BM, and from this temperature the consumption of methane runs parallel to the consumption of water and the production of syngas is observed. As a result, the performance below 450 °C obeys to the equation: $CH_4 + 2O_2 \rightarrow CO_2 + 2H_2O$.

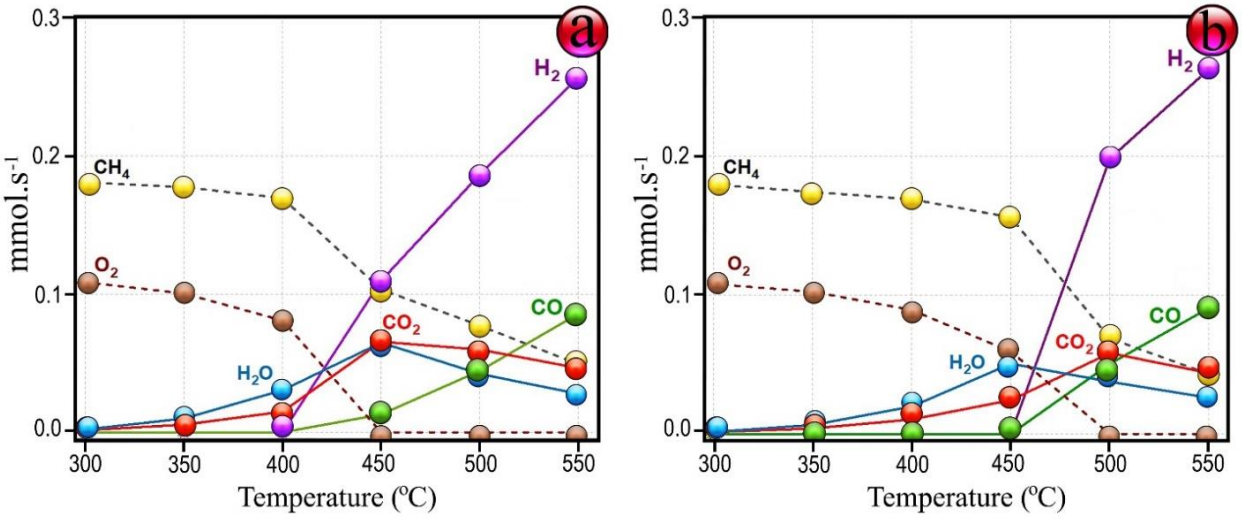

Fig-4. 5: Molar flows recorded for bimetallic catalysts 1Pd–0.5Ni/CeO_2 prepared by BM at 50 Hz for 20 min (a) and IWI (b) methods. GHSV=12 × 10^3 h^{-1}, F/W=60 L h^{-1} g^{-1}.

When all the oxygen is consumed, at higher temperatures the methane steam reforming reaction occurs: $CH_4 + H_2O \rightleftarrows CO + 3H_2$, where the conversion of methane is accompanied by the consumption of H_2O, and the production of syngas rises significantly. Simultaneously, the methane dry reforming occurs: $CH_4 + CO_2 \rightleftarrows 2CO + 2H_2$. This mechanisms corresponds to the well-known "combustion and reforming reaction (CRR)" mechanism described in the introduction section [92, 165]. Similar trend distribution and appearance of products is obtained when the bimetallic catalyst

was prepared by the conventional IWI method, confirming that the same reaction mechanisms takes place independently of the preparation method. However, all the reactions occur at higher temperatures, indicating lower catalytic activity.

Considering the two consecutive steps involved in the POM reaction and given that below 450°C the production of syngas is not significant, only the performance of the catalysts will be considered further at temperatures above 450°C. Table–4. 1 to 3 compile the catalytic results of all prepared samples in terms of methane conversion (x_{CH_4}), hydrogen selectivity (S_{H_2}), carbon monoxide selectivity (S_{CO}) and yield of syngas (Y_{syngas}). Bare CeO_2 results are also included as a blank test, as well as chemical equilibrium values.

As already pointed out, the CeO_2 support in the absence of Pd and Ni is totally inactive for POM under the reaction conditions tested, as already discussed in the precedent chapter. Additionally, the catalytic activity results for the monometallic Ni/CeO_2 catalysts (0.5 wt.% Ni) prepared by either IWI or BM methods showed low methane conversion and the formation of syngas was not observed at all. On the other side, it is quite clear that the catalytic activity of monometallic Pd/CeO_2 catalysts is much greater than that of the Ni/CeO_2 monometallic catalysts, as the methane conversion values for Pd/CeO_2 catalysts at 550 °C doubled those obtained over Ni/CeO_2 catalysts and the syngas yield was 42–48%. The milling parameters had a negligible effect on the catalytic performance of the monometallic catalysts, as methane conversion at 550 °C oscillated between 51–55% and syngas yield from 42 to 47 %.

Table–4.1. Methane conversion, hydrogen, carbon monoxide, and carbon dioxide selectivity values, and syngas yield obtained over milled CeO_2, monometallic Ni/CeO_2 and Pd/CeO_2 samples prepared by BM) and IWI methods. Metal loading values are nominal. Reaction conditions: CH_4:air:N_2 = 4: 11: 85, F/W= 60 L h^{-1} g^{-1}, GHSV= 12 × 10^3 h^{-1}.

Catalyst	Hz	min	wt.% Pd	wt.%Ni	$X_{CH_4}^{450\,°C}$	$X_{CH_4}^{550\,°C}$	$S_{H_2}^{550\,°C}$	$S_{CO}^{550\,°C}$	$Y_{Syngas}^{550\,°C}$
Equilibrium	–	–	–	–	51.3	77.9	67.2	26.3	70.9
CeO_2	–	–	–	–	0	0	0	0	0
CeO_2/BM	50	10	–	–	0	0	0	0	0
Ni/CeO_2/BM	50	10	0	0.5	3.2	22	0	0	0
Ni/CeO_2/IWI	-	-	0	0.5	3	18.6	0	0	0
Pd/CeO_2/BM	15	10	1	0	35.2	54.9	63.5	18	44.7
Pd/CeO_2/BM	30	10	1	0	31.4	51	64	18.2	41.9
Pd/CeO_2/BM	50	10	1	0	30.5	53.2	64.8	19.3	44.8
Pd/CeO_2/BM	50	20	1	0	32.7	55.6	65.2	20.2	47.6
Pd/CeO_2/BM	50	10	0.5	0	32.6	52.7	63.3	17.7	42.7
Pd/CeO_2/IWI	–	–	0.5	0	39.7	51	63.8	23	44.5
Pd/CeO_2/IWI	–	–	1	0	34.5	57.4	64.5	19.4	48.2

Table–4.2. Methane conversion, hydrogen, carbon monoxide, and carbon dioxide selectivity values, and syngas yield obtained over bimetallic Pd–Ni/CeO_2 catalysts prepared by BM technique. Metal loading values are nominal. Reaction conditions: CH_4:air:N_2 = 4: 11: 85, F/W= 60 L h^{-1} g^{-1}, GHSV= 12 × 10^3 h^{-1}

Catalyst	Hz	min	wt.%Pd	wt.%Ni	$X_{CH_4}^{450\,°C}$	$X_{CH_4}^{550\,°C}$	$S_{H_2}^{550\,°C}$	$S_{CO}^{550\,°C}$	$Y_{Syngas}^{550\,°C}$
Pd–Ni/CeO_2/BM	50	10	1	0.5	44	71.8	65.5	21.7	62.7
Pd–CeO_2/BM/Ni/BM	50	10	1	0.5	42.5	71.6	65.5	22	62.6
Ni–CeO_2/BM/Pd/BM	50	10	1	0.5	41.6	68	64.9	20.5	58.1
Pd–Ni/CeO_2/BM	15	10	1	0.5	36.4	62.4	64.2	19.2	52.1
Pd–Ni/CeO_2/BM	30	10	1	0.5	39.9	67.1	64.9	20.5	57.4
Pd–Ni/CeO_2/BM	50	5	1	0.5	37.5	67.2	65.5	20.7	57.9
Pd–Ni/CeO_2/BM	50	15	1	0.5	38	66.3	65.5	21.2	57.5
Pd–Ni/CeO_2/BM	50	20	1	0.5	42.1	72.4	66	22	63.7
Pd–Ni/CeO_2/BM	50	40	1	0.5	41.4	71.5	65.8	21.7	62.6
Pd–Ni/CeO_2/BM	50	20	0.75	0.75	37.9	67.4	65.4	21.7	58.7
Pd–Ni/CeO_2/BM	50	20	0.5	1	35.5	68.2	65.3	21.7	59.4
Pd–Ni/CeO_2/BM	50	20	0.25	1.25	37.7	70.6	65.9	23.8	63.4
Pd–Ni/CeO_2/BM	50	20	0.12	1.38	40.8	69.5	65.9	23.6	62.2
Pd–Ni/CeO_2/BM	50	20	0.06	1.44	36.6	69.5	66	23.1	62

Table–4.3. Methane conversion, hydrogen, carbon monoxide, and carbon dioxide selectivity values, and syngas yield obtained over bimetallic Pd–Ni/CeO_2 catalysts prepared IWI method. Metal loading values are nominal. Reaction conditions: CH_4:air:N_2= 4: 11: 85, F/W= 60 L h^{-1} g^{-1}, GHSV= 12 × 10^3 h^{-1}.

Catalyst	wt.%Pd	wt.%Ni	$X_{CH_4}^{450\,°C}$	$X_{CH_4}^{550\,°C}$	$S_{H_2}^{550\,°C}$	$S_{CO}^{550\,°C}$	$Y_{Syngas}^{550\,°C}$
Pd–CeO_2/IWI/Ni/IWI	1	0.5	42.2	71.7	66	21.8	63
Ni–CeO_2/IWI/Pd/IWI	1	0.5	38.5	51.5	64.6	19.5	54
Pd–Ni/CeO_2/IWI	1	0.5	12.6	75.8	66.1	22.8	67.4
Pd–Ni/CeO_2/IWI	0.75	0.75	11.6	74.8	66.2	22.5	66.3
Pd–Ni/CeO_2/IWI	0.5	1	7.7	74.4	66.3	22.8	66.3
Pd–Ni/CeO_2/IWI	0.25	1.25	6.9	70	66	21.8	63
Pd–Ni/CeO_2/IWI	0.12	1.38	2.8	67.7	65.8	23	60.2
Pd–Ni/CeO_2/IWI	0.06	1.44	3.3	65.4	66	22.9	62.6

From Table–4.2 and Table–4.3, it can be clearly seen that the cooperative effect between Pd and Ni in the bimetallic catalysts is remarkable, with a dramatic increase in both the methane conversion and the syngas yield compared to monometallic catalysts. At 550 °C, bimetallic Pd–Ni/CeO_2 catalysts show methane conversion levels from 62 to 75%, selectivity towards H_2 of 64–66%, selectivity towards CO of 19–24%, and syngas yield between 52 and 67%. These results demonstrate that the synergy between Pd and Ni supported on CeO_2 yields catalysts with improved activity and selectivity in the POM with respect to monometallic Ni/CeO_2 and Pd/CeO_2.

The catalysts preparation method (BM vs. IWI) and the order of incorporation of the metals (co–BM/co–IWI vs. sequential–BM/sequential–IWI) significantly influenced on the catalytic performance of the bimetallic Pd–Ni/CeO_2 catalysts. Fig–

4.6a displays the methane conversion for the bimetallic 1Pd–0.5Ni/CeO_2 catalysts prepared by co–IWI and sequential IWI at different temperatures. Interestingly, at low temperature (450 °C) the methane conversion of the catalysts prepared by sequential IWI is much higher than that of the catalyst prepared by co–IWI, regardless of the order of addition used for Pd and Ni. In contrast, at high temperatures (500 and 550 °C), the methane conversion attained by the catalyst prepared by co–IWI is higher than those of the catalysts prepared by sequential IWI.

Fig–4.6b shows the methane conversion for the bimetallic 1Pd–0.5Ni/CeO_2 catalysts prepared by co–BM and sequential–BM. No remarkable changes were observed between bimetallic catalysts prepared by co–BM or sequential–BM, and at each temperature, the methane conversion in all samples was similar. In any case, adding Pd first yields better catalytic results than adding Ni first, which points to a better catalytic performance when Pd interacts strongly with CeO_2, as opposed to Ni.

On the other side, the influence of milling conditions (frequency vs. time) on the catalytic activity of bimetallic Pd–Ni/CeO_2/BM catalyst at different temperatures is shown in Figs–4. 6c and 6d. Catalytic activity is strongly influenced by the energy applied during ball milling in terms of vibration frequency; the higher the energy, the better the catalyst's catalytic activity (Fig–4.6c). Therefore, it is clear that high-energy milling has a beneficial influence on the number and quality of the active sites [185, 186].

This project adds additional evidence that ball milling is able to create unprecedented architectures that can exhibit outstanding catalytic activity. The ball milling time is another important factor that can affect catalytic performance. Fig–4.6d shows the effect of the milling time (from 5 to 40 min) on the methane

conversion values. A good compromise between methane conversion and milling time is found for the catalyst prepared using 20 min of milling time. Accordingly, a ball milling frequency of 50 Hz for 20 min appears as the optimal synthesis conditions.

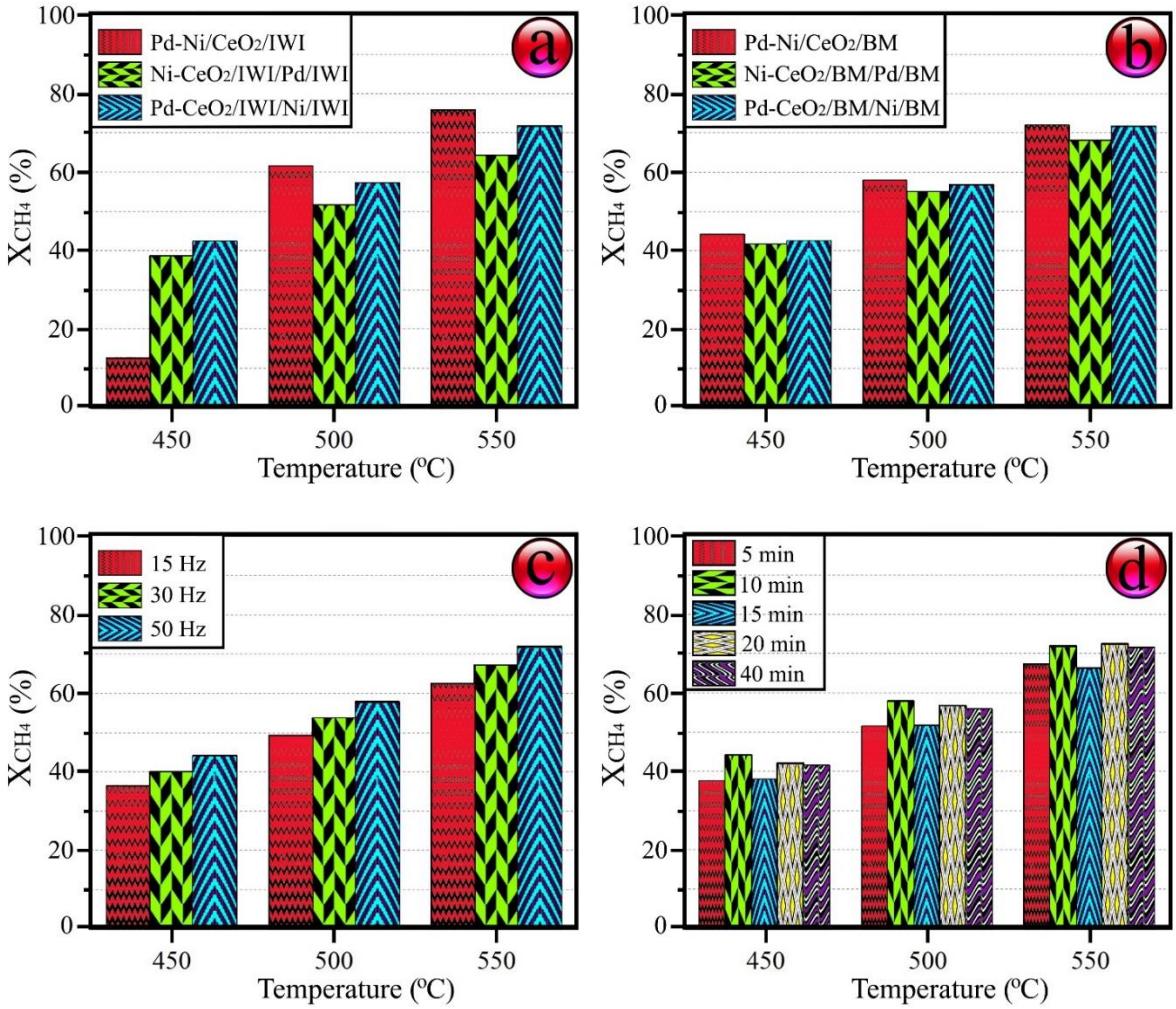

Fig-4. 6: Conversion of methane at 450, 500 and 550 °C over bimetallic 1Pd–0.5Ni/CeO_2 catalysts prepared by IWI (a), BM at 50 Hz for 10 min (b), BM at different milling frequency for 10 min (c), and BM at 50 Hz for different milling time (d). GHSV=12 × 10^3 h^{-1}, F/W=60 L h^{-1} g^{-1}.

A crucial aspect regarding bimetallic catalysts is the relative amount of the two metals involved. In our case, it should also be taken into account that Pd is

significantly more expensive than Ni, which obviously has a direct impact on the catalyst's final cost. Fig–4.7 illustrates the methane conversion and syngas yield at 450 °C and 550 °C exhibited by xPd–yNi/CeO_2 catalysts prepared by BM and IWI techniques, having varying amounts of Pd and Ni but maintaining the overall metal loading at 1.5 wt.% (x = 0.06 to 1% and y = 0.5 to 1.44%).

Two factors merit particular attention. First, it is very interesting to observe that at 450 °C both the methane conversion (Fig–4.7a) and syngas yield (Fig–4.7c) are much higher for all the catalysts prepared by BM with respect to their respective counterparts prepared by the IWI method. This proves clearly that very reactive and specific active sites are created by the BM method, which are highly active for the POM process at low temperature. At 550 °C, the catalytic function of both xPd–yNi/CeO_2/BM and xPd–yNi/CeO_2/IWI catalysts are similar. Second, the effect of the Pd amount on the catalytic performance is lower than was predicted and is also influenced by the preparation method. There is a correlation between Pd content (x) and methane conversion for the xPd–yNi/CeO_2/IWI catalysts: the higher the Pd content, the higher the methane conversion.

In contrast, both the methane conversion and syngas yield for the xPd–yNi/CeO_2/BM catalysts are not sensitive to the relative quantities of Pd and Ni in the examined range. It is important to note that the Ni/CeO_2/BM sample showed low methane conversion (3.2% at 450 °C and 22% at 550 °C, Table–4.1) and no syngas production, whereas with only 0.06 wt.% Pd the methane conversion increased up to 36.6 and 69.5% at 450 and 550 °C, respectively, and syngas yield was 62% (Table–4.2). The bimetallic Pd–Ni system certainly seems to be a particularly appealing metal combination for POM process. Recent DFT calculations have demonstrated that the

substitution of Ce by Pd ions in the surface of the catalysts originates highly active and stable species based on $Pd_xCe_{1-x}O_\delta$ which are highly effective in the rapid C–H bond activation [166, 168]. From the HRTEM images, we cannot determine if Pd substitutes Ce in the ceria structure, but we do have proof that both Pd and Ni are extensively dispersed at the subnanometric level. The greatest performance (both methane conversion and syngas yield) was reported for Pd–Ni/CeO_2/BM with 0.12 wt% Pd and 1.38 wt% Ni at low temperature (450 °C), where the bimetallic Pd–Ni catalysts prepared by BM exhibit a particularly high activity for POM.

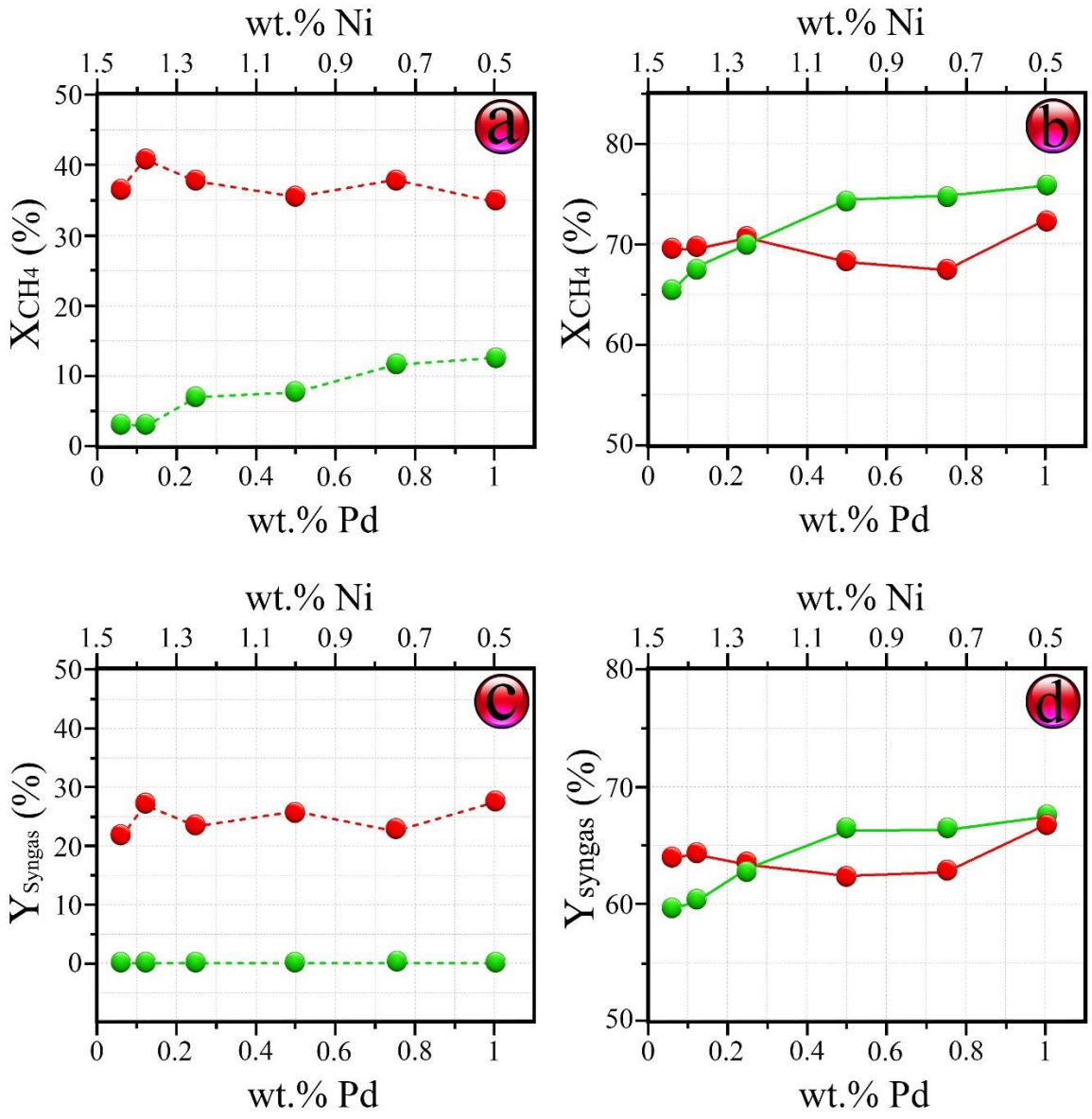

Fig-4. 7: Conversion of methane at 450 °C (a) and 550 °C (b) and yield of syngas at 450 °C (c) and 550 °C (d) for the bimetallic xPd–yNi/CeO_2 catalysts containing different amounts of Pd and Ni prepared by BM (red) and IWI (green) methods. All catalysts contain a total metal loading of 1.5 wt.%. GHSV=12 × 10^3 h^{-1}, F/W=60 L h^{-1} g^{-1}.

4.3 Characterization of the catalysts after reaction

Fig–4.8 displays the Raman spectra obtained from the catalysts Pd–Ni/CeO_2/BM and Pd–Ni/CeO_2/IWI after the catalytic test discussed above. For both bimetallic catalysts the position of the F_{2g} band of CeO_2 did not shift after the catalytic test with respect to the values recorded before reaction (Fig–4.1), and the residual nitrate signals in the sample Pd–Ni/CeO_2/BM disappeared due to decomposition after reaction. Furthermore, the two characteristic graphite D and G bands at about ~1345 and ~1595 cm^{-1} [187, 188] were observed in the Raman spectra of the catalysts after reaction, being their relative contribution in the spectra considerably more intense in the case of the bimetallic sample prepared by impregnation.

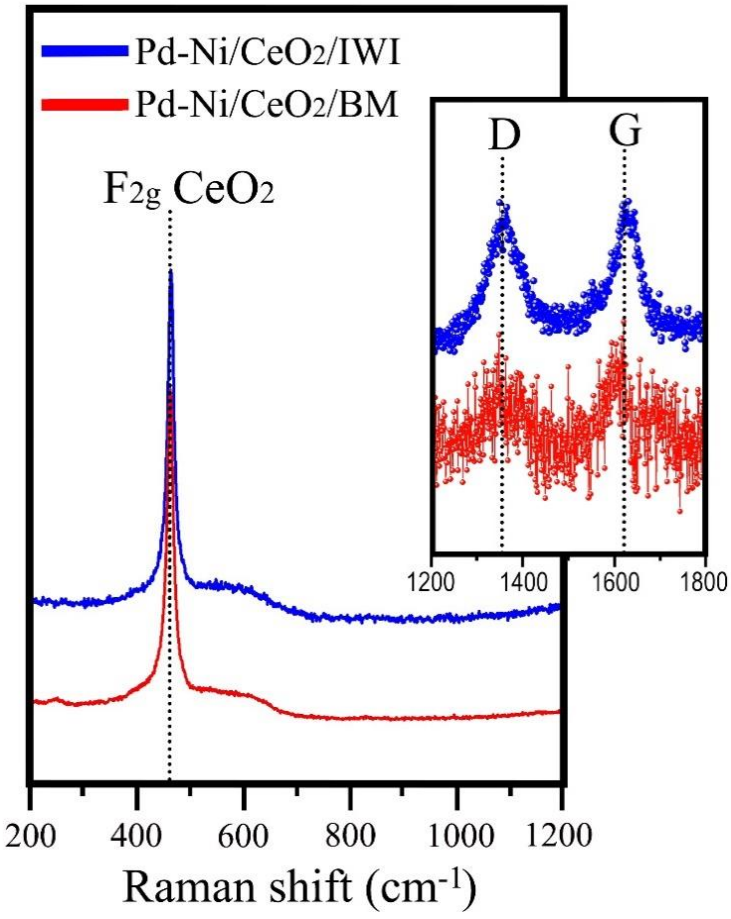

Fig-4. 8: Raman spectra of bimetallic 1Pd–0.5Ni/CeO_2 catalysts prepared by BM at 50 Hz for 20 min (red), and IWI (blue) after reaction (CH_4:air:N_2=4:11:85, F/W=60 L h^{-1} g^{-1}, GHSV=12 × 10^3 h^{-1}).

Consequently, less coke deposition occurred on the bimetallic sample prepared by ball milling. Catalyst Pd–Ni/CeO_2/BM was studied by HRTEM and EDX (Fig–4.9). It's interesting to note that several voids are identified in the ceria crystallites that were not visible in the sample before reaction (Fig–4.2c).

They are speculatively attributed to clusters of oxygen vacancies, probably in contact with the metals, created under the reducing environment created by syngas during POM. On the other hand, Pd and/or Ni particles escape detection in HRTEM, indicating that the high dispersion of the metals is maintained during the catalytic reaction. In addition, and in accordance with the Raman results, coke is identified by its characteristic spacing at 3.8 Å, which is attributed to the (0001) interplanar spacing of poorly ordered graphite. However, the amount of deposited coke is not much.

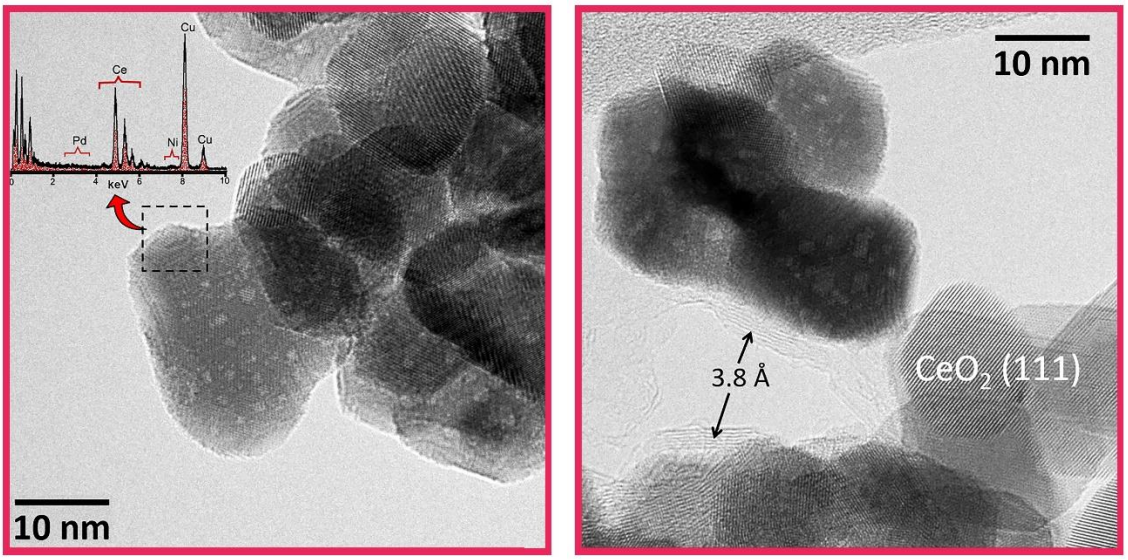

Fig-4. 9: HRTEM images of the bimetallic 1Pd–0.5Ni/CeO_2 catalyst prepared by BM at 50 Hz for 20 min, after the catalytic test.

4.4 Stability tests

Stability tests were carried out for more than 100 h at 550 °C to demonstrate the catalysts' long-term performance. Since bimetallic catalysts indicated good methane conversion and selectivity to syngas (Table–4.2 and Table–4.3), Pd–Ni/CeO_2 catalysts with 1 wt.% Pd and 0.5 Ni loading prepared by both IWI and BM techniques were examined. A monometallic Pd/CeO_2 catalyst prepared by BM with 1 wt.% Pd was also tested for comparison purposes. The methane conversion and yield of syngas are shown in Figs–4. 10a and 10b, respectively.

As expected, both the initial methane conversion and syngas yield of the bimetallic catalysts were significantly higher than those of the monometallic sample, and the Pd–Ni/CeO_2/BM catalyst performed better than Pd–Ni/CeO_2/IWI. More interestingly, the catalytic performance of the three samples revealed a constant decline of the methane conversion rate of ~0.32% h^{-1} and ~0.37% h^{-1} for the bimetallic catalysts prepared by BM and IWI methods, respectively, and ~0.32% h^{-1} for the monometallic sample up to the first 40 h on stream. However, after 40 hours, both the methane conversion and syngas production of the bimetallic catalyst prepared by BM had reached a steady state, and the deactivation rate was almost inexistent (0.01% h^{-1}). In comparison, the deactivation of the bimetallic catalyst prepared by IWI and the monometallic sample Pd/CeO_2/BM did not stop and continued progressing with a similar rate. Therefore, the bimetallic Pd–Ni/CeO_2 sample prepared by BM not only demonstrated higher methane conversion and syngas production, but also a remarkable higher stability.

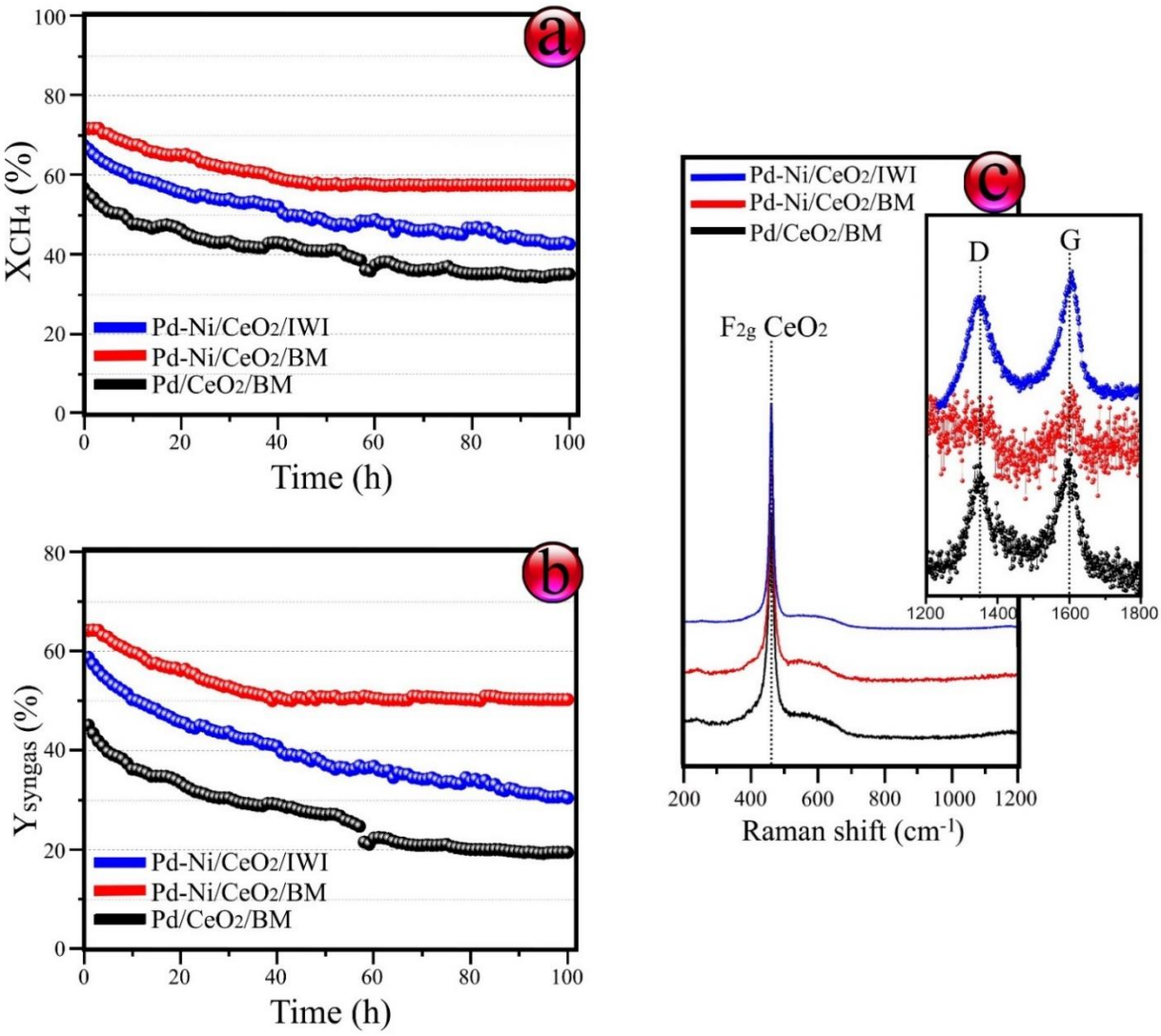

Fig-4. 10: Methane conversion (a) and syngas yield (b) in long-term stability tests at 550 °C of bimetallic 1Pd–0.5Ni/CeO_2/IWI (blue) and 1Pd–0.5Ni/CeO_2/BM (red) catalysts, and monometallic 1Pd/CeO_2/BM (black). GHSV=12 × 10^3 h^{-1}, F/W= 60 L h^{-1} g^{-1}. Raman spectra recorded on these catalysts after the stability test (c).

The Raman spectra of the carbon region for the three samples after the long-term stability test are displayed in Fig–4.10c. The spectra indicate three signals at ~1200, ~1345 and ~1595 cm^{-1}, which correspond to the second-order longitudinal optical mode (2LO) of CeO_2 and the D and G characteristic bands of carbon, respectively [90, 157]. The intensity of the D and G bands of carbon follows the trend Pd–

$Ni/CeO_2/IWI$ > $Pd/CeO_2/BM$ >> $Pd–Ni/CeO_2/BM$, which is exactly the opposite pattern of stability. It can be concluded that the higher stability of the bimetallic sample prepared by BM is related to its ability to suppress the deposition of carbon during POM process. This again points to the existence of unique active sites in the catalyst originating from an intimate and unique synergy between Pd and Ni on CeO_2 thanks to ball milling.

4.5 Conclusions

Monometallic Pd and Ni and bimetallic Pd–Ni catalysts supported on CeO_2 were produced by BM and IWI methods, and were characterized and evaluated to produce syngas using the POM process at 300–550 °C. The catalytic results indicated that the methane conversion and syngas yield followed this trend: $Pd–Ni/CeO_2/BM$ > $Pd–Ni/CeO_2/IWI$ >> $Pd/CeO_2/BM$ > $Pd/CeO_2/IWI$ >> $Ni/CeO_2/BM$ > $Ni/CeO_2/IWI$ >> CeO_2. A strong synergy between Pd and Ni on CeO_2 occurs in the bimetallic samples prepared by BM, leading to a significant increase in the number of active sites for POM reaction, especially at low temperature (450 °C).

Moreover, Raman spectroscopy, HRTEM–EDX, XPS and H_2–TPR point to an extremely high dispersion of Pd and Ni in $Pd–Ni/CeO_2/BM$. Furthermore, compared to the bimetallic $Pd–Ni/CeO_2$ catalysts prepared by IWI, the bimetallic catalysts prepared by BM not only produced syngas at lower temperature, but also revealed higher catalytic stability in long-term experiments (100 h on stream at 550 °C). This was related to less carbon deposition.

Another important result of this chapter was obtained by studying the influence of Pd and Ni loadings in the bimetallic $Pd–Ni/CeO_2$ catalysts prepared by BM and

IWI. A series of bimetallic catalysts were prepared by keeping a total metal loading of 1.5 wt.% and varying the Pd amount between 0.016 and 1 wt.%. Whereas methane conversion increased gradually with the Pd content for the Pd–Ni/CeO_2/IWI catalysts, it was maintained approximately constant for the Pd–Ni/CeO_2/BM samples, with maximum methane conversion and syngas yield values for 0.12Pd–1.38Ni/CeO_2/BM. This result suggests that highly active catalysts for POM can be designed by properly ball milling small amounts of Pd with Ni. The optimal ball milling parameters were 50 Hz and 20 min (BPR=10.2).

4.6 References

1. Fleys, M., et al., Investigation of the reaction of partial oxidation of methane over Ni/La_2O_3 catalyst. Energy & Fuels, 2006. **20**(6): p. 2321-2329.
2. York, A.P., T. Xiao, and M.L. Green, Brief overview of the partial oxidation of methane to synthesis gas. Topics in Catalysis, 2003. **22**(3): p. 345-358.
3. Rostrup-Nielsen, J.R., Fuels and energy for the future: the role of catalysis. Catalysis reviews, 2004. **46**(3-4): p. 247-270.
4. Wu, Z., et al., Probing defect sites on CeO_2 nanocrystals with well-defined surface planes by Raman spectroscopy and O_2 adsorption. Langmuir, 2010. **26**(21): p. 16595-16606.
5. Carter, J.C., et al., Raman spectroscopic evidence supporting the existence of Ni_4 (OH) 44+ in aqueous, Ni $(NO_3)_2$ solutions. Analytica Chimica Acta, 2004. **514**(2): p. 241-245.
6. Lucentini, I., et al., Ammonia decomposition over 3D-printed CeO_2 structures loaded with Ni. Applied Catalysis A: General, 2020. **591**: p. 117382.
7. Weber, W., K. Hass, and J. McBride, Raman study of CeO_2: Second-order scattering, lattice dynamics, and particle-size effects. Physical Review B, 1993. **48**(1): p. 178.
8. Danielis, M., et al., Outstanding Methane Oxidation Performance of Palladium-Embedded Ceria Catalysts Prepared by a One-Step Dry Ball-Milling Method. Angewandte Chemie, 2018. **130**(32): p. 10369-10373.
9. Rynkowski, J.M., et al., Characterization of Ru/CeO_2-Al_2O_3 catalysts and their performance in CO_2 methanation. Reaction Kinetics and Catalysis Letters, 2000. **71**(1): p. 55-64.

10. Tanksale, A., et al., Effect of Pt and Pd promoter on Ni supported catalysts—A TPR/TPO/TPD and microcalorimetry study. Journal of Catalysis, 2008. **258**(2): p. 366-377.
11. Rynkowski, J., T. Paryjczak, and M. Lenik, On the nature of oxidic nickel phases in NiO/γ-Al_2O_3 catalysts. Applied Catalysis A: General, 1993. **106**(1): p. 73-82.
12. Mierczynski, P., et al., High active and selective Ni/CeO_2–Al_2O_3 and Pd–Ni/CeO_2–Al_2O_3 catalysts for oxy-steam reforming of methanol. Catalysts, 2018. **8**(9): p. 380.
13. Kugai, J., et al., Effects of nanocrystalline CeO_2 supports on the properties and performance of Ni–Rh bimetallic catalyst for oxidative steam reforming of ethanol. Journal of Catalysis, 2006. **238**(2): p. 430-440.
14. Mierczynski, P., W. Maniukiewicz, and T.P. Maniecki, Comparative studies of Pd, Ru, Ni, Cu/$ZnAl_2O_4$ catalysts for the water gas shift reaction. Central European Journal of Chemistry, 2013. **11**(6): p. 912-919.
15. Luo, M.-F., et al., Characterization study of CeO_2 supported Pd catalyst for low-temperature carbon monoxide oxidation. Catalysis letters, 1998. **50**(3): p. 205-209.
16. Jen, H.-W., et al., Characterization of model automotive exhaust catalysts: Pd on ceria and ceria–zirconia supports. Catalysis Today, 1999. **50**(2): p. 309-328.
17. Pang, J., et al., Mesoporous Cu_2O–CeO_2 composite nanospheres with enhanced catalytic activity for 4-nitrophenol reduction. Applied Surface Science, 2018. **439**: p. 420-429.
18. Molinari, M., et al., Water adsorption and its effect on the stability of low index stoichiometric and reduced surfaces of ceria. The Journal of Physical Chemistry C, 2012. **116**(12): p. 7073-7082.

19. Enger, B.C., R. Lødeng, and A. Holmen, A review of catalytic partial oxidation of methane to synthesis gas with emphasis on reaction mechanisms over transition metal catalysts. Applied Catalysis A: General, 2008. **346**(1-2): p. 1-27.
20. York, A.P., T. Xiao, and M.L. Green, Brief overview of the partial oxidation of methane to synthesis gas. Topics in Catalysis, 2003. **22**(3-4): p. 345-358.
21. Chen, Y., et al., A straightforward method to prepare supported Au clusters by mechanochemistry and its application in photocatalysis. Applied Materials Today, 2020. **21**: p. 100873.
22. Leitenburg, C., A novel and simple route to catalysts with a high oxygen storage capacity: the direct room-temperature synthesis of CeO_2–ZrO_2 solid solutions. Journal of the Chemical Society, Chemical Communications, 1995(21): p. 2181-2182.
23. Senftle, T.P., A.C. Van Duin, and M.J. Janik, Role of Site Stability in Methane Activation on $Pd_x Ce_{1-x} O_\delta$ Surfaces. ACS Catalysis, 2015. **5**(10): p. 6187-6199.
24. Senftle, T.P., A.C. Van Duin, and M.J. Janik, Methane activation at the Pd/CeO_2 interface. ACS Catalysis, 2017. **7**(1): p. 327-332.
25. Han, Z., et al., Propane dehydrogenation over Pt–Cu bimetallic catalysts: the nature of coke deposition and the role of copper. Nanoscale, 2014. **6**(17): p. 10000-10008.
26. Chen, Y. and J. Chen, Selective hydrogenation of acetylene on SiO_2 supported Ni-In bimetallic catalysts: Promotional effect of In. Applied Surface Science, 2016. **387**: p. 16-27.
27. Fazlikeshteli, S., X. Vendrell, and J. Llorca, Low-Temperature Methane Partial Oxidation over Pd Supported on CeO_2: Effect of the Preparation Method and Precursors. Reactions, 2021. **2**(1): p. 30-42.

CHAPTER 5

5. Catalytic partial oxidation of methane over bimetallic Ru–Ni supported on CeO_2 for syngas production

Abstract

In this chapter, we focus on Ru–Ni bimetallic catalysts supported on CeO_2 to conduct the POM process at low temperature (350–600 °C). A number of monometallic Ru, Ni, and bimetallic Ru–Ni catalysts loaded on CeO_2 support have been prepared via BM and IWI methods. Similar to the previous chapters, we also have investigated the importance of metal loading, the Ru:Ni metal ratio and order of incorporation of the metals, and the milling energy and time for samples prepared by the mechanochemical method, and compared the results with monometallic Ru–CeO_2 and Ni–CeO_2 counterparts.

5.1 Characterization of fresh catalysts

5.1.1 Raman spectroscopy

Fig–5.1 shows the Raman spectra of fresh monometallic Ru, Ni, and bimetallic Ru–Ni catalysts supported on CeO_2 prepared by BM and IWI methods. To ensure the homogeneity of the samples, multiple spectra were recorded from different areas, and no variations were observed. The Raman spectra were dominated by the strong F_{2g} mode of the ceria lattice structure at about ~460 cm^{-1} [1-3]. The defect-induced vibrational mode at about ~595 cm^{-1} (D band) of ceria lattice defects, such as oxygen vacancies, was absent in all samples. This

absence indicates that the incorporation of Ni and Ru into the ceria structure did not lead to the formation of lattice defects [4].

In the Raman spectra of the monometallic 0.5Ni/CeO_2/BM and 1Ni/CeO_2/BM catalysts, a faint band was observed at approximately 1060 cm^{-1}, corresponding to the symmetric ν_1 stretching mode of the nitrate anion [5, 6]. Conversely, in the Raman spectra of the monometallic 0.5Ru/CeO_2, 1Ru/CeO_2, and bimetallic 1Ru–0.5Ni/CeO_2 catalysts prepared by IWI method, a band at around 720 cm^{-1} was observed. This band is attributed to the B_{2g} mode of RuO_2 [7]. Furthermore, an extended broadband ranging from approximately 675 to 690 cm^{-1} was observed in the spectra of the monometallic 0.5Ru/CeO_2/BM, 1Ru/CeO_2 catalysts prepared by both IWI and BM, and the bimetallic 1Ru–0.5Ni/CeO_2/BM. This broadband is attributed to the A_{1g} mode of RuO_x, indicating a strong interaction between Ru species and the ceria support [7]. The additional bands observed at approximately 700 and 980 cm^{-1} in the spectra of the 1Ru/CeO_2/BM (spectrum c), and the bimetallic 1Ru–0.5Ni/CeO_2/BM (spectrum a) catalysts were attributed to the presence of the Ru–OC–e bond [1, 8]. Also, the presence of a band in the range of 300 to 360 cm^{-1} for the monometallic 0.5Ru/CeO_2, 1Ru/CeO_2, and bimetallic 1Ru–0.5Ni/CeO_2 (spectrum a) samples prepared by BM indicates an intimate interaction between the CeO_2 support and the metals [9].

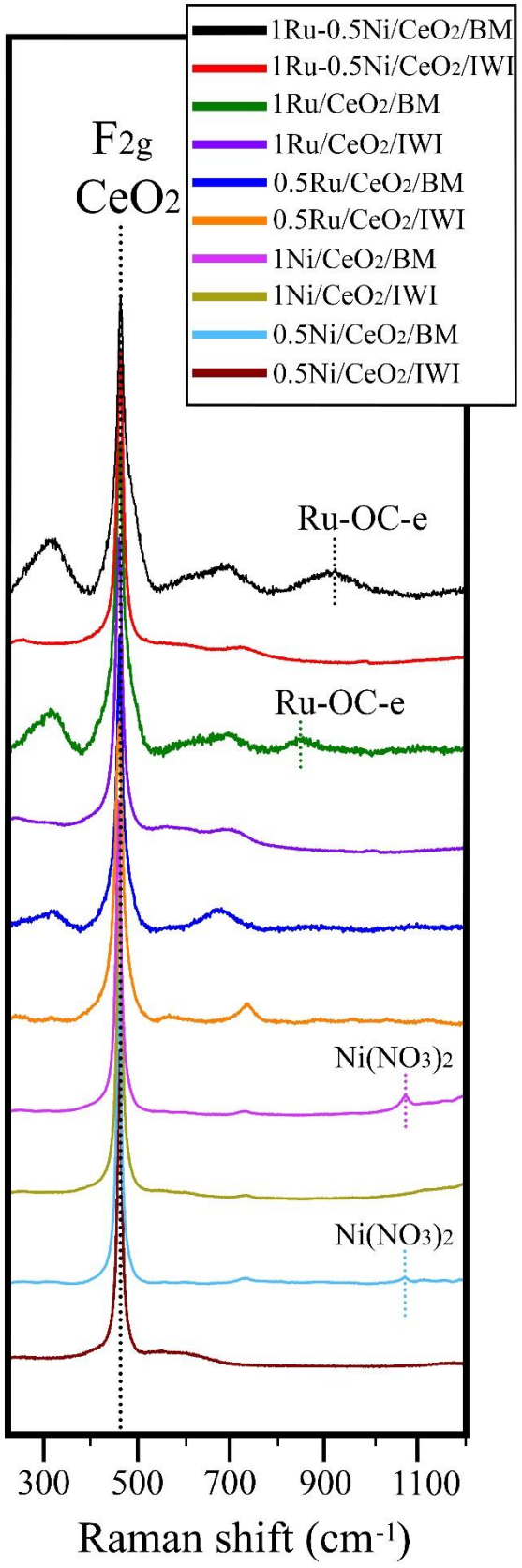

Fig-5. 1: Raman spectra of monometallic xRu/CeO_2 and yNi/CeO_2 samples prepared by BM and IWI methods, and bimetallic catalysts $1Ru–0.5Ni/CeO_2$/BM and $1Ru–0.5Ni/CeO_2$/IWI. Ball mill conditions: 50 Hz and 15 min.

5.1.2 Temperature–programmed reduction (H_2–TPR)

The intimate interaction between the metals (Ru, Ni) and the CeO_2 support was confirmed by H_2–TPR measurements, as depicted in Fig–5.2. The H_2–TPR profile of the CeO_2 support exhibited two distinct peaks at temperatures of 530 and 800 °C. The peak at 530 °C corresponds to the surface reduction of ceria, which involves the formation of bridging OH– groups, and the peak observed at 800 °C corresponds to the reduction of bulk Ce(IV) to Ce(III) within the ceria lattice [9, 10]. Notably, the reduction peak corresponding to bulk CeO_2 in the bimetallic Ru–Ni catalysts exhibited a remarkable shift towards lower temperatures with respect to the monometallic samples and to pure CeO_2. This is a clear indication of the existence of a strong synergy between the two metals and the support. Moreover, the changes in the surface reduction of ceria after decoration with the metals are also remarkable as both Ru and Ni are known to possess the ability to adsorb hydrogen on their surfaces, which in turn facilitates the transportation of the generated atomic hydrogen to the CeO_2 support.

The H_2 consumption profiles of the monometallic 0.5Ni/CeO_2/BM and 0.5Ni/CeO_2/IWI catalysts displayed multiple peaks at approximately 160–240 °C, corresponding to the reduction of surface NiO species [9, 11]. In addition, the H_2 consumption profile of the Ni monometallic catalysts prepared by IWI showed a peak at around 430 °C, attributed to the reduction of surface ceria, which was shifted to a lower temperature [12] with respect to bare ceria. In contrast, the 0.5Ni/CeO_2/BM sample shows hydrogen consumption at much lower temperature, indicative of a stronger interaction between Ni species and the ceria support. Therefore, the use of the ball milling method yields a catalyst with distinct metal-support interaction, resulting in a more reactive surface than that of the Ni/CeO_2 sample prepared by impregnation. Similarly, the hydrogen consumption for the Ru catalyst prepared by ball

milling occurs at a lower temperature with respect to the conventional Ru catalyst prepared by impregnation. For both samples, peaks at about 230 and 100 °C are attributed to the reduction of RuO_x–type oxides, which are distinct from pure ruthenium oxide [13]. Special attention merits the spectra of the bimetallic samples. In addition to a strong shift toward lower temperature of the peak corresponding to the bulk reduction of the ceria support, catalyst 1Ru–0.5Ni/CeO_2/BM exhibits a sharp and intense hydrogen consumption at very low temperature (ca. 100 °C), again pointing out to a particular surface architecture of the sample prepared by mechanochemistry and indicating that the simultaneous presence of Ru and Ni has a positive influence on the reducibility of CeO_2.

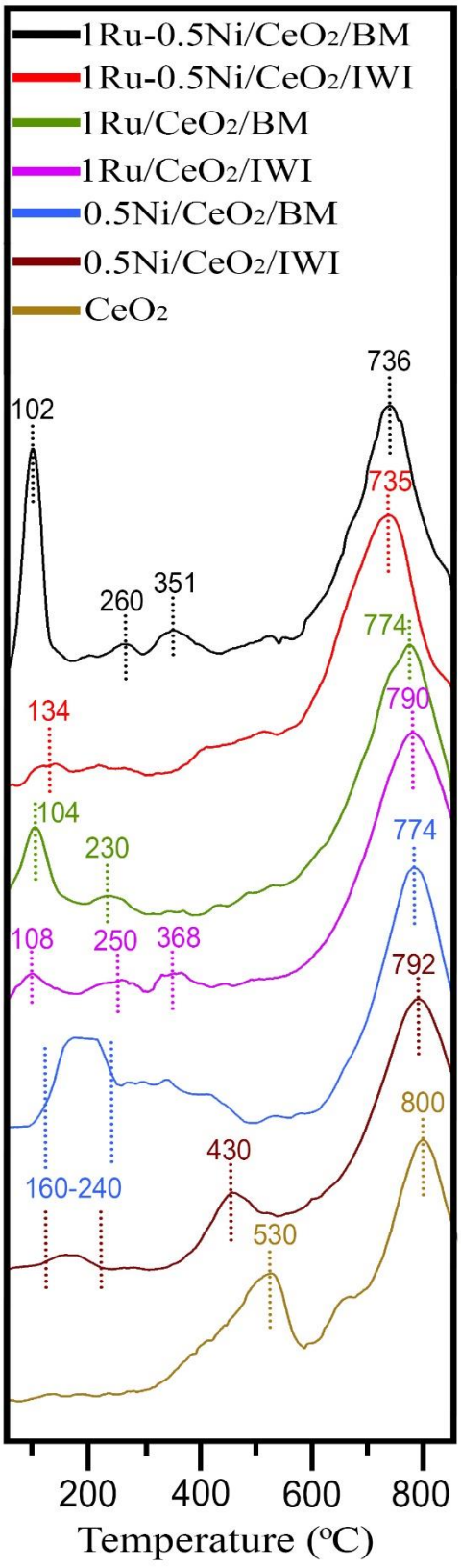

Fig-5. 2: H_2–TPR results of CeO_2, monometallic 1Ru/CeO_2, 0.5Ni/CeO_2 samples, and bimetallic 1Ru–0.5Ni/CeO_2 catalysts prepared by BM and IWI methods. Ball mill conditions: 50 Hz and 15 min.

5.1.3 X–ray Photoelectron Spectroscopy (XPS)

To investigate the surface atomic composition of the monometallic 1Ru/CeO_2, 1Ni/CeO_2, and bimetallic 0.5Ru–1Ni/CeO_2 catalysts prepared by BM and IWI methods, X–ray photoelectron spectroscopy (XPS) was employed. The Ce 3d + Ni 2p XPS region of all the samples is depicted in Fig–5.3a. In the Ce 3d spectra, no significant changes are observed among the different catalysts. The peaks denoted as v (882.7 eV), v_2 (889.0 eV), v_3 (899.8 eV), u (901.1 eV), u_2 (907.1 eV), and u_3 (916.9 eV) are attributed to the presence of Ce^{4+} species, while v_0 (881.6 eV), v_1 (885.0 eV), u_0 (898.4 eV), and u_1 (903.0 eV) correspond to Ce^{3+} species [14, 15]. As indicated in Table–5.1, the Ce 3d signal deconvolution for all the monometallic and bimetallic catalysts revealed that less than ca. 20% of the ceria surface consisted of Ce^{3+} species.

The binding energy value of the Ni $2p_{3/2}$ signal at 854.9-855.0 eV observed in the monometallic 1Ni/CeO_2 and bimetallic 0.5Ru–1Ni/CeO_2 catalysts (Table–5.1), prepared by both the BM and IWI methods, is consistent and indicative of NiO. No significant differences are found between the samples prepared by BM and IWI in terms of the Ni $2p_{3/2}$ signal. However, it is worth noting that the Ni/Ce surface atomic ratios are slightly lower in the samples prepared by BM compared to those prepared by IWI (Table–5.1), which may indicate a better dispersion in the IWI samples or, alternatively, that Ni is partially incorporated into the subsurface region of the sample due to the high energy involved in the BM process. All the catalysts exhibit a Ru $3d_{5/2}$ peak in the range of 280.4–280.9 eV, which corresponds to oxidized Ru species (Fig–5.3b) [11]. Notably, the binding energies of the samples prepared by BM are significantly higher than those prepared by IWI, suggesting a stronger electron

donation between Ru and ceria in the BM samples. Again, the Ru/Ce surface atomic ratio is higher in the samples prepared by IWI with respect to BM (Table–5.1).

Table-5.1. The percentage of Ce^{3+} and Ce^{4+}, binding energies and integrated peak areas of Ni $2p_{3/2}$, Ru $3d_{5/2}$, and surface atomic Ni/Ce and Ru/Ce values.

Catalysts	Ce^{3+} %	Ce^{4+} %	Ni $2p_{3/2}$	Ru $3d_{5/2}$	Ni/Ce	Ru/Ce
1Ru–0.5Ni/CeO_2/BM	15.8	84.2	854.9	280.7	0.011	0.036
1Ru–0.5Ni/CeO_2/IWI	17.9	82	854.9	280.5	0.016	0.038
1Ru/CeO_2/BM	19.1	80.9	-	280.9	-	0.014
1Ru/CeO_2/IWI	20.1	79.9	-	280.4	-	0.034
1Ni/CeO_2/BM	16.27	83.7	854.9	-	0.024	-
1Ni/CeO_2/IWI	20.1	79.9	855.0	-	0.027	-

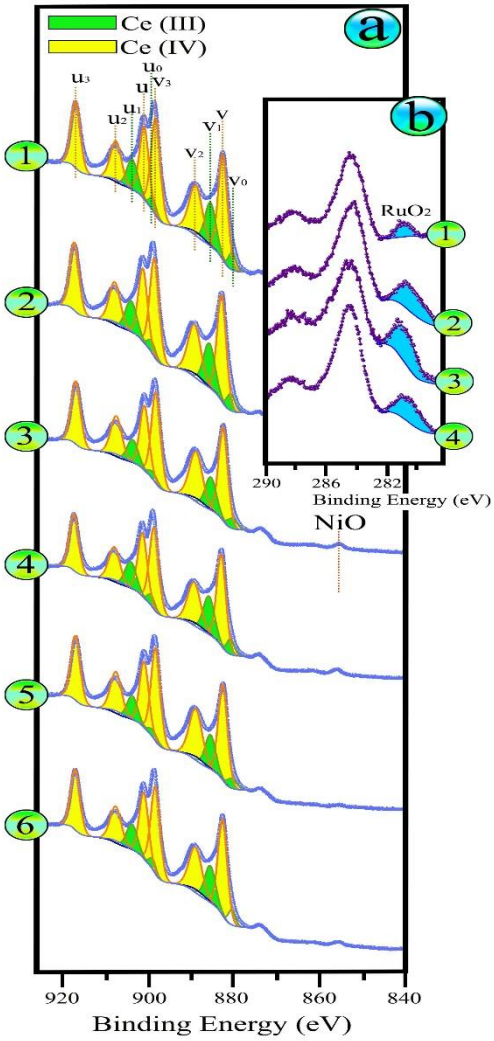

Fig-5. 3: Ce 3d + Ni 2p (a) and Ru $3d_{5/2}$ (b) X–ray photoelectron spectra of monometallic catalysts 1Ru/CeO_2/BM (1), 1Ru/CeO_2/IWI (2), 1Ni/CeO_2/BM (5), 1Ni/CeO_2/IWI (6), and bimetallic 1Ru–0.5Ni/CeO_2 catalysts prepared by BM (3) and IWI (4) methods. Ball mill conditions: 50 Hz and 15 min.

5.2 Catalytic tests

The molar flow rates of reactants (CH_4 and O_2) and products (H_2, CO, H_2O, and CO_2) as a function of the reaction temperature from 350 to 600 °C of catalysts 1Ru–0.5Ni/CeO_2 and 1Ru/CeO_2 prepared by both IWI and BM methods are shown in Fig–5.4. According to the distribution of reactants and products observed and according to literature [16-20], the POM process occurs in two steps. In the first step, CH_4 is first partially oxidized to produce CO_2 and H_2O; then, as the temperature increases, the remaining unreacted CH_4 is reformed with water (SRM, Eq. 1) and CO_2 (dry reforming, $CH_4 + CO_2 \longrightarrow 2CO + 2H_2$). Finally, the water gas-shift equilibrium is also operative ($CO + H_2O \rightleftarrows CO_2 + H_2$). Clearly, the bimetallic Ru–Ni catalyst prepared by ball milling (Fig–5.4a) showed higher catalytic activity and better syngas selectivity under the same operation conditions compared with the homologous IWI catalyst (Fig–5.4b) and also to the monometallic samples (Fig–5.4c and Fig–5.4d), pointing out to a beneficial effect of the synergy between Ru and Ni and the importance of the preparation method. The differences are particularly appealing at low temperature (550 ºC). This effect is analogous to those previously described for ceria–supported bimetallic Ni–Pd catalyst [21].

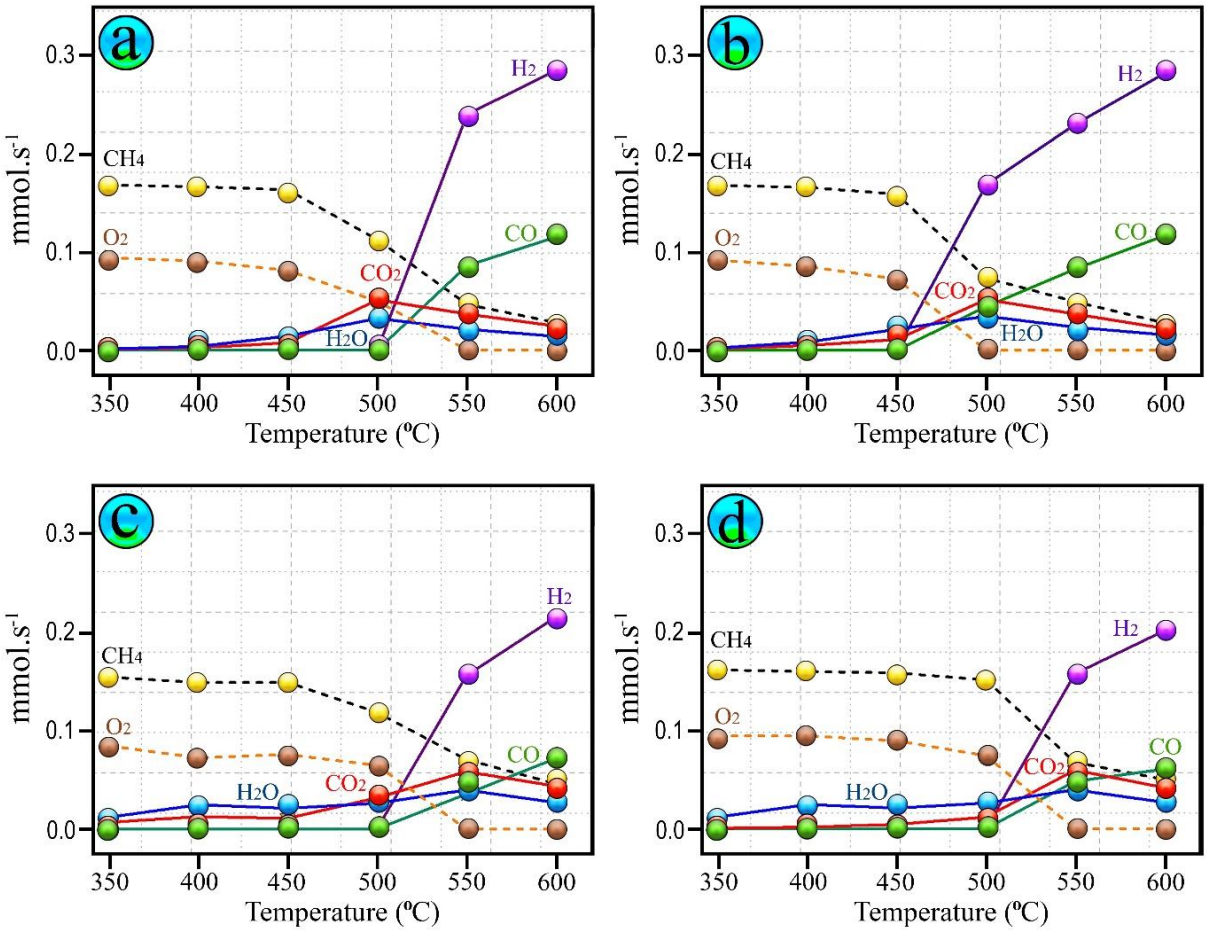

Fig-5. 4: Molar flows of bimetallic catalysts 1Ru–0.5Ni/CeO_2 prepared by IWI (a) and BM (b) methods, and monometallic catalysts 1Ru/CeO_2/IWI (c), 1Ru–CeO_2/BM (d). GHSV=12 × 10^3 h^{-1}, F/W=60 L h^{-1} g^{-1}. Ball mill conditions: 50 Hz and 15 min.

The catalytic results for all samples investigated in this work in terms of CH_4 conversion (x_{CH_4}), H_2 selectivity (S_{H_2}), CO selectivity (S_{CO}), CO_2 selectivity (S_{CO_2}), and yield of syngas (Y_{sg}) are compiled in Table–5.2, Table–5.3, and Table–5.4, as well as the calculated chemical equilibrium values.

Table–5.2. Methane conversion, hydrogen, carbon monoxide, and carbon dioxide selectivity values, and syngas yield obtained over milled CeO_2, monometallic Ru/CeO_2 and Ni/CeO_2 samples prepared by ball milling (BM) and incipient wetness impregnation (IWI). Metal loading values are nominal. Reaction conditions: CH_4:air:N_2=4:11:85, F/W=60 L h^{-1} g^{-1}, GHSV=12 × 10^3 h^{-1}.

Catalyst	Hz	min	wt.% Ni	wt.% Ru	$X_{CH_4}^{500°C}$	$X_{CH_4}^{550°C}$	$X_{CH_4}^{600°C}$	$S_{H_2}^{600°C}$	$S_{CO}^{600\,°C}$	$S_{CO_2}^{600°C}$	$Y_{Syngas}^{600\,°C}$
Equilibrium	–	–	–	–	51.3	77.9	89.4	65.4	30	4.5	85.3
CeO_2	–	–	–	–	0	0	0	0	0	0	0
Ni/CeO_2/BM	50	15	0.5	–	10.8	22	25.9	0	0	100	0
Ni/CeO_2/IWI	–	–	0.5	–	8.6	18.6	28.3	0	0	100	0
Ni/CeO_2/BM	50	15	1	–	12.3	17	20.5	0	0	100	0
Ni/CeO_2/IWI	–	–	1	–	18.3	28.5	34.3	0	0	100	0
Ni/CeO_2/BM	50	15	1.5	–	20.5	30.3	38.5	0	0	100	0
Ni/CeO_2/IWI	–	–	1.5	–	13.6	31.2	34.3	0	0	100	0
Ru/CeO_2/BM	50	15	–	0.25	5.4	38.5	52.1	62.0	17.1	20.9	41.2
Ru/CeO_2/IWI	–	–	–	0.25	1.6	7.8	41.8	65.8	9.5	24.7	31.5
Ru/CeO_2/BM	50	15	–	0.5	9.9	54.5	62	65.0	22.6	12.4	54.3
Ru/CeO_2/IWI	–	–	–	0.5	11.9	24.3	61.8	66.5	15.1	18.4	50.3
Ru/CeO_2/BM	50	15	–	1	14.9	62	71.8	66.3	20	13.8	61.9
Ru/CeO_2/IWI	–	–	–	1	33.4	60.4	74.1	65.1	21.7	13.2	64.3

Under the reaction conditions tested in this work, the CeO_2 support in the absence of metals (Ru and Ni) is totally inactive for the POM process, even after milling. Moreover, the catalytic activity of the monometallic Ni/CeO_2 catalysts prepared by either IWI or BM methods showed low methane conversion and the formation of syngas was not observed. In contrast, the catalytic activity of Ru/CeO_2 was much

greater than that of Ni/CeO_2, irrespective of the preparation method employed. As an example, the methane conversion values for Ru/CeO_2 catalysts with 1 wt.% of Ru prepared by either IWI or BM methods at 600 °C are between 70–75%, which is more than double of those obtained over Ni/CeO_2 catalysts with 1 wt.% of Ni (20–35%). Moreover, it is clear that the catalytic activity of monometallic Ru/CeO_2 catalysts increased with increasing the wt. % of Ru, as the CH_4 conversion values for Ru/CeO_2 catalysts with 1 wt. % Ru prepared either by IWI and BM methods at 600 °C are ~70 %, around 10 % higher than those of the monometallic 0.5Ru/CeO_2 catalysts, and 20 % higher than monometallic 0.25Ru/CeO_2 samples.

Table–5.3. Methane conversion, hydrogen, carbon monoxide, and carbon dioxide selectivity values, and syngas yield obtained over bimetallic Ru–Ni/CeO_2 catalysts prepared incipient wetness impregnation (IWI). Metal loading values are nominal. Reaction conditions: CH_4:air:N_2= 4:11:85, F/W= 60 L h^{-1} g^{-1}, GHSV=12 × 10^3 h^{-1}.

Catalyst	wt.% Ni	wt.% Ru	$X_{CH_4}^{500°C}$	$X_{CH_4}^{550°C}$	$X_{CH_4}^{600°C}$	$S_{H_2}^{600°C}$	$S_{CO}^{600\,°C}$	$S_{CO_2}^{600°C}$	$Y_{Syngas}^{600\,°C}$
Ru–Ni/CeO_2/IWI	0.5	1	37.3	74.1	84.5	67.2	27.1	5.7	79.7
Ni–CeO_2/IWI/Ru/IWI	0.5	1	13	70.6	81.7	66.9	25.9	7.2	75.8
Ru–CeO_2/IWI/Ni/IWI	0.5	1	13.1	72.9	84.8	67.6	26.5	6	79.7
Ru–Ni/CeO_2/IWI	0.75	0.75	14.4	72.6	83.4	67	26.5	6.6	78
Ru–Ni/CeO_2/IWI	1	0.5	7.9	65.1	77.8	66.7	26.4	6.9	72.4
Ru–Ni/CeO_2/IWI	1.25	0.25	8.3	63.3	75.5	66.9	24.8	8.4	69.2
Ru–Ni/CeO_2/IWI	1.38	0.12	7.9	63.2	76.5	66.9	25.6	7.5	70.7
Ru–Ni/CeO_2/IWI	1.44	0.06	5.5	56.4	76.4	63.7	20.6	15.8	64.3

Table–5.4. Methane conversion, hydrogen, carbon monoxide, and carbon dioxide selectivity values, and syngas yield obtained over bimetallic Ru–Ni/CeO_2 catalysts prepared by ball milling (BM). Metal loading values are nominal. Reaction conditions: CH_4:air:N_2= 4:11:85, F/W=60 L h^{-1} g^{-1}, GHSV=12 × 10^3 h^{-1}.

Catalyst	Hz	min	wt.% Ni	wt.% Ru	$X_{CH_4}^{500°C}$	$X_{CH_4}^{550°C}$	$X_{CH_4}^{600°C}$	$S_{H_2}^{600°C}$	$S_{CO}^{600\,°C}$	$S_{CO_2}^{600°C}$	$Y_{Syngas}^{600\,°C}$
Ru–Ni/CeO_2/BM	50	10	0.5	1	56.8	72.6	80.9	66.8	26.7	6.5	75.3
Ni–CeO_2/BM/Ru/BM	50	10	0.5	1	14.4	72.8	85.1	67	28.1	4.9	80.9
Ru–CeO_2/BM/Ni/BM	50	10	0.5	1	54.6	69	82	66.7	26.7	26.7	76.6
Ru–Ni/CeO_2/BM	50	5	0.5	1	52.7	70.7	78.2	66.4	25.7	7.9	72
Ru–Ni/CeO_2/BM	50	15	0.5	1	59	72.6	84.7	67.0	27.8	5.2	80.3
Ru–Ni/CeO_2/BM	50	20	0.5	1	50.4	69.3	81.6	70.3	21.4	8.3	74.8
Ru–Ni/CeO_2/BM	50	40	0.5	1	55.8	71.7	75.6	66.1	24.8	9.1	68.8
Ru–Ni/CeO_2/BM	15	15	0.5	1	7.8	64.1	79.1	66.7	26.9	6.4	74
Ru–Ni/CeO_2/BM	30	15	0.5	1	14.9	69.8	82.1	67	27.5	5.5	77.6
Ru–Ni/CeO_2/BM	50	15	0.75	0.75	50.6	66.3	80	66.8	24.9	8.3	73.3
Ru–Ni/CeO_2/BM	50	15	1	0.5	56.6	61.3	75.8	66.1	23.8	10.1	68.1
Ru–Ni/CeO_2/BM	50	15	1.25	0.25	54	62.9	76.2	66.9	24.9	8.1	70.3
Ru–Ni/CeO_2/BM	50	15	1.38	0.12	50.9	63	77	67	24.8	8.2	70
Ru–Ni/CeO_2/BM	50	15	1.44	0.06	48.3	53.9	68.1	66.3	22.7	11	60.6

It is evident from the data compiled in Table–5.3 and Table–5.4 that the synergistic effect of Ru and Ni in the bimetallic catalysts is noteworthy, leading to a significant enhancement in both CH_4 conversion and syngas production compared to the monometallic catalysts. The IWI–prepared bimetallic Ru–Ni/CeO_2 catalysts (Table–5.3) exhibited methane conversion levels ranging from 75% to 85%. These catalysts demonstrated a selectivity towards H_2 of 66% to 68%, selectivity towards CO of 25% to 28%, and syngas yield ranging between 69% and 80%. Furthermore,

the bimetallic Ru–Ni/CeO_2 catalysts prepared via BM exhibited impressive CH_4 conversion rates ranging from 76% to 85% at 600 °C (Table–5.4). Additionally, these catalysts displayed a hydrogen selectivity of 66% to 70%, CO selectivity of 22% to 28%, and syngas yield ranging between 68% and 80%. These values closely resemble those predicted by thermodynamic equilibrium [22]. Notably, these values surpassed those obtained from the Ni/CeO_2 and Ru/CeO_2 catalysts (Table–5.2). This outcome clearly illustrates that the synergy between Ru and Ni on CeO_2 leads to catalysts with enhanced activity and selectivity for the POM, surpassing the performance of their monometallic counterparts.

Fig–5.5 illustrates the effect of metal addition (one–step ball milling or co–IWI vs. two-step ball milling or sequential–IWI) and milling conditions (time and frequency), for the catalysts synthesized through mechanochemistry, on methane conversion. In Fig–5.5a, the methane conversion of bimetallic 1Ru–0.5Ni/CeO_2 catalysts prepared by co–impregnation (1Ru–0.5Ni/CeO_2/IWI) and sequential impregnation, either by impregnating Ni first and then Ru (0.5Ni–CeO_2/IWI/1Ru/IWI) or by impregnating Ru first and then Ni (1Ru–CeO_2/IWI/0.5Ni/IWI), is shown. It is observed that while similar methane conversion values are obtained for the co–IWI and sequential–IWI catalysts at higher reaction temperature (600 °C), the co–IWI catalyst exhibits higher activity at lower temperature (500 °C). On the other hand, Fig–5.5b displays the methane conversion results for the bimetallic 1Ru–0.5Ni/CeO_2 catalysts prepared using one–step ball milling (1Ru–0.5Ni/CeO_2/BM) and two–step ball milling, either by adding Ni first and then Ru (0.5Ni–CeO_2/BM/1Ru/BM) or by adding Ru first and then Ni (1Ru–CeO_2/BM/0.5Ni/BM). Again, at higher reaction temperatures (550–600 °C), similar methane conversion values are obtained regardless of the order of metal addition.

However, it is worth highlighting that both the bimetallic 1Ru–0.5Ni/CeO_2/BM and 1Ru–CeO_2/BM/0.5Ni/BM catalysts exhibit significantly higher catalytic activity at lower temperature (500 °C).

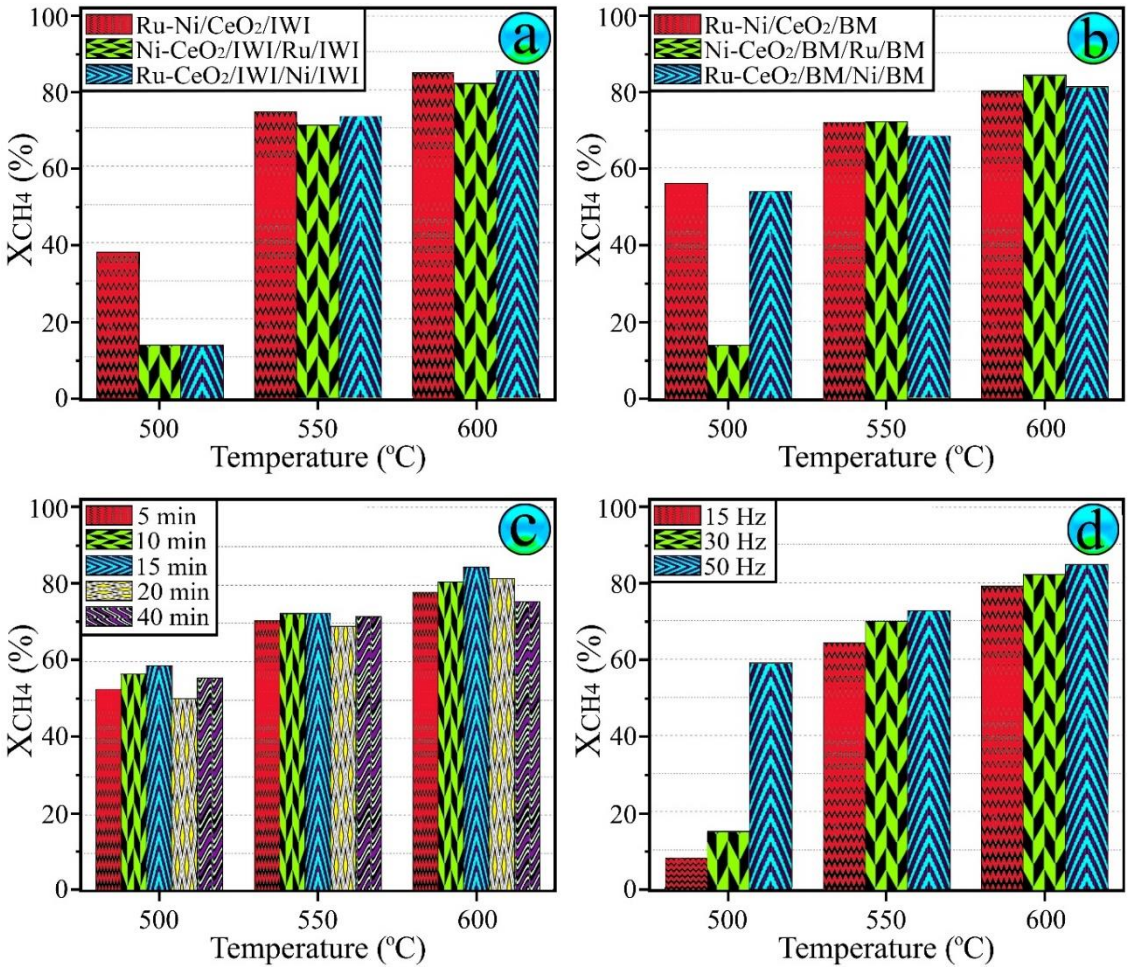

Fig-5. 5: Conversion of methane at 500–600 °C of bimetallic 1Ru–0.5Ni/CeO_2 catalysts prepared by co–IWI and sequential–IWI (a) and co–BM and sequential–BM at 50 Hz for 10 min (b). Conversion of methane at 500-600 °C of 1Ru–0.5Ni/CeO_2 catalysts prepared with different milling times at 5 to 40 min (c) and different milling frequencies at 15 to 50 Hz (d). Reaction conditions: CH_4:air:N_2= 4:11:85, F/W= 60 L h^{-1} g^{-1}, GHSV=12 × 10^3 h^{-1}.

This observation suggests that the mechanical forces between the three catalyst components (ceria, Ni, and Ru) generate different surface architectures, obtaining exceptional high activity when Ru and CeO_2 are put in contact first. The methane

conversion values shown in Fig–5.5a and 5b confirm that, in all cases, the catalytic activity at low temperature (500 °C) of the samples prepared by ball milling consistently surpasses that of the corresponding counterparts prepared by incipient wetness impregnation.

The effect of ball milling parameters on catalytic activity for the 1Ru–0.5Ni/CeO_2/BM catalyst is shown in Fig–5.5c and 5d (selectivity and syngas yield values can be found in Table–5.4). At low reaction temperature, the milling frequency has a significant influence on methane conversion. Overall, the optimal synthesis conditions for catalysts produced via ball milling are a frequency of 50 Hz and a milling time of 15 minutes.

Considering the significantly higher cost of Ru compared to Ni, we conducted a study to examine the influence of the Ru:Ni ratio in bimetallic catalysts on the POM catalytic performance. Fig–5.6 illustrates the methane conversion and syngas yield at 500 and 600 °C for the bimetallic xRu–yNi/CeO_2 catalysts prepared using both IWI and BM methods, with varying amounts of Ru (ranging from 0.06 to 1 wt.%) and Ni (ranging from 0.5 to 1.44 wt.%), while maintaining a total metal loading of 1.5 wt.%. Clearly, the Ru:Ni ratio exhibits a noticeable influence on both CH_4 conversion and syngas selectivity, particularly at low temperature (500 °C). A correlation between the Ru content in the bimetallic samples and the catalytic activity is observed: the higher the Ru content the higher the methane conversion and selectivity towards syngas. Also, in all cases, the methane conversion and syngas selectivity values obtained at low temperature were significantly higher for the BM samples compared to the catalysts prepared using the IWI method. It is interesting to highlight that neither the monometallic Ru/CeO_2 catalysts prepared by IWI nor BM methods

demonstrated syngas production at temperatures below 550 °C. Therefore, the strong synergistic effect between Ru and Ni facilitates the formation of syngas at low temperatures, even with low Ru contents.

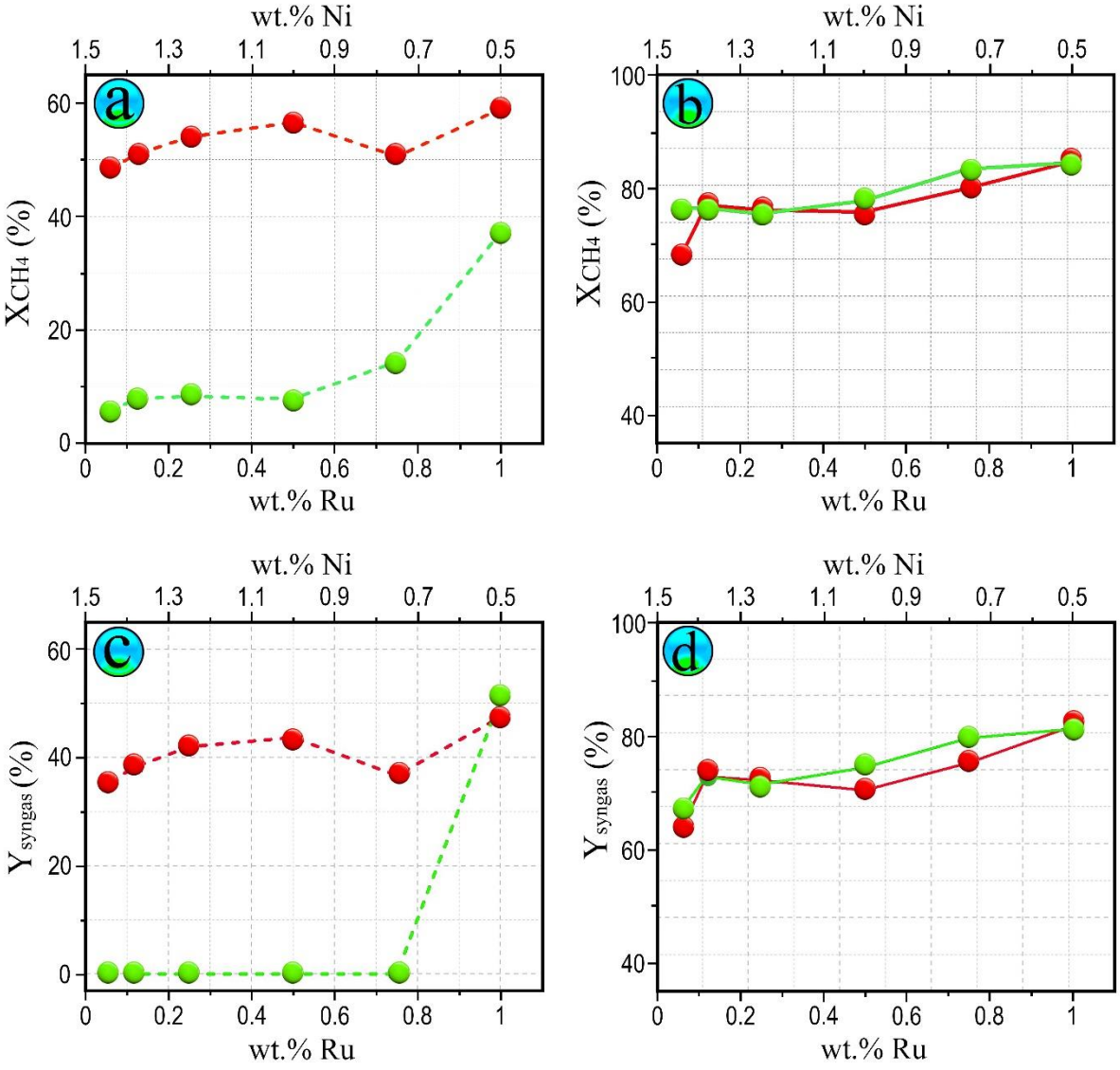

Fig-5. 6: Methane conversion at 500°C (a) and 600 °C (b), and syngas yield at 500 °C (c) and 600 °C (d) for the bimetallic catalysts xRu–yNi/CeO_2 prepared by BM (red), and IWI (green) methods. All bimetallic catalysts contain a nominal metal loading of 1.5 wt.%. Reaction conditions: GHSV=12 × 10^3 h^{-1} and F/W= 60 L h^{-1} g^{-1}. Ball mill conditions: 50 Hz for 15 min.

5.3 Characterization of the catalysts after reaction

Fig–5.7 displays the Raman spectra of the same samples depicted in Fig–5.1, but after the catalytic test. In comparison to the fresh catalysts, the position of the F_{2g} band of CeO_2 remained unchanged in all samples after the reaction, indicating that no metals were incorporated into the ceria structure during the tested conditions. In addition to the signals of RuO_x, the Raman spectra of the catalysts after reaction exhibited the distinctive D and G bands of graphitic carbon at approximately ~1343 and ~1590 cm^{-1}, respectively [23, 24]. As depicted in the zoomed-in area of the figure, carbon deposition was clearly more prominent on the monometallic samples, particularly those prepared using the IWI method. During the POM process, carbon deposition can occur through various side reactions, such as $CH_4 \rightarrow 2H_2+C$, $2CO \rightarrow C+CO_2$, and $CO+H_2 \rightarrow C+H_2O$ [26]. The bimetallic catalyst prepared by BM, 1Ru–0.5Ni/CeO_2/BM, demonstrated the lowest carbon accumulation.

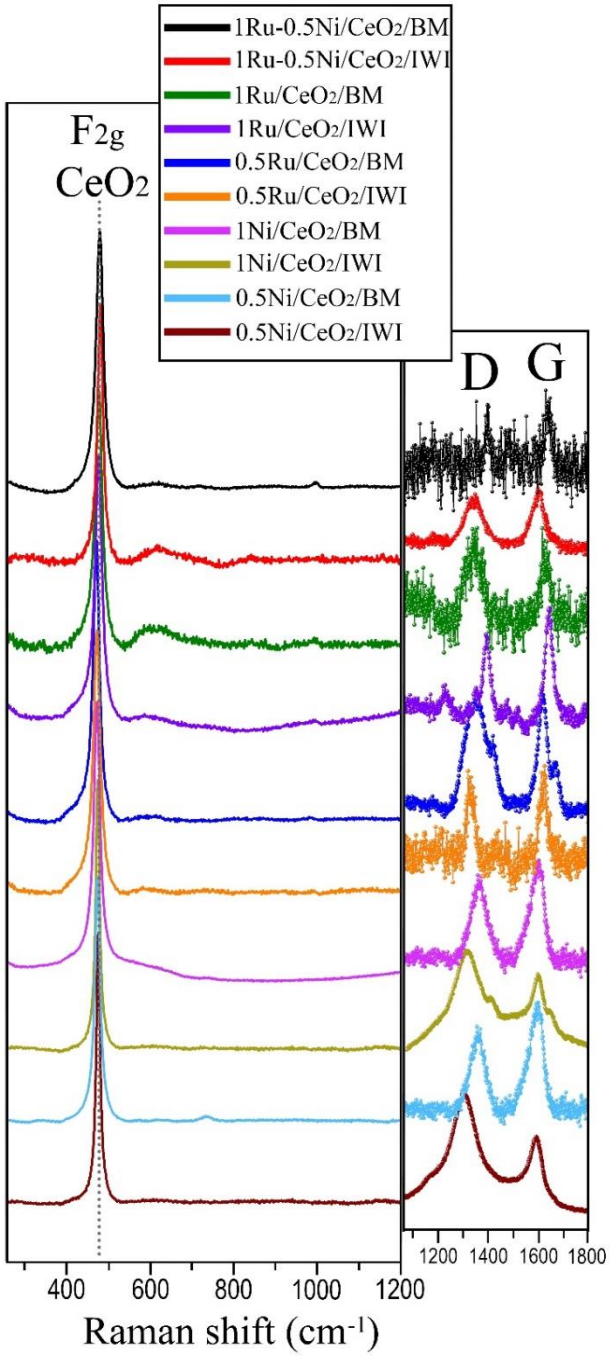

Fig-5. 7: Raman spectra of the monometallic catalysts 1Ru/CeO_2/BM, 1Ru/CeO_2/IWI, 0.5Ni/CeO_2/BM and 0.5Ni/CeO_2/IWI, and bimetallic catalysts 1Ru–0.5Ni/CeO_2/BM and 1Ru–0.5Ni/CeO_2/IWI after reaction at 600°C. Reaction conditions: CH_4:air:N_2= 4:11:85, F/W=60 L h^{-1} g^{-1}, GHSV=12 × 10^3 h^{-1}. Ball mill conditions: 30 Hz for 10 min.

5.4 Stability tests

The bimetallic catalysts 0.5Ru–1Ni/CeO_2/BM and 0.5Ru–1Ni/CeO_2/IWI were subjected for a long-term stability test at 550 °C for over 100 hours, along with the monometallic 0.5Ru/CeO_2/BM catalyst for comparison purposes. Figs–5. 8a and 8b show the methane conversion and syngas yield for the three samples, respectively. As expected from the previous results, the initial methane conversion of the Ru–Ni/CeO_2 bimetallic catalysts prepared by IWI (68%) and BM (73%) methods was significantly higher than that of the Ru monometallic catalyst (57%), and that the bimetallic catalyst prepared via the BM method exhibited higher methane conversion compared to the bimetallic counterpart prepared via the IWI method. During the first 50 hours on stream, both Ru–Ni bimetallic catalysts prepared by BM and IWI methods experienced a consistent decline in the CH_4 conversion rate at approximately 0.12% per hour. In contrast, the monometallic Ru–CeO_2/BM catalyst showed a considerably higher deactivation rate of approximately 0.29% per hour. After this period, the methane conversion stabilized on the bimetallic catalysts, while it continued to decrease on the Ru monometallic sample.

Following the long-term stability test, Raman spectra were recorded (Figs–5. 8c). The intensity of the D and G bands of carbon at approximately ~1347 and ~1603 cm^{-1}, respectively, exhibited an opposite trend to stability: 0.5Ru–CeO_2/BM >> 0.5Ru–1Ni/CeO_2/IWI > 0.5Ru–1Ni/CeO_2/BM. This suggests that the presence of carbon deposition can account for the deactivation of the catalysts during the stability test. The minimal carbon deposition observed on the bimetallic 0.5Ru–1Ni/CeO_2 catalyst prepared via the BM method is particularly noteworthy.

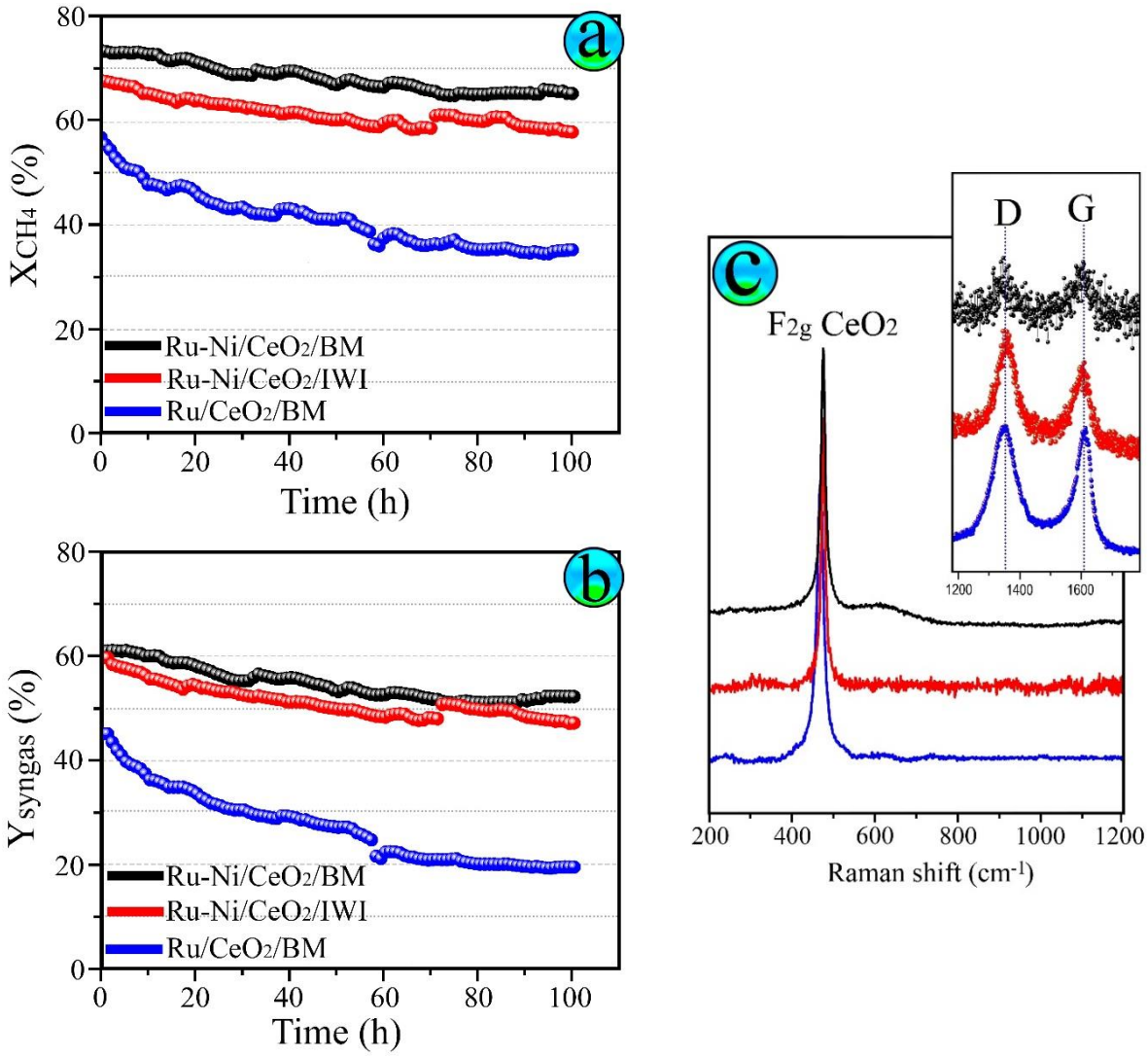

Fig-5. 8: Conversion of methane (a) and yield of syngas (b) in a long–term stability test at 550 °C on monometallic 0.5Ru/CeO_2/BM (red) catalyst, and bimetallic catalysts 0.5Ru–1Ni/CeO_2/BM (black) and 0.5Ru–1Ni/CeO_2/IWI (green). Raman spectra recorded for the samples after the long–term stability test (c). Reaction conditions: CH_4:air:N_2= 4:11:85, F/W=60 L h^{-1} g^{-1}, GHSV=12×10^3 h^{-1}. Ball mill conditions: 30 Hz for 10 min.

5.5 Conclusions

This study involved the preparation of series of monometallic Ru and Ni catalysts, as well as bimetallic Ru–Ni catalysts supported on CeO_2, using both ball milling (BM) and incipient wetness impregnation (IWI) methods. The catalysts were characterized using Raman and X–ray photoelectron spectroscopy and H_2–TPR, and tested for the production of syngas through the POM reaction at atmospheric pressure at low temperature (350 to 600 °C). The catalytic results clearly demonstrated that bimetallic Ru–Ni catalysts exhibited superior activity and selectivity compared to monometallic Ru and Ni samples. The CH_4 conversion and syngas yield observed for various catalysts followed the trend: Ru–Ni/CeO_2/BM ≥ Ru–Ni/CeO_2/IWI >> Ru/CeO_2/BM ≥ Ru/CeO_2/IWI >> Ni/CeO_2/BM ≈ Ni/CeO_2/IWI ≈ CeO_2. Notably, a remarkable synergy between Ru and Ni on CeO_2 was observed in the bimetallic samples prepared via BM, resulting in significantly more active POM active sites, particularly at temperatures below 550 °C, and stable catalyst performance, which was related to the absence of carbon deposition on the catalyst surface.

5.6 References

1. Wu, Z., et al., Probing defect sites on CeO_2 nanocrystals with well-defined surface planes by Raman spectroscopy and O_2 adsorption. Langmuir, 2010. **26**(21): p. 16595-16606.
2. Reddy, B.M., et al., Surface characterization of CeO_2/SiO_2 and $V_2O_5/CeO_2/SiO_2$ catalysts by Raman, XPS, and other techniques. The Journal of Physical Chemistry B, 2002. **106**(42): p. 10964-10972.
3. Reddy, B.M., B. Manohar, and E.P. Reddy, Oxygen chemisorption on titania-zirconia mixed oxide supported vanadium oxide catalysts. Langmuir, 1993. **9**(7): p. 1781-1785.
4. Weber, W., K. Hass, and J. McBride, Raman study of CeO_2: Second-order scattering, lattice dynamics, and particle-size effects. Physical Review B, 1993. **48**(1): p. 178.
5. Carter, J.C., et al., Raman spectroscopic evidence supporting the existence of Ni_4 (OH) 44+ in aqueous, Ni $(NO_3)_2$ solutions. Analytica Chimica Acta, 2004. **514**(2): p. 241-245.
6. Lucentini, I., et al., Ammonia decomposition over 3D-printed CeO_2 structures loaded with Ni. Applied Catalysis A: General, 2020. **591**: p. 117382.
7. Huang, H., Q. Dai, and X. Wang, Morphology effect of Ru/CeO_2 catalysts for the catalytic combustion of chlorobenzene. Applied Catalysis B: Environmental, 2014. **158**: p. 96-105.
8. Lucentini, I., et al., Catalytic ammonia decomposition over Ni-Ru supported on CeO_2 for hydrogen production: Effect of metal loading and kinetic analysis. Applied Catalysis B: Environmental, 2021. **286**: p. 119896.

9. Mar, S., et al., Characterization of RuO_2 thin films by Raman spectroscopy. Applied Surface Science, 1995. **90**(4): p. 497-504.
10. Watanabe, S., X. Ma, and C. Song, Characterization of structural and surface properties of nanocrystalline TiO_2−CeO_2 mixed oxides by XRD, XPS, TPR, and TPD. The Journal of Physical Chemistry C, 2009. **113**(32): p. 14249-14257.
11. Dou, Y., et al., Core-shell structured Ru-Ni@ SiO_2: Active for partial oxidation of methane with tunable H_2/CO ratio. Journal of Energy Chemistry, 2018. **27**(3): p. 883-889.
12. Zheng, W., et al., Effects of CeO_2 addition on Ni/Al_2O_3 catalysts for the reaction of ammonia decomposition to hydrogen. Applied Catalysis B: Environmental, 2008. **80**(1-2): p. 98-105.
13. Pérez-Bustos, H.F., et al., Synthesis and characterization of bimetallic catalysts Pd-Ru and Pt-Ru supported on γ-alumina and zeolite FAU for the catalytic transformation of HMF. Fuel, 2019. **239**: p. 191-201.
14. Pang, J., et al., Mesoporous Cu_2O–CeO_2 composite nanospheres with enhanced catalytic activity for 4-nitrophenol reduction. Applied Surface Science, 2018. **439**: p. 420-429.
15. Molinari, M., et al., Water adsorption and its effect on the stability of low index stoichiometric and reduced surfaces of ceria. The Journal of Physical Chemistry C, 2012. **116**(12): p. 7073-7082.
16. Jones, R.H., et al., Catalytic conversion of methane to synthesis gas over europium iridate, $Eu_2Ir_2O_7$: Anin situ study by x-ray diffraction and mass spectrometry. Catalysis Letters, 1991. **8**(2): p. 169-174.
17. Claridge, J.B., et al., A study of carbon deposition on catalysts during the partial oxidation of methane to synthesis gas. Catalysis Letters, 1993. **22**(4): p. 299-305.

18. Vernon, P.D., et al., Partial oxidation of methane to synthesis gas. Catalysis Letters, 1990. **6**(2): p. 181-186.
19. Ashcroft, A., A.K. Cheetham, and M. Green, Partial oxidation of methane to synthesis gas using carbon dioxide. Nature, 1991. **352**(6332): p. 225-226.
20. Ashcroft, A., et al., Selective oxidation of methane to synthesis gas using transition metal catalysts. Nature, 1990. **344**(6264): p. 319-321.
21. Fazlikeshteli, S., X. Vendrell, and J. Llorca, Low-temperature partial oxidation of methane over Pd–Ni bimetallic catalysts supported on CeO2. International Journal of Hydrogen Energy, 2023. **48**(32): p. 12024-12035.
22. Dandy, D. Bioanalytical Microfluidics Program. 2019; Available from: https://navier.engr.colostate.edu/code/code-4/index.html.
23. Han, Z., et al., Propane dehydrogenation over Pt–Cu bimetallic catalysts: the nature of coke deposition and the role of copper. Nanoscale, 2014. **6**(17): p. 10000-10008.
24. Chen, Y. and J. Chen, Selective hydrogenation of acetylene on SiO_2 supported Ni-In bimetallic catalysts: Promotional effect of In. Applied Surface Science, 2016. **387**: p. 16-27.

CHAPTER 6

6. Bimetallic Ru–Pd supported on CeO_2 for the catalytic partial oxidation of methane into syngas

The data used in this chapter has been partially published in:

I. S. Fazlikeshteli, J. Llorca, X. Vendrell. Fuel 334: 126799.
https://doi.org/10.1016/j.fuel.2022.126799

Abstract

In the last chapter, a series of monometallic Ru, Pd, and bimetallic Ru–Pd catalysts loaded on CeO_2 support have been prepared via BM and IWI methods and used in the POM process to produce syngas. The preparation of the monometallic xRu/CeO_2, yPd/CeO_2 and bimetallic $xRu–yPd/CeO_2$ catalysts have been described in Chapter 2. As in the previous chapters, at first, we discussed about the characterization of the fresh samples by Raman spectroscopy, Temperature programmed reduction (H_2–TPR), and X–ray photoelectron spectroscopy (XPS). Then, we concentrated on the influence of the preparation method, the sequence in which the metals are added, the milling energy and time for samples prepared by the mechanochemical method, and the Ru:Pd metal ratio which have been evaluated for the POM between 300–600 °C. At the end, Raman spectroscopy, and high–resolution transmission electron microscopy (HRTEM) were investigated to characterize the catalysts after reaction and the most importantly the long stability test result that obtained by the best bimetallic $Ru–Pd/CeO_2$ catalysts.

6.1 Characterization of fresh catalysts

6.1.1 Raman spectroscopy

Fig–6.1 displays the Raman spectra for fresh monometallic Ru, Pd, and bimetallic Ru–Pd catalysts supported on CeO_2 prepared by BM and IWI methods. Similar to previous chapters, various spectra were recorded for each sample at several locations and no differences were noted, indicating homogeneity of the samples. The Raman spectra were dominated by the characteristic F_{2g} band of the ceria lattice structure at ~460 cm^{-1} [157]. In addition, the defect-induced vibrational mode at about ~595 cm^{-1} (D band) of ceria lattice defects, such as oxygen vacancies, was nearly absent in all catalysts, which suggested that the incorporation of Pd and Ru did not result in the formation of lattice defects in the ceria structure [158].

The Raman spectra of the monometallic 1Pd/CeO_2 catalysts prepared either by IWI and BM methods and bimetallic 0.5Ru–CeO_2/IWI/1Pd/IWI catalyst showed a band at ~650 cm^{-1}, which correspond to the B_{1g} mode of PdO and suggests that these samples contain well-defined PdO nanoparticles [161]. Moreover, for the catalysts containing Pd and prepared by mechanochemistry (1Pd/CeO_2/BM and 0.5Ru–CeO_2/BM/1Pd/BM), a weak band was observed at ~1050 cm^{-1}, which is ascribed to the symmetric ν_1 stretching mode of the nitrate anion [174]. For the catalysts prepared by the IWI method the NO_3^- band was absent, because nitrate residues disappeared following the calcination treatment performed at 650 °C. Additionally, for the monometallic 0.5Ru/CeO_2 catalyst prepared by IWI method a broadband at about 645–700 cm^{-1} is found, which is attributed to the B_{2g} mode of RuO_2 [193].

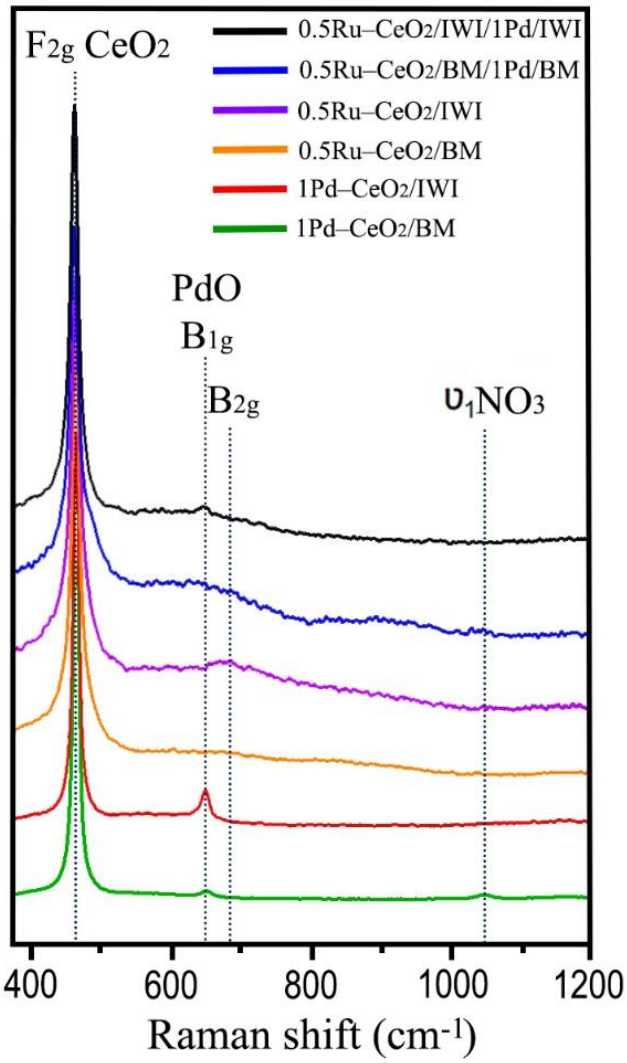

Fig-6. 1: Raman spectra of 1Pd/CeO_2 and 0.5Ru/CeO_2 samples prepared by BM and IWI methods, and bimetallic catalysts 0.5Ru–CeO_2/BM/1Pd/BM and 0.5Ru–CeO_2/IWI/1Pd/IWI. Ball mill conditions: 30 Hz and 10 min.

6.1.2 Temperature programmed reduction (H_2–TPR)

H_2–TPR profiles are shown in Fig–6.2. As already discussed in previous chapters, the profile of the CeO_2 support presents two peaks at around 530 and 780 °C, corresponding to the surface reduction of ceria and the reduction of bulk Ce(IV) to Ce(III), respectively [193]. The bulk reduction peak of CeO_2 were detected in all the other samples analyzed, and it is quite clear, compared with monometallic Pd/CeO_2 catalysts prepared by both BM and IWI methods, that the bulk CeO_2 reduction peak for the bimetallic Ru–Pd catalysts are shifted to lower temperatures, which reveals that the simultaneous presence of Ru and Pd exerts a strong influence on the CeO_2

reduction. Generally, the reduction profile of pure PdO is reported typically between 20 and 100 °C [181, 199]. The reduction profile of the monometallic Pd/CeO_2 catalyst prepared by BM exhibits two H_2 consumption peaks at about 150 and 293 °C. The reduction peak at ~150 °C is attributable to the reduction of surface PdO [200], while the intense consumption at ~293°C can be assigned to the reduction of PdO–CeO_2 species strongly interacting with each other [201].

In contrast, the monometallic Pd/CeO_2 catalyst prepared by IWI did not show significant hydrogen consumption at low temperature. This represents a remarkable difference between the two Pd/CeO_2 catalyst and indicates that mechanochemistry originates a catalyst containing a strong interaction between Pd and CeO_2 [202]. Three reduction peaks were observed for the monometallic Ru/CeO_2 and bimetallic Ru–Pd/CeO_2 catalysts prepared by both IWI and BM methods in the range of 100–380 °C. According to literature data, the reduction peaks between 100 and 150 °C correspond to the reduction of RuO_x–type oxides (e.g. Ru_2O_3) different from RuO_2 [197], while the peaks at 210–380 °C are assigned to the reduction of well-dispersed ruthenium oxide particles on the surface of the ceria support [197].

Interestingly, the hydrogen consumption for the bimetallic Ru–Pd/CeO_2 catalyst prepared by ball milling is much higher than that of the bimetallic sample prepared by incipient wetness impregnation, particularly at low temperature. This again points out to a particular strong interaction between Pd and Ru and between the metals and the ceria support.

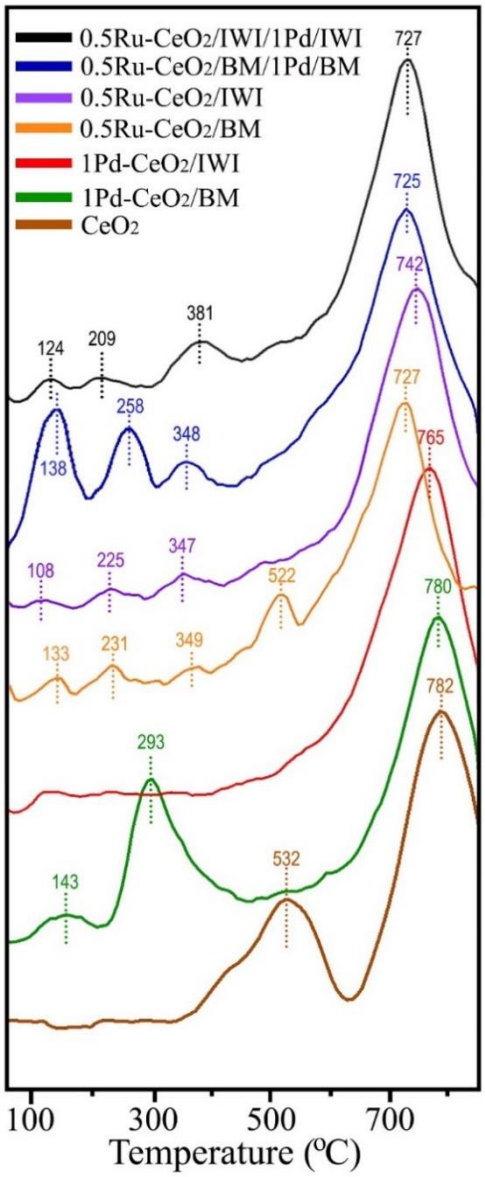

Fig-6. 2: H_2–TPR results of CeO_2, 1Pd/CeO_2 and 0.5Ru/CeO_2 samples prepared by BM and IWI methods, and bimetallic catalysts 0.5Ru–CeO_2/BM/1Pd/BM and 0.5Ru–CeO_2/IWI/1Pd/IWI. Ball milling conditions: 30 Hz and 10 min.

6.1.3 X–ray Photoelectron Spectroscopy (XPS)

As shown in Fig–6.3, X–ray photoelectron spectroscopy (XPS) was used to determine the surface atomic composition of monometallic 1Pd/CeO_2, prepared by BM and IWI methods, and bimetallic 0.5Ru–CeO_2/BM/1Pd/BM and 0.5Ru–CeO_2/IWI/1Pd/IWI catalysts. Ru could not be identified on the surface of the bimetallic catalysts because of the low amount of ruthenium (≤ 0.5 wt. %). Fig–6.3a displays the Ce 3d spectra, and no significant changes are observed for all the catalysts. As discussed in the previous chapters, the fitted components labeled V and

U arise from the spin-orbit coupling of $3d_{5/2}$ and $3d_{3/2}$, respectively. Three doublets are attributed to the presence of Ce^{+4}: v (~882.7 eV), v_2 (~889 eV), v_3 (~898.3 eV), u (~900.9 eV), u_2 (~907.6 eV), and u_3 (~916.9 eV) [183]. Two doublets are ascribed to the presence of Ce^{3+}: v_0 (~880.5 eV), v_1 (~885.6 eV), u_0 (~889.2 eV), and u_1 (~903.8 eV) [203]. The analysis of the Ce 3d signals revealed that for all monometallic and bimetallic catalysts the percentage of Ce^{4+} species calculated as $Ce^{4+}/(Ce^{4+}+ Ce^{3+})$ is, in all cases, higher than 78%.

The Pd 3d core level XPS spectra for all samples were composed of two main doublets (Fig–6.3b), indicating that there are two different Pd species present on the surface [203]. There are two bands at about 336.3 and 337.9 eV for the Pd $3d_{5/2}$ spectra, which correspond to Pd^{2+} and Pd–O–Ce species, respectively [156]. Similarly, the Pd $3d_{3/2}$ spectra contain two bands related to Pd^{2+} (~341.5 eV) and Pd–O–Ce (~343.2 eV) species [90]. Interestingly, the Pd 3d core level XPS spectra reveal distinct differences between the monometallic and bimetallic catalysts, where the intensity of Pd–O–Ce species in the bimetallic Ru–Pd/CeO_2 catalysts is greater when compared to monometallic Pd/CeO_2 catalysts, independently of the preparation method. The surface atomic ratio calculated by $\left(\frac{Pd-O-Ce}{Pd-O-Ce + Pd^{2+}}\right)$ for these samples are: 1Pd/CeO_2/BM (= 0.63), 1Pd/CeO_2/IWI (= 0.49), 0.5Ru–CeO_2/BM/1Pd/BM (= 0.89), and 0.5Ru–CeO_2/IWI/1Pd/IWI (= 0.75). Therefore, it is claimed that that Pd species strongly interacting with ceria (Pd–O–Ce) are easily accommodated on the surface of bimetallic Ru–Pd/CeO_2 catalysts.

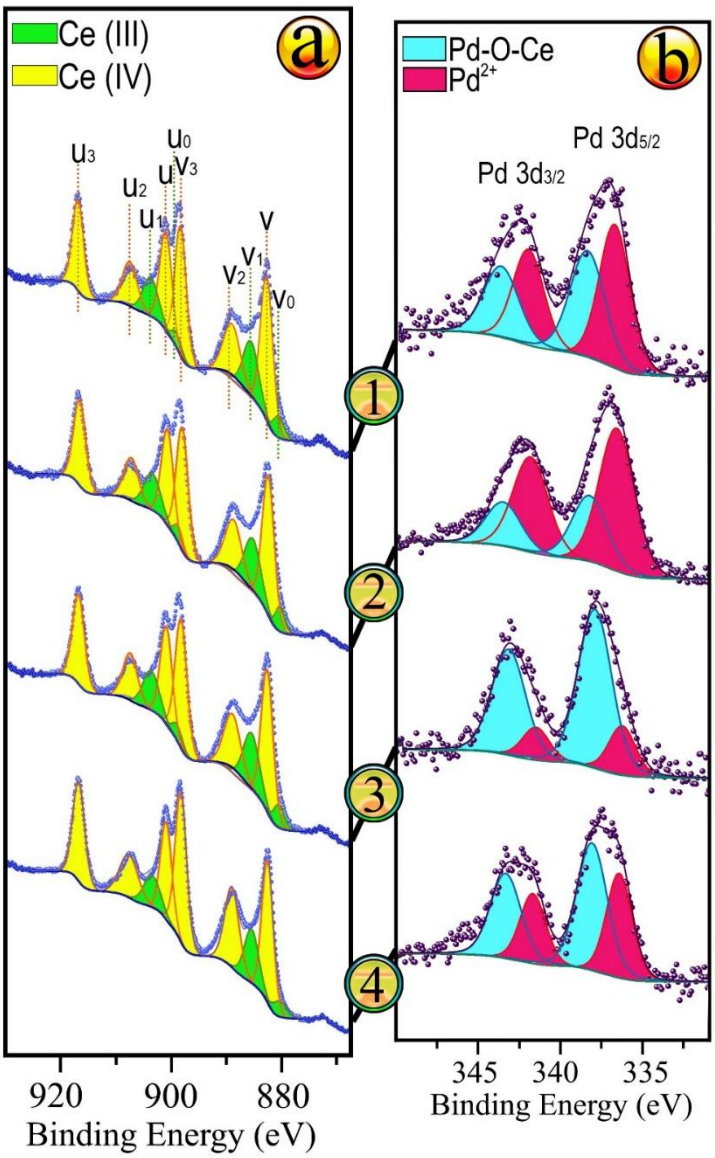

Fig-6. 3: Ce 3d (a) and Pd 3d (b) X–ray photoelectron spectra of monometallic 1Pd/CeO_2 catalysts prepared by BM (1) and IWI (2) methods, and bimetallic 0.5Ru–CeO_2/BM/1Pd/BM (3) and 0.5Ru–CeO_2/IWI/1Pd/IWI (4) catalysts. Ball mill conditions: 30 Hz and 10 min.

6.2 Catalytic tests

Fig–6.4 shows the molar flow rates of reactants (methane and oxygen) and products (hydrogen, carbon monoxide, water, and carbon dioxide) from 300 to 600 °C recorded on monometallic Ru, Pd, and bimetallic Ru–Pd catalysts supported on CeO_2 prepared by BM and IWI methods. According to thermodynamics, all samples followed similar trends in the disappearance of the reactants (CH_4 and O_2) and appearance of the products (H_2 and CO). As expected, CH_4 conversion increased with

increasing reaction temperature. In all cases, the distribution of intermediates and products is in accordance with the well–known combustion and reforming reaction (CRR) mechanism, where methane is first partially oxidized to yield H_2O and CO_2 and, as the temperature increases, the unreacted methane combines with H_2O and CO_2 to yield H_2 and CO through the steam reforming and dry reforming reactions (Eq–1.6 and Eq–1.7, respectively) [92, 165].

However, there is a significant difference between the Ru and Pd monometallic samples and the Ru–Pd bimetallic catalysts. Clearly, the bimetallic Ru–Pd catalysts exhibited higher catalytic activity and better syngas selectivity compared to monometallic Ru and Pd samples under the same operation conditions, pointing out to a beneficial effect of the synergy between the two metals. On the other hand, it should be noted that for all samples prepared by the IWI method the production of syngas occurred at higher temperature with respect to the samples prepared by the BM method. Considering the H_2–TPR and XPS results discussed above, it can be concluded that the strong interaction between Pd, Ru and CeO_2 that takes place in the catalysts prepared by ball milling with respect to those prepared by the conventional IWI method is responsible for a better catalytic performance.

Taking account these results, we prepared a series of monometallic and bimetallic catalysts varying the metal loading, the order of incorporation of metals and, for those samples prepared by mechanochemistry, the milling conditions (frequency and time) and the Pd:Ru elemental ratio. Tables–6. 1, 2 and 3 compile the catalytic results for all the samples at 450–600 °C in terms of methane conversion (x_{CH_4}), H_2 selectivity (S_{H_2}), CO selectivity (S_{CO}), and yield of syngas (Y_{sg}). Similar to previous

chapters, chemical equilibrium values and catalytic results of milled CeO_2 are also included for comparison.

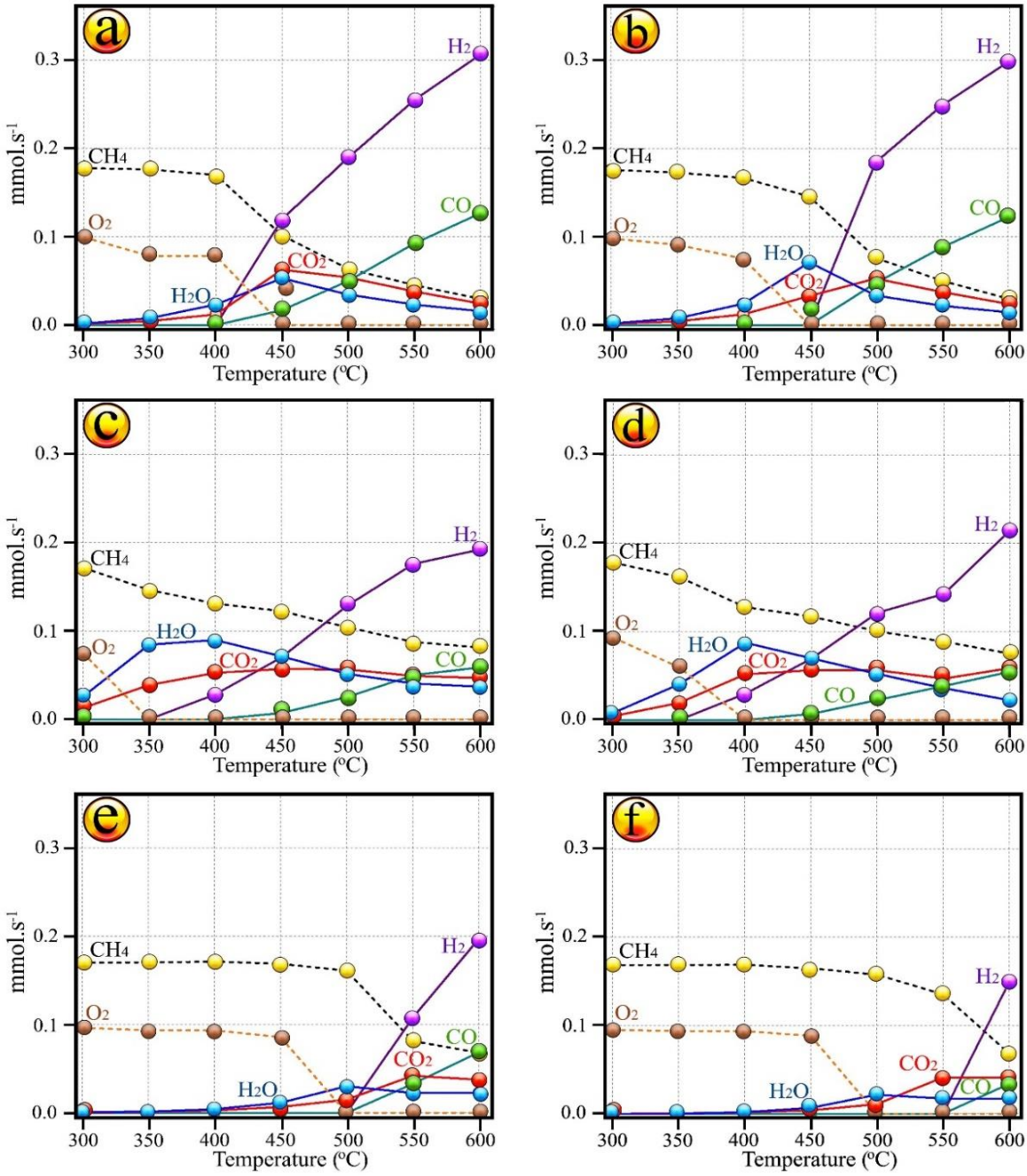

Fig-6. 4: Molar flows of bimetallic catalysts 0.5Ru–CeO_2/BM/1Pd/BM (a), 0.5Ru–CeO_2/IWI/1Pd/IWI (b), and monometallic 1Pd/CeO_2/BM (c), 1Pd/CeO_2/IWI (d), 0.5Ru/CeO_2/BM (e) and 0.5Ru/CeO_2/IWI (f) catalysts. GHSV=12 × 10^3 h^{-1}, F/W=60 L h^{-1} g^{-1}. Ball mill conditions: 30 Hz and 10 min.

Table–6.1. Methane conversion, hydrogen, carbon monoxide, and carbon dioxide selectivity values, and syngas yield obtained over milled CeO_2 and monometallic Ru/CeO_2 and Pd/CeO_2 samples prepared by ball milling (BM) and incipient wetness impregnation (IWI). Metal loading values are nominal. Reaction conditions: CH_4:air:N_2= 4:11:85, F/W= 60 L h^{-1} g^{-1}, GHSV=12 × 10^3 h^{-1}.

Catalyst	Hz	min	wt.% Pd	wt.% Ru	$X_{CH_4}^{450\,°C}$	$X_{CH_4}^{550\,°C}$	$X_{CH_4}^{600\,°C}$	$S_{H_2}^{600\,°C}$	$S_{CO}^{600\,°C}$	$S_{CO_2}^{600\,°C}$	$Y_{Syngas}^{600\,°C}$
Equilibrium	–	–	–	–	51.3	77.9	89.4	65.4	30	4.5	85.3
CeO_2	–	–	0	0	0	0	0	0	0	100	0
Ru/CeO_2/BM	30	10	0	0.25	5.4	38.5	52.1	62.0	17.1	20.9	41.2
Ru/CeO_2/IWI	–	–	0	0.25	1.9	7.8	41.8	65.8	9.5	24.7	31.5
Ru/CeO_2/BM	30	10	0	0.5	5.6	54.5	62	65.0	22.6	12.4	54.3
Ru/CeO_2/IWI	–	–	0	0.5	7.8	24.3	61.8	66.5	15.1	18.4	50.5
Ru/CeO_2/BM	30	10	0	1	10.9	62	71.8	66.3	20	13.8	61.9
Ru/CeO_2/IWI	–	–	0	1	16.3	60.4	74.1	65.1	21.7	13.2	64.3
Pd/CeO_2/BM	30	10	0.5	0	32.6	52.7	51.6	62.9	17.9	19.2	41.7
Pd/CeO_2/IWI	–	–	0.5	0	39.7	51.0	55.2	64.8	23.9	11.3	49.0
Pd/CeO_2/BM	30	10	1	0	31.5	51.0	54.6	64.6	19.7	15.7	46.0
Pd/CeO_2/IWI	–	–	1	0	34.5	50.3	58.0	65.4	16.6	17.9	47.6
Pd/CeO_2/BM	30	10	2	0	39.9	66.8	68.2	64.3	24.2	11.5	60.2
Pd/CeO_2/IWI	–	–	2	0	32.8	56	64.2	64.6	23.3	12.1	56.4

As already discussed in previous chapters, the CeO_2 support in the absence of metals is inactive for the POM process under the reaction conditions tested. It is clear that the catalytic activity of monometallic Pd/CeO_2 is greater than that of Ru/CeO_2 at temperatures ≤ 500°C, as the CH_4 conversion values for Pd/CeO_2 catalysts with 0.5 wt.% Pd prepared either by BM or IWI methods at 450 °C is ~30 % higher than those of the $0.5Ru/CeO_2$ monometallic catalysts.

Table–6.2. Methane conversion, hydrogen, carbon monoxide, and carbon dioxide selectivity values, and syngas yield obtained over bimetallic Ru–Pd/CeO_2 catalysts prepared by ball milling. Metal loading values are nominal. Reaction conditions: CH_4:air:N_2= 4:11:85, F/W= 60 L h^{-1} g^{-1}, GHSV=12 × 10^3 h^{-1}.

Catalyst	Hz	min	wt.% Pd	wt.% Ru	$X_{CH_4}^{450\,°C}$	$X_{CH_4}^{550\,°C}$	$X_{CH_4}^{600\,°C}$	$S_{H_2}^{600\,°C}$	$S_{CO}^{600\,°C}$	$S_{CO_2}^{600\,°C}$	$Y_{Syngas}^{600\,°C}$
Ru–Pd/CeO_2/BM	50	10	1	0.5	4.9	72.6	83.2	66.5	26.7	6.8	77.5
Pd–CeO_2/BM/Ru/BM	50	10	1	0.5	10.3	74.1	83.1	66.5	27.0	6.4	77.8
Ru–CeO_2/BM/Pd/BM	50	10	1	0.5	38.6	74.5	84.4	66.6	27.1	6.3	79.0
Ru–CeO_2/BM/Pd/BM	15	10	1	0.5	38.7	69.7	79.3	66.5	26.8	6.8	73.9
Ru–CeO_2/BM/Pd/BM	30	10	1	0.5	43.3	74.7	83.5	67.0	27.7	5.3	79.1
Ru–CeO_2/BM/Pd/BM	30	5	1	0.5	39.9	70.6	82.6	66.8	28.0	5.2	78.3
Ru–CeO_2/BM/Pd/BM	30	20	1	0.5	38.8	69.6	81.0	66.7	27.2	6.1	76.1
Ru–CeO_2/BM/Pd/BM	30	10	0.5	1	42.5	71.8	82.6	66.9	27.5	5.6	78.0
Ru–CeO_2/BM/Pd/BM	30	10	0.75	0.75	41.8	72.0	81.8	66.9	27.4	5.7	77.2
Ru–CeO_2/BM/Pd/BM	30	10	1.25	0.25	46.7	72.7	81.6	66.6	24.9	8.6	74.6
Ru–CeO_2/BM/Pd/BM	30	10	1.38	0.12	41.8	67.2	81.6	66.7	27.0	6.2	76.5
Ru–CeO_2/BM/Pd/BM	30	10	1.44	0.06	41.7	65.3	78.7	66.4	26.1	7.6	72.7

Table–6.3. Methane conversion, hydrogen, carbon monoxide, and carbon dioxide selectivity values, and syngas yield obtained over bimetallic Ru–Pd/CeO_2 catalysts prepared by incipient wetness impregnation (IWI). Metal loading values are nominal. Reaction conditions: CH_4:air:N_2= 4:11:85, F/W= 60 L h^{-1} g^{-1}, GHSV=12 × 10^3 h^{-1}.

Catalyst	wt.% Pd	wt.% Ru	$X_{CH_4}^{450\,°C}$	$X_{CH_4}^{550\,°C}$	$X_{CH_4}^{600\,°C}$	$S_{H_2}^{600\,°C}$	$S_{CO}^{600\,°C}$	$S_{CO_2}^{600\,°C}$	$Y_{Syngas}^{600\,°C}$
Ru–Pd/CeO_2/IWI	1	0.5	2.7	72.7	82.0	66.7	27.1	6.1	77.0
Pd–CeO_2/IWI/Ru/IWI	1	0.5	4.8	72.9	84.3	67.2	27.7	5.1	80.0
Ru–CeO_2/IWI/Pd/IWI	1	0.5	18.5	71.8	83.2	67.1	27.5	5.4	78.7
Ru–CeO_2/IWI/Pd/IWI	0.5	1	43.2	73.5	83.4	68.2	23.0	8.9	76.0
Ru–CeO_2/IWI/Pd/IWI	0.75	0.75	42.8	71.4	82.9	67.3	25.8	7	77.2
Ru–CeO_2/IWI/Pd/IWI	1.25	0.25	23.0	66.5	67.7	66.0	19.0	14.9	57.7
Ru–CeO_2/IWI/Pd/IWI	1.38	0.12	16.5	55.4	68.9	65.6	21.7	12.7	60.1
Ru–CeO_2/IWI/Pd/IWI	1.44	0.06	17.1	54.0	54.2	66.7	26.0	7.3	50.1

Compared to monometallic catalysts, it should be highlighted that the cooperative effect between Ru and Pd in the bimetallic catalysts is remarkable, with a dramatic increase in both the methane conversion and the syngas yield. At 600 °C, the bimetallic Ru–Pd/CeO_2 catalysts prepared by BM shows CH_4 conversion levels from 79 to 85%, with selectivity towards H_2 of 66–67%, selectivity towards CO of 26–28%, and syngas yield between 71 and 80%, very close to the values corresponding to the thermodynamic equilibrium. In contrast, the bimetallic Ru–Pd/CeO_2 catalysts prepared by the IWI method show methane conversion levels from 54 to 85% with a hydrogen selectivity of 66–68%, CO selectivity of 19–28%, and syngas yield between 50 to 79%. These values obtained over the bimetallic samples are significantly higher than those of the Pd/CeO_2 and Ru/CeO_2 catalysts (Table–6.1) and demonstrate that the synergy between Ru and Pd on CeO_2 yields catalysts with improved activity and

selectivity for the POM with respect to the monometallic counterparts. Fig–6.5 illustrates the influence of the catalyst preparation method (co–IWI or co–BM vs. sequential–IWI or sequential–BM) as well as the effect of the milling conditions (frequency and time) for those catalysts prepared by mechanochemistry.

Fig–6.5a shows the methane conversion at different temperatures (450 to 600 °C) for the bimetallic 0.5Ru–1Pd/CeO_2 catalysts prepared by co–IWI (0.5Ru–1Pd/CeO_2/IWI) and by se–IWI by either impregnating first Pd and then Ru (1Pd–CeO_2/IWI/0.5Ru/IWI), or first Ru and then Pd (0.5Ru–CeO_2/IWI/1Pd/IWI). It is remarkable that the catalyst 0.5Ru–CeO_2/IWI/1Pd/IWI prepared by se–IWI (impregnating first Ru and then Pd) exhibits much higher catalytic activity at 450–500 °C than the catalysts prepared by co–IWI or the catalyst prepared by sequential IWI when Pd is impregnated first on CeO_2. In contrast, at higher reaction temperature (550–600 °C), all catalysts prepared by IWI show a similar activity regardless of the order of metal addition.

In a similar way, the bimetallic 0.5Ru–1Pd/CeO_2 catalyst prepared by sequential BM adding first Ru (0.5Ru–CeO_2/BM/1Pd/BM) indicates a considerable higher catalytic activity at low temperature (Fig–6.5b, 450 °C) than those of the catalyst prepared by co-BM (0.5Ru–1Pd/CeO_2/BM) and two steps adding Pd first (1Pd–CeO_2/BM/0.5Ru/BM), whereas at higher reaction temperature (550–600 °C) similar methane conversion values are recorded, regardless of the order of metal addition. This result suggests that the effect of mechanical forces between the three components of the catalyst (ceria, Ru and Pd) originates a particular catalytic architecture that is extraordinarily active at low temperature. The methane conversion values shown in Figs–6. 5a and 5b confirm that the samples prepared by ball milling always have

higher catalytic activity than the respective counterparts prepared by IWI method, and that these differences are particularly evident at low reaction temperature.

Figs–6. 5c and 5d illustrate the conversion of methane of the 0.5Ru–CeO_2/BM/1Pd/BM catalyst prepared with different milling frequency and different milling time, respectively, to infer on the influence of the ball milling parameters on the catalytic activity (selectivity values and syngas yield are reported in Table–6.2). Both the milling frequency and time have a strong effect on the conversion of methane, especially at a low reaction temperature, which follows the order 30 Hz~ 50 Hz > 15 Hz and 10 min > 5 min~ 20 min. Hence, ideal synthesis conditions for the catalysts produced by BM can be established as 30 Hz and 10 min.

A crucial aspect regarding bimetallic catalysts is the relative amount of the two metals involved. In our case, it should also be considered that the cost of Ru is much higher than that of Pd, which has a direct impact on the final cost of the catalyst. Figs–6. 6a and 6b show the methane conversion and syngas yield, respectively, at 450 and 600 °C for bimetallic xRu–CeO_2/BM/yPd/BM and xRu–CeO_2/IWI/yPd/IWI catalysts containing different amounts of Ru (x = from 0.06 to 1 wt.%) and Pd (y = from 0.5 to 1.44 wt.%), keeping the total metal loading (x + y) at 1.5 wt.%.

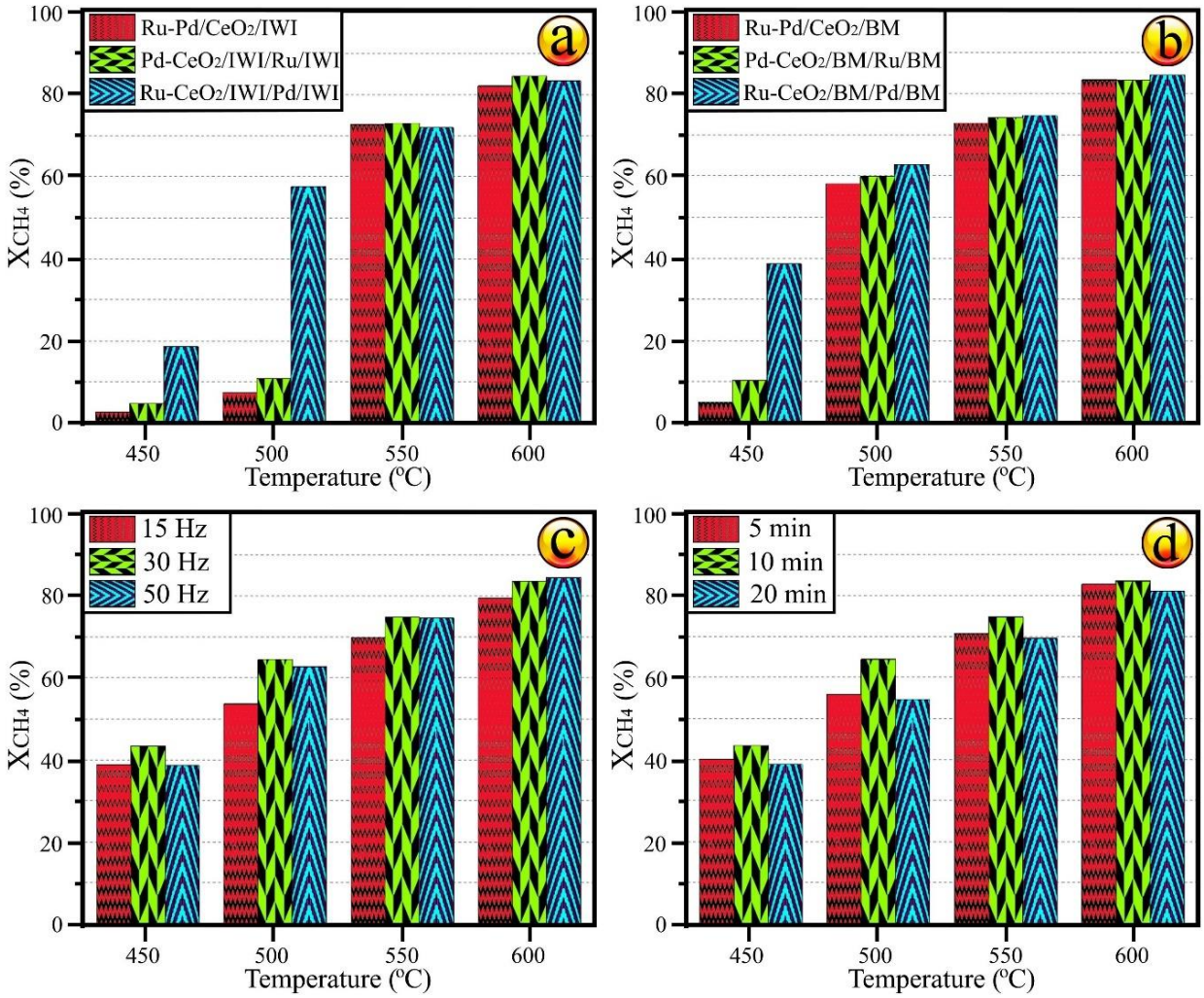

Fig-6. 5: Conversion of methane at 450–600 °C of bimetallic 0.5Ru–1Pd/CeO_2 catalysts prepared by co–IWI and sequential–IWI (a) and co–BM and sequential–BM at 50 Hz for 10 min (b). Conversion of methane at 450–600 °C of 0.5Ru–CeO_2/BM/1Pd/BM catalyst prepared with different milling frequencies (c) and different milling times (d). Reaction conditions: CH_4:air:N_2= 4:11:85, F/W= 60 L h^{-1} g^{-1}, GHSV= 12 × 10^3 h^{-1}.

There is a correlation between catalytic activity and the Ru content in the bimetallic samples produced by IWI method, being the catalysts with a progressive Ru loading more active in the transformation of methane and more selective to syngas. The bimetallic BM samples, in sharp contrast, do not follow this trend and no large differences in methane conversion and syngas selectivity are encountered, being

methane conversion and syngas selectivity values much higher than those recorded on the catalysts prepared by the IWI method with the same composition, particularly at low temperature and low Ru content.

It is important to note that the selectivity to syngas is maintained approximately constant at each temperature for the catalysts prepared by the BM method regardless of the relative metal content, whereas for the catalysts prepared by the IWI method the selectivity to syngas is strongly influenced by the relative amounts of the metals, being large quantities of Ru necessary to attain syngas selectivity values similar to those attained by the samples prepared by mechanochemistry. It should be highlighted that no syngas production was observed for temperatures lower than 550°C for the Ru/CeO_2/BM (Table–6.1). Certainly, the bimetallic Ru–Pd system appears as a particularly appealing metal combination to conduct POM at low temperature, where very reactive and specific active sites are created by ball milling with ceria [204].

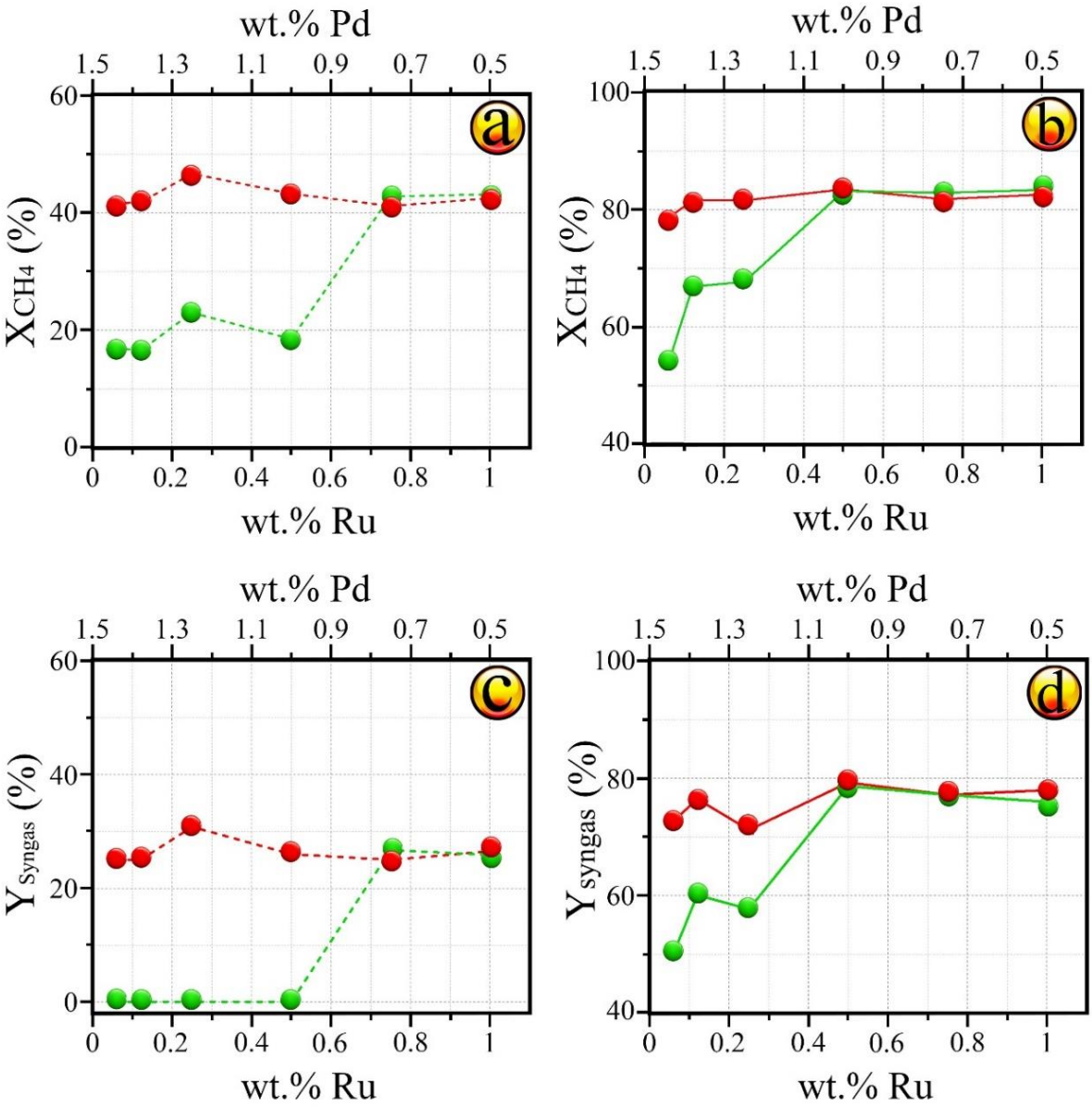

Fig-6. 6: Methane conversion at 450 °C (a) and 600 °C (b) and syngas yield at 450 °C (c) and 600 °C (d) for bimetallic catalysts xRu–yPd/CeO_2 prepared by sequential–BM (red), and sequential–IWI (green) methods. All catalysts contain a total nominal metal loading of 1.5 wt.%. Reaction conditions: GHSV= 12×10^3 h^{-1}, F/W= 60 L h^{-1} g^{-1} and CH_4:air:N_2= 4:11:85 Ball mill conditions: 30 Hz for 10 min.

6.3 Characterization of catalysts after reaction

Fig–6.7 displays the Raman spectra recorded for the monometallic Ru and Pd samples and bimetallic Ru–Pd catalysts prepared by BM and IWI methods after the catalytic test discussed above. In all cases, the position of the F_{2g} band of CeO_2 remained constant and did not shift after the catalytic test with respect to the values recorded before reaction (Fig–6.1), suggesting that there is no incorporation of metals in the ceria structure during the reaction under the conditions tested. As anticipated, the symmetric ν_1 stretching mode of the nitrate anion and the B_{1g} mode of PdO in the monometallic Pd/CeO_2 produced by both IWI and BM methods disappeared after reaction due to decomposition. Additionally, the two characteristic graphite D and G bands at about ~1345 and ~1595 cm^{-1} [187, 188] were observed in the Raman spectra for the catalysts after reaction. Even if their relative contribution in the spectra is certainly weak, it is reasonable to draw the conclusion that carbon deposition is more abundant on the monometallic samples and, in particular, on samples prepared by the IWI method. This constitutes another crucial issue that supports the benefits of using the ball milling for preparing $Ru–Pd/CeO_2$ catalysts.

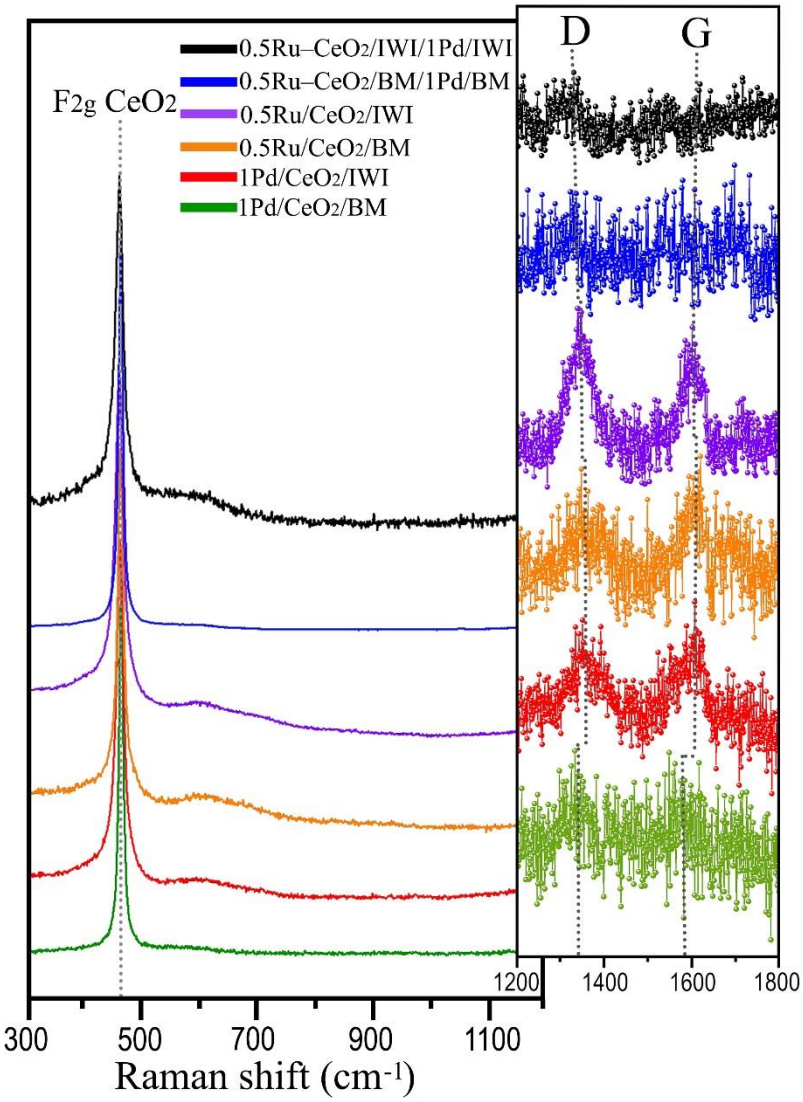

Fig-6. 7: Raman spectra of the monometallic catalysts 1Pd/CeO_2/BM, 1Pd/CeO_2/IWI, 0.5Ru/CeO_2/BM and0.5Ru/CeO_2/IWI, and bimetallic catalysts 0.5Ru–CeO_2/BM/1Pd/BM and 0.5Ru–CeO_2/IWI/1Pd/IWI after reaction at 600 °C. Reaction conditions: CH_4:air:N_2= 4:11:85, F/W= 60 L h^{-1} g^{-1}, GHSV=12 × 10^3 h^{-1}. Ball mill conditions: 30 Hz for 10 min.

Fig–6.8 shows high–resolution transmission electron microscopy (HRTEM) images corresponding to monometallic Pd/CeO_2 and bimetallic Ru–Pd/CeO_2 catalysts prepared by both BM and IWI methods after reaction. A representative image of the monometallic 1Pd/CeO_2 prepared by the BM is shown in Fig–6.8a. The

sample contains Pd nanoparticles that measure about 3–4 nm and are well dispersed over the CeO_2 support (highlighted by circles). The Fourier Transform (FT) analysis of the lattice fringes reveals the presence of spots at 1.94 Å from Pd^0 (200) planes and at 2.04 Å from PdO (101) crystallographic planes. Fig–6.8b shows representative HRTEM images of the monometallic 1Pd/CeO_2/IWI catalyst. Similar to the 1Pd/CeO_2/BM sample, both Pd^0 and PdO nanoparticles are identified, but their size is larger, about 4–7 nm. Additionally, this catalyst shows the occurrence of carbon deposition, which is in accordance to the Raman results. Fig–6.8c corresponds to the bimetallic Ru–CeO_2/BM/Pd/BM catalysts, and for this sample it is difficult to distinguish any Ru, Pd or Ru–Pd particle in the HRTEM analysis, which indicates an excellent dispersion of Ru and Pd on the CeO_2 support. Moreover, the mechanochemical synthesis of the Ru–CeO_2/BM/Pd/BM catalyst creates an amorphous layer on the ceria crystallites, similar to Pd/CeO_2 catalysts prepared by BM and reported in chapter 3 [90], which is kept under reaction. This shell exhibits an average thickness of about 1–2 nm (marked between arrows). Finally, Fig–6.8d corresponds to the bimetallic Ru–CeO_2/IWI/Pd/IWI catalyst, and the HRTEM images for this sample show the presence of PdO and RuO_2 particles after reaction, with a size distribution of about 4–7 nm.

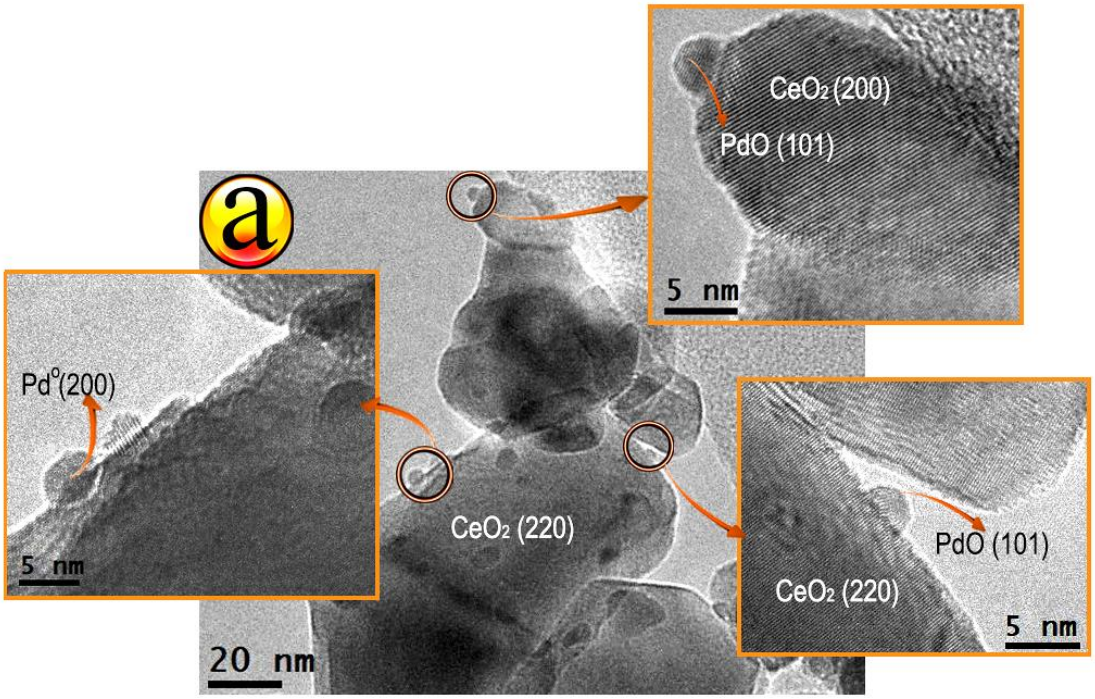
a
CeO2 (200)
PdO (101)
5 nm
Pd°(200)
5 nm
CeO2 (220)
PdO (101)
CeO2 (220)
5 nm
20 nm

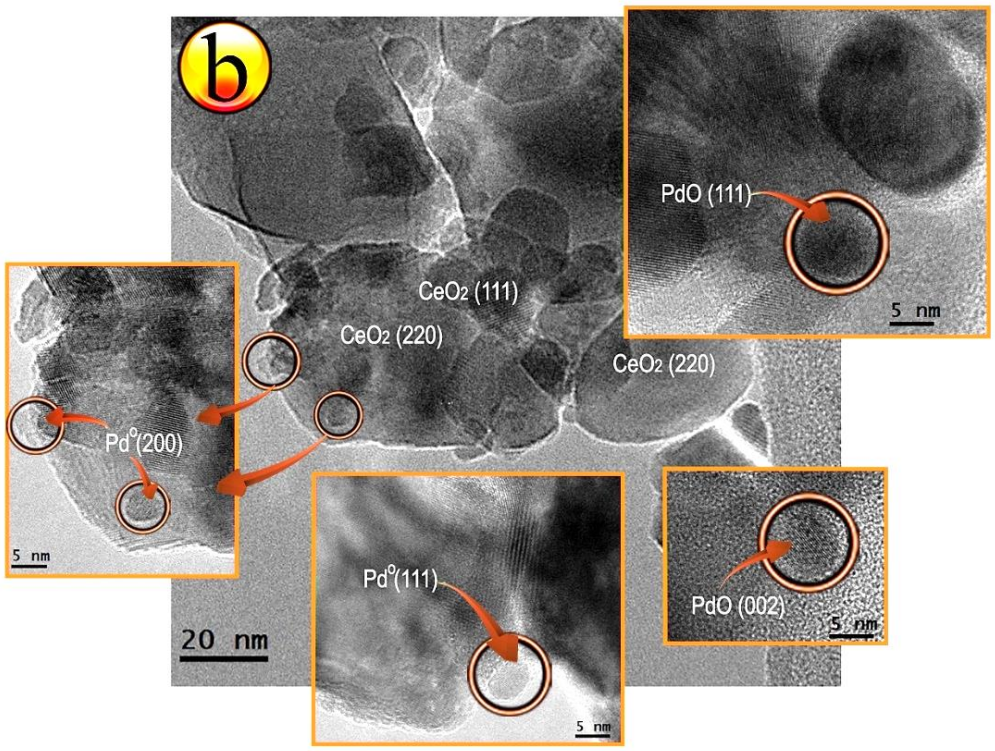
b
PdO (111)
5 nm
CeO2 (111)
CeO2 (220)
CeO2 (220)
Pd°(200)
5 nm
Pd°(111)
5 nm
PdO (002)
5 nm
20 nm

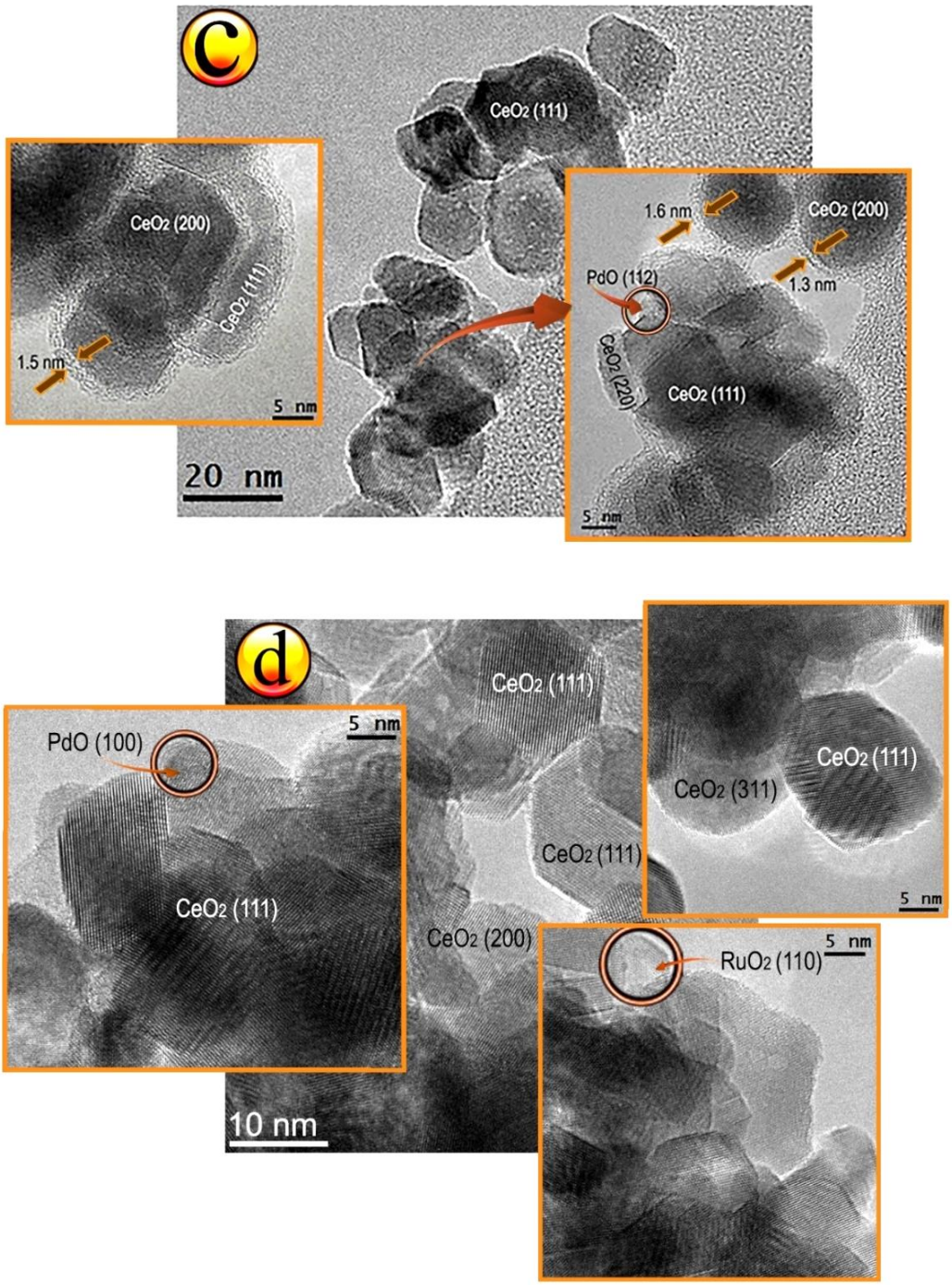

Fig-6. 8: HRTEM images of catalysts 1Pd/CeO_2/BM (a), 1Pd/CeO_2/IWI (b), 0.5Ru–CeO_2/BM/1Pd/BM (c) and 0.5Ru–CeO_2/IWI/1Pd/WI (d) after reaction at 600 °C. Reaction conditions: CH_4:air:N_2= 4:11:85, F/W= 60 L h^{-1} g^{-1}, GHSV=12 × 10^3 h^{-1}. Ball mill conditions: 30 Hz for 10 min.

The presence of reduced metal after reaction suggests that due to the formation of syngas the catalysts are progressively reduced under reaction conditions. Consequently, in order to understand the synergistic effect that Ru–Pd plays, we reduced the sample 0.5Ru–CeO_2/BM/1Pd/BM at 550 °C for 1h before reaction (10% H_2 in Ar, 20 mL min^{-1}). Figs–6. 9a and 9b shows the results of methane conversion and syngas yield at different temperatures, respectively. It obviously demonstrates that the reduction treatment is detrimental to the reaction. It can be claimed that a direct reduction treatment is not advantageous for the synergistic effect between Ru and Pd in the BM samples, whereas the progressive reduction of the sample under reaction yields an optimum Ru–Pd interaction, being this effect particularly important at low reaction temperature.

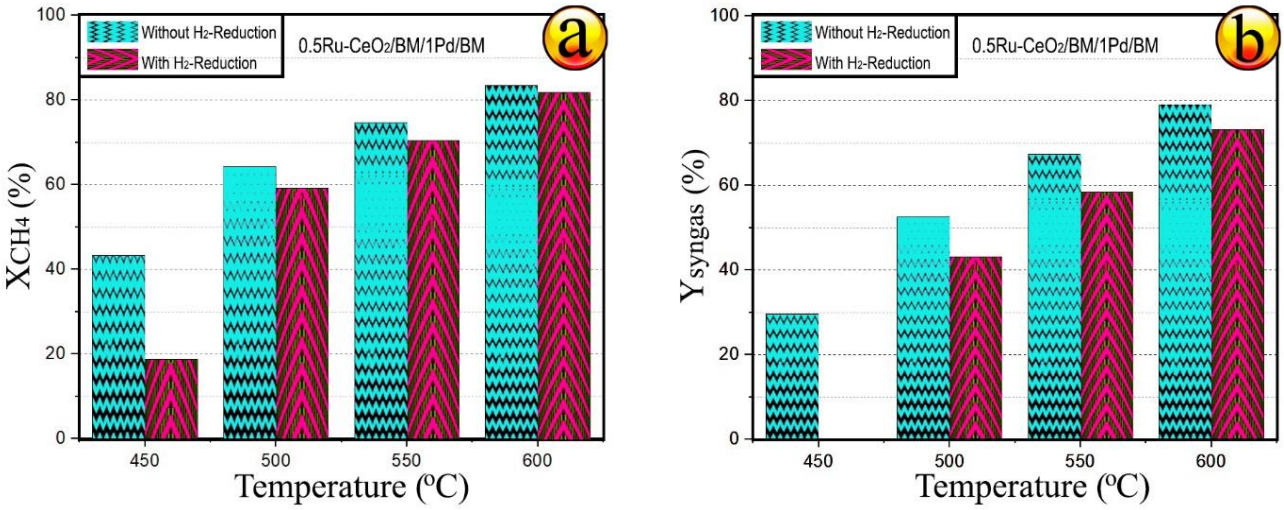

Fig-6. 9: Conversion of methane and yield of syngas on bimetallic catalyst 0.5Ru–CeO_2/BM/1Pd/BM reduced at 550 °C for 1 h. Reaction conditions: CH_4:air:N_2= 4:11:85, F/W= 60 L h^{-1} g^{-1}, GHSV=12 × 103 h^{-1}. Ball mill conditions: 30 Hz for 10 min.

6.4 Stability test

Fig–6.10 shows the stability test which was carried out for more than 100 h at 550 °C on the bimetallic catalysts 0.5Ru–CeO_2/BM/1Pd/BM and 0.5Ru–CeO_2/IWI/1Pd/WI, since these two catalysts exhibited good methane conversion and selectivity to syngas (see Tables–6. 2 and 3). For comparative purposes, the monometallic 0.5Ru/CeO_2/BM and 1Pd/CeO_2/BM samples also were also examined.

Figs–6. 10a and 10b show the methane conversion and syngas yield, respectively. As expected, the initial CH_4 conversion and syngas yield of both Ru–Pd/CeO_2 bimetallic catalysts were remarkably higher than those of the monometallic samples, and the bimetallic catalyst prepared by the BM method performed better than the bimetallic counterpart prepared by the IWI method. Up to the first 50 h on stream, the catalytic performance of both Ru–Pd bimetallic catalysts produced by either BM vs. IWI methods exhibited a steady decrease of the CH_4 conversion rate of ~0.03 % h^{-1}. On the other side, for the monometallic Ru/CeO_2/BM and Pd/CeO_2/BM the deactivation rates of methane conversion were much higher, ~0.24 % h^{-1} and ~0.26 % h^{-1}, respectively.

In the following 50 h on stream, the catalytic performance of the Ru–Pd bimetallic catalyst prepared by BM reached a steady-state in both CH_4 conversion and syngas yield, and the deactivation rate was practically zero (0.01 % h^{-1}). The methane conversion and syngas yield for this bimetallic catalyst stabilized at ~70% and ~60%, respectively. In contrast, the catalytic performance of the Ru–Pd bimetallic catalyst prepared by the IWI method and the Ru and Pd monometallic samples did not stabilize, and deactivation continued progressing, especially for the monometallic 1Pd/CeO_2/BM sample. As a conclusion, the catalysts activity and stability follow the

order: Ru–CeO_2/BM/Pd/BM > Ru–CeO_2/IWI/Pd/IWI > Ru/CeO_2/BM >> Pd/CeO_2/BM. Thus, the bimetallic sample prepared by BM not only exhibited higher methane conversion and syngas production, but also significantly higher stability.

Raman spectra was recorded on the Pd/CeO_2/BM, Ru–CeO_2/BM/Pd/BM and Ru–CeO_2/IWI/Pd/IWI catalysts after the long-term stability test (Fig–6.10c), since the methane dry reforming is part of the POM reaction mechanism and commonly causes carbon deposition on the catalyst. The intensity of the D and G bands of carbon were observed at about ~1410 and ~1650 cm^{-1}, respectively [90, 157], and follows the trend Pd/CeO_2/BM >> Ru–CeO_2/IWI/Pd/IWI > Ru–CeO_2/BM/Pd/BM, which is exactly the opposite trend of stability result. Consequently, it can be concluded that the presence of carbon deposition can explain the catalysts' deactivation during the stability test, and that the almost absence of carbon deposition on the 0.5Ru–CeO_2/BM/1Pd/BM catalyst indicates its suitability to carry out POM under practical conditions.

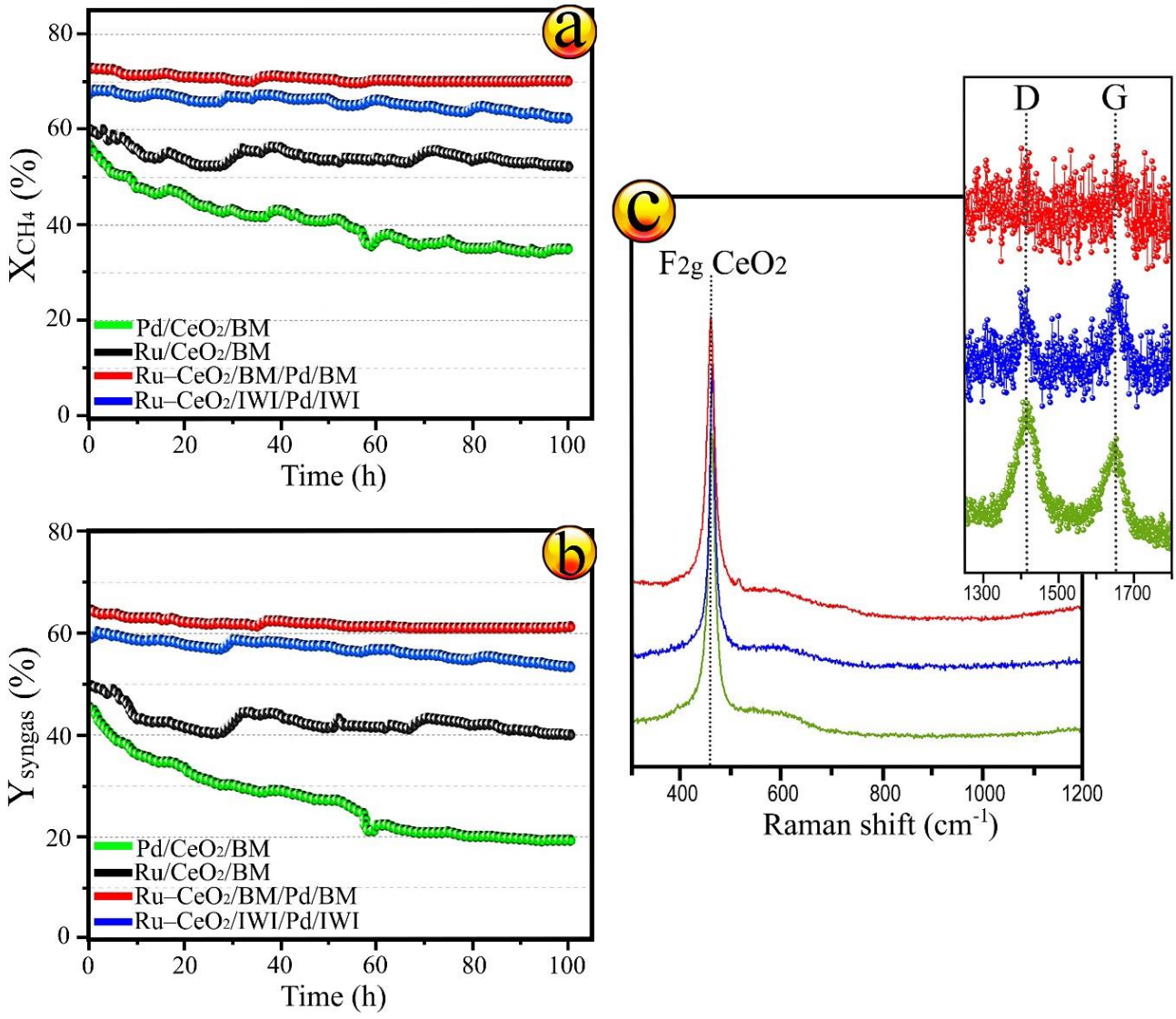

Fig-6. 10: Conversion of methane (a) and yield of syngas (b) in a long–term stability test at 550 °C on monometallic catalysts 1Pd/CeO_2/BM and 0.5Ru/CeO_2/BM, and bimetallic catalysts 0.5Ru–CeO_2/BM/1Pd/BM and 0.5Ru–CeO_2/IWI/1Pd/IWI. Raman spectra recorded on the samples after the long-term stability test (c). Reaction conditions: CH_4:air:N_2= 4:11:85, F/W= 60 L h^{-1} g^{-1}, GHSV=12 × 10^3 h^{-1}. Ball mill conditions: 30 Hz for 10 min.

6.5 Conclusions

In this chapter, monometallic Pd and Ru and bimetallic Pd–Ru catalysts supported on CeO_2 have been prepared by BM and IWI methods, and have been characterized and tested for the POM reaction at atmospheric pressure to produce syngas between 300 and 600 °C. The catalytic results clearly demonstrated that the bimetallic Ru–Pd catalysts showed a greater activity and selectivity in comparison to monometallic Ru or Pd catalysts, and that the CH_4 conversion and syngas yield observed for different catalysts followed the order: Ru–CeO_2/BM/Pd/BM ≥ Ru–CeO_2/IWI/Pd/IWI >> Ru/CeO_2/BM ~ Pd/CeO_2/IWI ≥ Ru/CeO_2/IWI ~ Pd/CeO_2/BM >> CeO_2.

The catalytic results confirm a strong synergy between Ru and Pd on CeO_2 occurring in the bimetallic samples produced by sequential–BM, resulting in much more active sites for POM, particularly at temperatures below 500 °C. In addition, the bimetallic Ru–Pd catalysts prepared by two sequential–BM not only produced syngas at lower temperature, but also revealed excellent stability in long-term experiments during 100 h on stream at 550 °C, with no carbon deposition, outperforming by a large extent those of the bimetallic Ru–Pd catalysts produced by sequential–IWI, and the monometallic Ru/CeO_2 and Pd/CeO_2 catalysts. Moreover, by studying the effect of Ru and Pd loadings in the bimetallic Ru–CeO_2/BM-IWI/Pd/BM-IWI catalysts prepared by sequential–IWI and sequential–BM, it has been confirmed that while the methane conversion increased gradually with the Ru content for the Ru–CeO_2/IWI/Pd/IWI catalysts, it was maintained approximately constant for the Ru–CeO_2/BM/Pd/BM samples. The best catalytic performance with maximum methane conversion and syngas yield values was achieved with catalysts containing 0.25 wt.% Ru and 1.25 wt.% Pd (0.25Ru–CeO_2/BM/1.25Pd/BM). Based

on these results, highly active catalysts for POM can be designed and prepared by ball milling, a simple and scalable method, by using small amounts of Pd and Ru.

6.6 References

1. Dedov, A., et al., High-selectivity partial oxidation of methane into synthesis gas: the role of the red-ox transformations of rare earth—alkali earth cobaltate-based catalyst components. Fuel Processing Technology, 2016. **148**: p. 128-137.
2. Freni, S., G. Calogero, and S. Cavallaro, Hydrogen production from methane through catalytic partial oxidation reactions. Journal of Power Sources, 2000. **87**(1-2): p. 28-38.
3. Fakeeha, A.H., A.S. Al-Fatesh, and A.E. Abasaeed, Modification of alumina support with TiO_2-P_{25} in CO2 reforming of CH_4. Journal of Industrial and Engineering Chemistry, 2012. **18**(1): p. 212-217.
4. Moral, A., et al., Partial oxidation of methane to syngas using Co/Mg and Co/Mg-Al oxide supported catalysts. Catalysis Today, 2019. **333**: p. 259-267.
5. Makarshin, L., et al., Catalytic partial oxidation of methane in microchannel reactors with co-current and countercurrent reagent flows: An experimental comparison. Chemical engineering journal, 2011. **178**: p. 276-281.
6. Xie, J., et al., Autothermal reforming and partial oxidation of n-hexadecane via Pt/Ni bimetallic catalysts on ceria-based supports. International Journal of Hydrogen Energy, 2015. **40**(27): p. 8510-8521.
7. Khajenoori, M., M. Rezaei, and B. Nematollahi, Preparation of noble metal nanocatalysts and their applications in catalytic partial oxidation of methane. Journal of Industrial and Engineering Chemistry, 2013. **19**(3): p. 981-986.
8. Maniecki, T.P., et al., Effect of the chemical composition of (MgO) x (Al_2O_3) y support on the catalytic performance of Ni and Ni–Au catalysts for the partial oxidation of methane. Chemical Engineering Journal, 2009. **154**(1-3): p. 142-148.

9. Navarro, R.M., M. Pena, and J. Fierro, Hydrogen production reactions from carbon feedstocks: fossil fuels and biomass. Chemical reviews, 2007. **107**(10): p. 3952-3991.
10. Kriz, D.A., et al., Partial Oxidation of Methane to Synthesis Gas Using Supported Ga-Containing Bimetallic Catalysts and a Ti-Promoter. ChemCatChem, 2018. **10**(19): p. 4300-4308.
11. Requies, J., et al., Nickel/alumina catalysts modified by basic oxides for the production of synthesis gas by methane partial oxidation. Catalysis today, 2006. **116**(3): p. 304-312.
12. Cifuentes, B., et al., Monoliths washcoated with AuCu catalysts for CO removal in an ethanol fuel processor: Effect of CeO_2–SiO_2 dual support on the catalytic performance and reactor cost. International Journal of Hydrogen Energy, 2021. **46**(2): p. 2166-2181.
13. Ashcroft, A., et al., Selective oxidation of methane to synthesis gas using transition metal catalysts. Nature, 1990. **344**(6264): p. 319-321.
14. Tsang, S., J. Claridge, and M. Green, Recent advances in the conversion of methane to synthesis gas. Catalysis today, 1995. **23**(1): p. 3-15.
15. Hickman, D., E. Haupfear, and L. Schmidt, Synthesis gas formation by direct oxidation of methane over Rh monoliths. Catalysis letters, 1993. **17**(3): p. 223-237.
16. Hickman, D. and L. Schmidt, Production of syngas by direct catalytic oxidation of methane. science, 1993. **259**(5093): p. 343-346.
17. Hickman, D. and L.D. Schmidt, Steps in CH4 oxidation on Pt and Rh surfaces: High-temperature reactor simulations. AIChE Journal, 1993. **39**(7): p. 1164-1177.

18. Poirier, M.G., J. Trudel, and D. Guay, Partial oxidation of methane over ruthenium catalysts. Catalysis letters, 1993. **21**(1): p. 99-111.
19. Horn, R., et al., Methane catalytic partial oxidation on autothermal Rh and Pt foam catalysts: Oxidation and reforming zones, transport effects, and approach to thermodynamic equilibrium. Journal of Catalysis, 2007. **249**(2): p. 380-393.
20. Yamagishi, T., et al., Catalytic performance and characterization of $RhVO_4/SiO_2$ for hydroformylation and CO hydrogenation. Journal of Molecular Catalysis A: Chemical, 2006. **244**(1-2): p. 201-212.
21. Tomishige, K., M. Asadullah, and K. Kunimori, Syngas production by biomass gasification using $Rh/CeO_2/SiO_2$ catalysts and fluidized bed reactor. Catalysis Today, 2004. **89**(4): p. 389-403.
22. Torniainen, P., X. Chu, and L. Schmidt, Comparison of monolith-supported metals for the direct oxidation of methane to syngas. Journal of Catalysis, 1994. **146**(1): p. 1-10.
23. Chen, W., et al., Titanium-promoted Rh-Mn-Li/SiO2 for C2-oxygenates synthesis from syngas: effect of low titanium loading. Journal of Natural Gas Chemistry, 2005. **14**(4): p. 199-206.
24. Choudhary, V.R., K.C. Mondal, and S.A. Mulla, Simultaneous conversion of methane and methanol into gasoline over bifunctional Ga-, Zn-, In-, and/or Mo-modified ZSM-5 zeolites. Angewandte Chemie, 2005. **117**(28): p. 4455-4459.
25. Kaila, R.K., et al., Zirconia-supported bimetallic RhPt catalysts: Characterization and testing in autothermal reforming of simulated gasoline. Applied Catalysis B: Environmental, 2008. **84**(1-2): p. 223-232.

26. Nikolla, E., J. Schwank, and S. Linic, Promotion of the long-term stability of reforming Ni catalysts by surface alloying. Journal of catalysis, 2007. **250**(1): p. 85-93.
27. Zhang, J., H. Wang, and A.K. Dalai, Development of stable bimetallic catalysts for carbon dioxide reforming of methane. Journal of Catalysis, 2007. **249**(2): p. 300-310.
28. Luo, Z., et al., TiO_2 Supported gold–palladium catalyst for effective syngas production from methane partial oxidation. Applied Catalysis A: General, 2018. **554**: p. 54-63.
29. Ramírez-López, R., I. Elizalde-Martinez, and L. Balderas-Tapia, Complete catalytic oxidation of methane over $Pd/CeO_2–Al_2O_3$: The influence of different ceria loading. Catalysis Today, 2010. **150**(3-4): p. 358-362.
30. Wang, Y. and J. Zhang, Hydrogen production on $Ni–Pd–Ce/\gamma\text{-}Al_2O_3$ catalyst by partial oxidation and steam reforming of hydrocarbons for potential application in fuel cells. Fuel, 2005. **84**(14-15): p. 1926-1932.
31. Mustu, H., et al., Effect of synthesis route of mesoporous zirconia based Ni catalysts on coke minimization in conversion of biogas to synthesis gas. international journal of hydrogen energy, 2015. **40**(8): p. 3217-3228.
32. da Silva, A.M., et al., Study of the performance of $Rh/La_2O_3–SiO2$ and Rh/CeO_2 catalysts for SR of ethanol in a conventional fixed-bed reactor and a membrane reactor. international journal of hydrogen energy, 2015. **40**(11): p. 4154-4166.
33. Wang, Z., et al., Self-sustained electrochemical promotion catalysts for partial oxidation reforming of heavy hydrocarbons. international journal of hydrogen energy, 2012. **37**(23): p. 17928-17935.

34. Xu, X., P. Li, and Y. Shen, Small-scale reforming of diesel and jet fuels to make hydrogen and syngas for fuel cells: A review. Applied energy, 2013. **108**: p. 202-217.
35. Fazlikeshteli, S., X. Vendrell, and J. Llorca, Low-Temperature Methane Partial Oxidation over Pd Supported on CeO_2: Effect of the Preparation Method and Precursors. Reactions, 2021. **2**(1): p. 30-42.
36. Danielis, M. and S. Colussi, de leitenburg, C.; Soler, L.; Llorca, J.; Trovarelli, A. Outstanding Methane Oxidation Performance of Pd-Embedded Ceria Catalysts Prepared by a One-step Dry Ball-Milling Method. Angew. Chem, 2018. **130**: p. 10369-10373.
37. Fazlikeshteli, S., X. Vendrell, and J. Llorca, Low-temperature partial oxidation of methane over Pd–Ni bimetallic catalysts supported on CeO_2. International Journal of Hydrogen Energy, 2022.
38. Engineering, D.o.C.a.B. Bioanalytical Microfluidics Program. 2019; Available from: http://cbe.colostate.edu/.
39. Wu, Z., et al., Probing defect sites on CeO_2 nanocrystals with well-defined surface planes by Raman spectroscopy and O_2 adsorption. Langmuir, 2010. **26**(21): p. 16595-16606.
40. Weber, W., K. Hass, and J. McBride, Raman study of CeO_2: Second-order scattering, lattice dynamics, and particle-size effects. Physical Review B, 1993. **48**(1): p. 178.
41. Ma, J., et al., The relationship between the chemical state of Pd species and the catalytic activity for methane combustion on Pd/CeO_2. Catalysis Science & Technology, 2018. **8**(10): p. 2567-2577.

42. Lucentini, I., et al., Ammonia decomposition over 3D-printed CeO_2 structures loaded with Ni. Applied Catalysis A: General, 2020. **591**: p. 117382.
43. Lucentini, I., et al., Catalytic ammonia decomposition over Ni-Ru supported on CeO_2 for hydrogen production: Effect of metal loading and kinetic analysis. Applied Catalysis B: Environmental, 2021. **286**: p. 119896.
44. Luo, M.-F., et al., Characterization study of CeO_2 supported Pd catalyst for low-temperature carbon monoxide oxidation. Catalysis letters, 1998. **50**(3): p. 205-209.
45. Xingyi, W., K. Qian, and L. Dao, Catalytic combustion of chlorobenzene over MnOx–CeO_2 mixed oxide catalysts. Applied Catalysis B: Environmental, 2009. **86**(3-4): p. 166-175.
46. Zhang, J., et al., Performance of bimetallic PdRu catalysts supported on gamma alumina for 2-ethylanthraquinone hydrogenation. RSC advances, 2017. **7**(11): p. 6447-6456.
47. Zhu, H., et al., Pd/CeO2–TiO2 catalyst for CO oxidation at low temperature: a TPR study with H2 and CO as reducing agents. Journal of Catalysis, 2004. **225**(2): p. 267-277.
48. Pérez-Bustos, H.F., et al., Synthesis and characterization of bimetallic catalysts Pd-Ru and Pt-Ru supported on γ-alumina and zeolite FAU for the catalytic transformation of HMF. Fuel, 2019. **239**: p. 191-201.
49. Pang, J., et al., Mesoporous Cu_2O–CeO_2 composite nanospheres with enhanced catalytic activity for 4-nitrophenol reduction. Applied Surface Science, 2018. **439**: p. 420-429.

50. Ho, P., et al., One-step electrodeposition of Pd–CeO_2 on high pore density foams for environmental catalytic processes. Catalysis Science & Technology, 2018. **8**(18): p. 4678-4689.
51. Danielis, M., et al., Methane oxidation activity and nanoscale characterization of Pd/CeO_2 catalysts prepared by dry milling Pd acetate and ceria. Applied Catalysis B: Environmental, 2022. **282**: p. 119567.
52. Enger, B.C., R. Lødeng, and A. Holmen, A review of catalytic partial oxidation of methane to synthesis gas with emphasis on reaction mechanisms over transition metal catalysts. Applied Catalysis A: General, 2008. **346**(1-2): p. 1-27.
53. York, A.P., T. Xiao, and M.L. Green, Brief overview of the partial oxidation of methane to synthesis gas. Topics in Catalysis, 2003. **22**(3-4): p. 345-358.
54. Hannemann, S., et al., Combination of flame synthesis and high-throughput experimentation: The preparation of alumina-supported noble metal particles and their application in the partial oxidation of methane. Applied Catalysis A: General, 2007. **316**(2): p. 226-239.
55. Han, Z., et al., Propane dehydrogenation over Pt–Cu bimetallic catalysts: the nature of coke deposition and the role of copper. Nanoscale, 2014. **6**(17): p. 10000-10008.
56. Chen, Y. and J. Chen, Selective hydrogenation of acetylene on SiO_2 supported Ni-In bimetallic catalysts: Promotional effect of In. Applied Surface Science, 2016. **387**: p. 16-27.

7. Conclusions

- A series of CeO_2-supported monometallic (Pd, Ni and Ru) and bimetallic (Pd–Ni, Ru–Ni and Pd–Ru) catalysts have been prepared by mechanochemistry (BM) and incipient wetness impregnation (IWI), characterized, and tested in the partial oxidation of methane (POM) to obtain syngas.
- The preparation method (BM vs. IWI), the order of incorporation of the metals (one or two steps), and the experimental conditions (frequency and time) for the samples prepared by BM play an important role on the catalytic performance.
- The CeO_2 support and the monometallic Ni/CeO_2 catalysts in the absence of noble metals are totally inactive for the POM process under the reaction conditions tested. On the other hand, the monometallic Pd/CeO_2 catalyst prepared by BM shows the best catalytic performance among the monometallic catalysts.
- The bimetallic Pd–Ni, Ru–Ni, and Pd–Ru catalysts exhibited a dramatic increase in both the methane conversion and the syngas yield compared to monometallic Pd, Ru, and Ni samples under the same operation conditions, pointing out to a beneficial effect of the synergy between the two metals.
- The bimetallic catalysts prepared by BM produce syngas at a lower temperature and are much more stable than those prepared by the conventional IWI method.
- The higher stability of bimetallic samples prepared by BM is related to its ability to suppress the deposition of carbon during the POM process.
- The selectivity to syngas is maintained approximately constant for the bimetallic catalysts prepared by the BM method regardless of the relative metal content (same total metal loading), whereas for the catalysts prepared by IWI the

selectivity to syngas is strongly influenced by the relative amounts of the metals, being large quantities of Ru or Pd necessary to attain syngas selectivity values similar to those attained by the samples prepared by mechanochemistry.

- Raman spectra reveal that defect-induced vibrational modes are nearly absent in almost all samples, which means that the incorporation of metals does not result in the formation of lattice defects in the ceria structure, such as oxygen vacancies.
- Temperature–programmed reduction (H_2–TPR) demonstrates that the reduction of CeO_2 in the bimetallic catalysts is shifted to lower temperatures with respect to the monometallic counterparts, which means the simultaneous presence of metals exerts a positive influence on the CeO_2 reduction.
- In contrast with conventional catalysts, high-resolution transmission electron microscopy (HRTEM) shows poorly-defined nanometric and subnanometric structures on the ceria crystallites in the catalysts prepared by mechanochemistry.
- As a general rule, X–ray photoelectron spectroscopy (XPS) shows higher M/Ce surface atomic ratios in the samples prepared by BM with respect to the catalyst prepared by IWI; therefore, it is concluded that metal species strongly interacting with ceria are easily accommodated on the surface of the catalysts prepared by mechanochemical methods.
- The characterization of post-reacted samples demonstrates that the high dispersion of the metals is maintained during the catalytic reaction.
- Overall, these results encourage the use of mechanochemistry as a simple, scalable, fast, cost-effective, and environmentally friendly methodology to prepare a new generation of active catalysts for the POM process to obtain syngas.